DEUTSCHE GEODÄTISCHE KOMMISSION

bei der Bayerischen Akademie der Wissenschaften

Reihe B | Angewandte Geodäsie | Heft Nr. 317

Andreas Hense, Jürgen Sündermann, Hermann Drewes,
Maik Thomas, Xueen Chen, Robert Dill, Malte Müller, Florian Seitz,
Jochen Stuck, Claudia Walter, Timo Winkelnkemper

Physically consistent system model for the study of the Earth's rotation, surface deformation and gravity field parameters

– Scientific results of the DFG project –

München 2009

Verlag der Bayerischen Akademie der Wissenschaften
in Kommission beim Verlag C. H. Beck

ISSN 0065-5317 ISBN 978-3-7696-8596-1

DEUTSCHE GEODÄTISCHE KOMMISSION

bei der Bayerischen Akademie der Wissenschaften

Reihe B | Angewandte Geodäsie | Heft Nr. 317

Andreas Hense, Jürgen Sündermann, Hermann Drewes,
Maik Thomas, Xueen Chen, Robert Dill, Malte Müller, Florian Seitz,
Jochen Stuck, Claudia Walter, Timo Winkelnkemper

Physically consistent system model for the study of the Earth's rotation, surface deformation and gravity field parameters

– Scientific results of the DFG project –

München 2009

Verlag der Bayerischen Akademie der Wissenschaften
in Kommission beim Verlag C. H. Beck

ISSN 0065-5317 | ISBN 978-3-7696-8596-1

Deutsche Geodätische Kommission

Adresse des Herausgebers /
Address of the publisher

Alfons-Goppel-Straße 11 ● D – 80 539 München
Telefon +49 – 89 – 23 031 1113 ● Telefax +49 – 89 – 23 031 - 1283/ - 1100
e-mail hornik@dgfi.badw.de ● http://www.dgk.badw.de

Adresse der Autoren /
Address of the authors

Prof. Dr. rer. nat. Andreas Hense,
Dr.rer.nat. Jochen Stuck,
Dr.rer.nat. Timo Winkelnkemper
Meteorologisches Institut
Universität Bonn
Auf dem Hügel 20
D - 53121 Bonn
Tel. +49 - (0)228 - 735184,
Fax: +49 - (0)228 - 735188,
E-Mail ahense@uni-bonn.de

Prof. Dr. rer. nat. Jürgen Sündermann,
Dr.rer.nat. Xueen Chen, Dr.rer.nat. Malte Müller
Institut für Meereskunde
Universität Hamburg
Bundesstr. 53
D - 20146 Hamburg
Tel. +49 - (0)40 - 42838 2606/5095, Fax: +49 - (0)40 - 42838 7488, E-Mail juergen.suendermann@zmaw.de, malte.mueller@zmaw.de

Hon.-Prof. Dr.-Ing. Hermann Drewes
Deutsches Geodätisches Forschungsinstitut
Alfons-Goppel-Str. 11
D - 80539 München
Tel. +49 - (0)89 - 23031 1106,
Fax +49 - (0)89 - 23031 1240,
E-Mail drewes@dgfi.badw.de

Prof. Dr. rer. nat. Maik Thomas, Dr.rer.nat. Robert Dill
Deutsches GeoForschungsZentrum GFZ
Telegraphenberg A17 20.32
D - 14473 Potsdam
Tel. +49 - (0)331 - 288 1147,
Fax +49 - (0)331 - 288 1163,
E-Mail mthomas@gfz-potsdam.de,
dill@gfz-potsdam.de

Prof. Dr.-Ing. Florian Seitz
Earth Oriented Space Science and Technology
Technische Universität München
Arcisstr. 21
D - 80333 München
Tel. +49 - (0)89 - 289 23184,
Fax +49 - (0)89 - 289 23178,
E-Mail seitz@bv.tu-muenchen.de

Dr.-Ing. Claudia Walter
Institut für Planetare Geodäsie
Technische Universität Dresden
Helmholtzstr. 10
D - 01069 Dresden

Diese Publikation ist als pdf-Dokument im Internet veröffentlicht unter der Adresse /
This volume is published as pdf-document in the internet under the address
http://dgk.badw.de/index.php?id=10

ISSN 0065-5317 ISBN 978-3-7696-8596-1

Contents

1. Introduction 5

1.1 The projects 5

1.2 Historical overview and motivations 5

2. Models of subsystems 7

2.1 Atmosphere models ECHAM 8

2.1.1 ECHAM5 8

2.1.2 Stand-alone atmosphere 20th century simulation 8

2.1.3 Results 9

2.2 Ocean model OMCT 12

2.3 Hydrological Discharge Model HDM 12

2.3.1 Continental hydrology modelling 12

2.3.1.1 SLS model component 13

2.3.1.2 HDM model component 13

2.3.1.3 Atmospheric forcing data 14

2.3.2 Results 14

2.3.2.1 Implementation of a 3-D relief model 14

2.3.2.2 Calculation of gravity field coefficients 15

2.3.2.3 Test simulations and validation of continental discharge with ECHAM4 and NCEP 15

2.3.2.4 Verification of simulated continental runoff (control runs) 15

2.3.2.5 Interface adaptation and verification of mass conservation at the boundaries in the coupled model system 17

2.3.2.6 Validation and analysis of continental water mass transports of ECOCTH 17

2.3.2.7 Statistical analysis and validation of simulated gravity field variations 17

2.3.2.8 Global water balance 19

2.3.3 Summary 21

3. Models of the coupled system 21

3.1 Coupled atmosphere-hydrosphere model ECOCTH 21

3.1.1 Model description 21

3.1.2 Validation 22

3.1.2.1 The lunisolar ocean tides 22

3.1.2.2 Global ocean circulation 22

3.1.2.3 Tropical variability and global warming 23

3.1.3 Results 23
3.1.3.1 Inter-annual variations and secular trends in length of day 23

3.2 Dynamic model of Earth rotation, gravity and surface deformation DyMEG 25
3.2.1 Numerical solution of the Liouville differential equation 26
3.2.2 Inverse model for surface deformations of the solid Earth due to mass loads 30

4. Results for Earth rotation, surface deformation and gravity 32
4.1 Validation of DyMEG with NCEP and ECCO 32
4.2 Results of DyMEG with ECOCTH forcing 36

5. Scientific highlights 40
5.1 Tidal mixing 40
5.1.1 Tidal mixing in OMCT2 41
5.1.2 Effect of tidal mixing on ocean water mass properties 42

5.2 Secular and decadal variations 43
5.2.1 Coupled simulation of Earth Rotation Parameters 43
5.2.2 Axial AAM long-term trends in 21st century scenario runs 43

5.3 Forcing mechanisms of the Chandler oscillation 45
5.3.1 Atmospheric and hydrospheric excitation of the Chandler oscillation 46
5.3.2 Noise as excitation mechanism of the Chandler oscillation 47

6. Conclusions and outlook 49

7. References 50

1. Introduction

1.1. The projects

This report is the final report of a series of projects which studied the Earth's rotational parameters angular momentum, tensor of inertia as well as related variables of the Earth's gravitational field. A system view has been taken by trying to incorporate the contributions from the various subsystems of the Earth system in a physically consistent way. This introduction will highlight the project history and performance since 1996 and the state of the art in 2000. Table 1.1.1 gives an overview of the sequence of DFG funded projects and the major time steps which ultimately led to this final report.

Table 1.1.1: Overview of projects and principal investigators since 1996

Time	Astronomy	Oceanography	Geodesy	Meteorology	Hydrology	Project-ID
Pre-1995	Brosche (Bonn)	Sündermann (Hamburg)	Campbell/ Schuh (Bonn)			BR675/4 SU69/12
10/1996 … 09/1999	Brosche (Bonn)	Sündermann (Hamburg)	Schuh (DGFI, München)	Hense (Bonn)		BR675/8
06/2000 … 12/2003		Sündermann (Hamburg)	Drewes (DGFI, München)	Hense (Bonn)		HE1916/4 DR143/10
06/2004 … 06/2008		Sündermann (Hamburg)	Drewes (DGFI, München)	Hense (Bonn)	Thomas (Dresden)	HE1916/9 DR143/12 SU69/26 TH864/3

1.2 Historical overview and motivations

Before 1996 already a well established and fruitful cooperation on variations of the Earth's rotation parameters (ERP) existed between P. Brosche (Astronomy, University Bonn), J. Sündermann (Oceanography, University Hamburg) and J. Campbell together with H. Schuh (Geodesy, University Bonn) dating back to 1972. This has been documented in several publications (BROSCHE and SÜNDERMANN, 1978, 1982, 1990).

Additionally a joint seminar on "Earth rotation" was held at the University Bonn by Brosche, Campbell and Hense. Together this led to the idea of a joint proposal studying the components of the ERP (angular momentum, torques and tensor of inertia) from observations and simulations as well as their separate contributions from atmosphere and oceans.

The starting points more than twelve years ago were such that at those times

- No general circulation ocean model (OGCM) which includes tidal motions was available;
- Atmospheric contributions to the ERP had been only estimated from reanalysis data or weather forecasts but not from free runs of atmospheric general circulation models (AGCM) forced by observed sea surface temperatures longer than approximately 10-15 years.

Therefore the aims of this first project had been

- The inclusion of oceanic tides based on full ephemerides data into an oceanic GCM.
- The inclusion of quasi-realistic atmospheric forcing fields (state-of-the-art mid 1990s) for the OGCM from an almost 50 year long simulation of the ECHAM3-T21 model forced by observed global sea surface temperatures SST and sea ice cover SIC.
- The calculation of the budget components of angular momentum of the modelled joint atmosphere-ocean dynamics including a separation of into forced (or predictable by SST/SIC) and free (chaotic or unpredictable) contributions by using the results of ensemble simulations of the ECHAM3-T21 model.

The project was backed up by a parallel one headed by H. Schuh (DGFI München) studying the effects of mass variations on the Earth surface and their contributions to the ERP by supplying them with quasi-realistic (state-of-the-art mid 1990'ies) water fluxes and surface pressure from the ECHAM3-T21 model.

Based on the assumption that the major torque transferring angular momentum between atmosphere and ocean is the frictional torque which depends almost solely on the atmospheric state, it was decided to diagnose the atmospheric forcing field of the ocean from a stand alone atmospheric simulation of the ECHAM3-T21 model forced with observed SST and SIC fields and feed them into a stand alone ocean simulation. This neglects e.g. changes of the atmospheric state due to SST simulated from the stand alone ocean model being different from the observed ones. The setup of the modelling approach is sketched in Fig. 1.2.1.

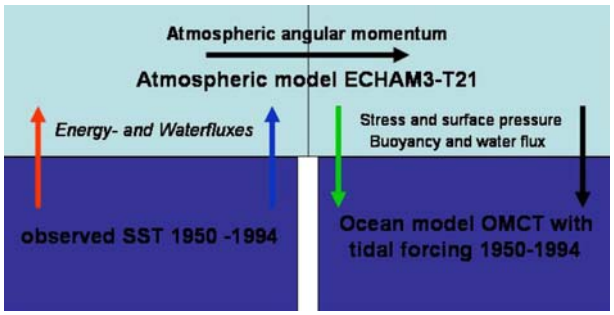

Fig. 1.2.1: Symbolic layout of the modelling approach during the first project phase

The major results from that early project which ended in autumn 1999 showed that the combination of a well developed OGCM with tides included (OMCT) and forced by energy-, mass-, stress-fluxes and surface pressure from a separate AGCM simulation forced by observed SST and SIC fields leads to realistic energy and angular momentum budgets although significant biases could be identified. The most prominent one was a reduction of the annual cycle amplitude of the axial component of the atmospheric angular momentum by 50%.

This proof-of-concept of using an atmospheric and oceanic model without an explicit and interactive coupling for simulating the angular momentum and its budget of the joint system gave rise for a second project proposal which was finally funded in 2000. Due to his retirement P. Brosche did not participate anymore. Instead H. Drewes from DGFI München moved in providing the expertise for modelling the ERP of the solid Earth from the given atmospheric and oceanic torques using the dynamic model of the nonlinear Liouville equation DyMEG.

The major aims of this second project have been:

- A system study of the influence of atmospheric and oceanic torques on the polar motion specifically the test of the hypothesis that the "Chandler-Wobble" is not excited by periodic components of the driving torques but "simply" by stochastic variations in the respective frequency band.
- An assimilation study of the dynamic Earth rotation model by using torques derived from atmospheric re-analysis data and oceanic reconstructions of the respective angular momentum components and their budgets by simulations forced with atmospheric energy-, mass-and stress fluxes derived from reanalysis data.
- A climate study using free simulations of ECHAM4-T42 atmospheric GCM forced with SST/SIC fields for the period 1904-1994 (later continued until 2000) studying long period ("inter-decadal") changes of polar motion and length-of-day.

The project was funded from 2000 onward until 2003. The results showed that

- Indeed the Chandler wobble is excited by temporally stochastic but spatially coherent modes ("Himalaya-mode") (SEITZ et al., 2004);
- Decadal scale variations in axial relative angular momentum variations do exist in the ECHAM4-T42 simulations, which are obviously forced by SST;
- The dynamic Earth rotation model showed that the length-of-day variations on time scales from a few days to several years could be almost completely explained by atmospheric angular momentum (SEITZ, 2002);
- The use of ECHAM4-T42 model data led to a significant improvement of the annual cycle amplitude of the axial component of the atmospheric angular momentum compared to the ECHAM3-T21 (STUCK and HENSE, 2002).

Fig. 1.2.2 shows the symbolic layout of the modelling strategy during the second project.

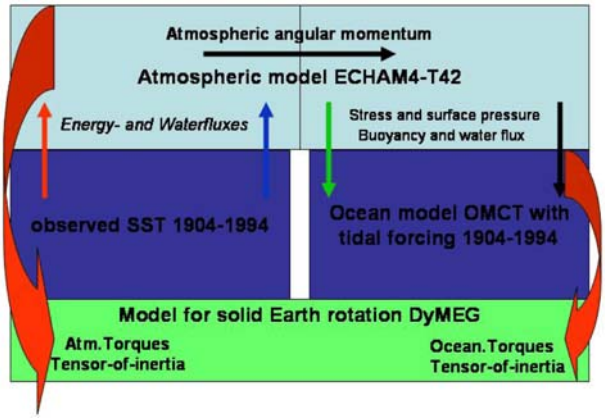

Fig. 1.2.2: Symbolic layout of the modelling approach during the second project phase.

Parallel to our project two initiatives for coordinated programs on specific questions of Earth rotation parameters and earth mass field and its variations have been prepared (and partially launched). The topics of these programs are complementary to our projects and concentrate mainly on the data and their interpretation by appropriate models of the newly available satellite missions CHAMP and GRACE. However, also in these new programs a fully coupled atmosphere-ocean model is not part of the research. Such a model would exchange the energy-, mass- and stress-fluxes interactively between the atmospheric, oceanic and any other necessary sub-model. As a necessary sub-model the land surface hydrology was identified, which allows to calculate the sub-terrain water levels which induce variations of the tensor-of-inertia. Even the global climate models used in the IPCC assessment reports (No.3 in 2001 and No. 4 in 2007) are only coupled in their energy and water cycles but not in their angular momentum cycles. Lastly, it had become clear that the Earth rotational components determined by astrometric-geodetic methods are the only measurable globally integrated variables of the Earth's

systems. This is in contrast e.g. to the globally mean surface temperature which has to be aggregated from individual point-wise measurements using specific model assumptions. Therefore one has to admit that the ERP have the potential for monitoring specific changes of the Earth system related to global climate change. However, as the measured ERP are variables of the solid Earth, the conclusions from the monitored ERP signal with respect to the atmosphere or the ocean require a modelling approach to disintegrate the measured signal. Therefore a prerequisite question for quantifying the monitoring potential are modelling studies using fully coupled atmosphere-ocean-land surface models to derive the changes due to anthropogenic and natural climate forcing influences on the atmospheric and oceanic torques and integrate them using the dynamic rotational model of the solid Earth. These are in effect the aims of the project which will be reported here:

- The development of a fully and self consistently coupled atmosphere-ocean model based on the state-of-the-art ECHAM5-T63 atmosphere and the MPIOM ocean model including the tidal forcing from our first project.
- A detailed land surface hydrology model fitted into the fluxes of the internal ECHAM5/MPIOM hydrological discharge model HDM for calculating offline the subterrain water levels and their contributions to the tensor-of-inertia.
- Simulations of the 20th century under observed climate forcing from anthropogenic and natural sources of the coupled model as well as the atmospheric model ECHAM5-T63 forced with observed SST/SIC and climate change simulations for the 21st century with the coupled model under the assumed A1b scenario for the future anthropogenic climate forcing.

This type of modelling approach is sketched in Fig. 1.2.3. Compared to Figs. 1.2.1 and 1.2.2 it clearly shows the increase in complexity. However, the comparison of the results with each other and with the observations shows that this increase in complexity has led to a clear increase in realism. This will be documented in more detail in the next chapters

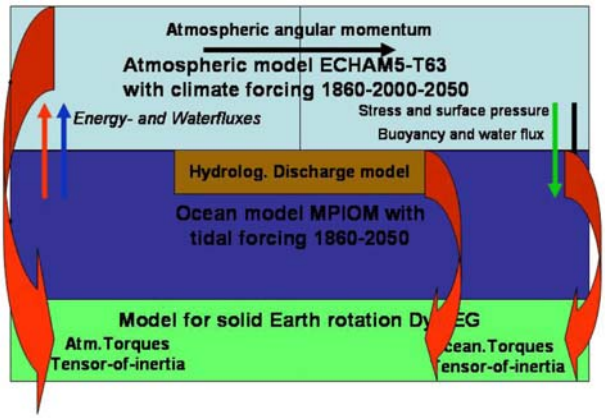

Fig. 1.2.3: Symbolic layout of the modelling approach during the third project phase

2. Models of subsystems

First, it should be reemphasized that the main objective of the project was to develop an integrated model of the subsystems atmosphere, ocean and continental hydrosphere (ECOCTH). Thereafter, on the basis of the obtained spatial and temporal data fields the dynamical Earth model DyMEG should calculate the respective rotation parameters, the gravity field, and the shape of the Earth and their variability (see Fig. 1.2.3). Only such a coupled model can guarantee the mass, energy and momentum fluxes between the subsystems to be steady and the Earth system parameters to be consistent. Differently from the singular treatment of a subsystem (where the influence of another subsystem will be prescribed by observed boundary values) the integrated approach does not use data assimilation; so principally the approximation of real nature might be somewhat inferior. On the other side, the fundamental physical properties are conserved in the coupled system and this is necessary for a consistent calculation of Earth system parameters. Moreover, only such a model can be run in a prognostic way for decades, because it does not need boundary conditions at interfaces (with the exception of the solar radiation, volcanic forcing and emission scenarios for anthropogenic climate forcing contributions which, of course, must be prescribed).

Nevertheless, for different reasons a preceding or partially simultaneous treatment of separate subsystems stand-alone runs made still sense. Firstly, the pioneering development of a free coupled model including ephemerides tides represented a certain risk while the sub-models had been already successfully tested. Indeed, initial difficulties arose when applying the OASIS coupling code. Together with the high computational effort for the five 200 years runs this delay allowed a common analysis and evaluation of results only in the final phase of the project. Moreover, one scientific attraction of the study was just the comparison of the "classical" stand-alone models of the atmosphere, the continental hydrosphere and the ocean with the new integrated model, with respect to both, specific meteorological, hydrological and oceanographic parameters, and simulations

with the DyMEG model. So, specifically the working groups meteorology and hydrology performed own experiments with the sub-models ECHAM and HDM, see sections 2.1 and 2.3. The working group oceanography has focussed its activities on the coupled model ECOCTH and did no new runs of the oceanic sub-model OMCT. The comparison between both models is based on results which have been produced by OMCT in the preceding project, see section 2.2.

2.1 Atmosphere models ECHAM

General circulation models are able to simulate mass movements and mass concentrations on a global scale in a realistic way. Due to enormous mass displacements and motions relative to the rotating Earth the atmosphere and oceanic hydrosphere have an important impact on the Earth's rotation. Simulations of an atmospheric stand-alone GCM have been conducted additionally within the project. The coupled and the standalone runs were driven by the same solar variability and greenhouse gas concentrations. The standalone run offers the possibility to clearly distinguish between oceanic and atmospheric effects as both subsystems are not directly coupled. As the stand-alone runs are additionally driven by observed Sea Surface Temperatures (SSTs) and Sea Ice Concentrations (SICs) these runs can be regarded as "perfect ocean" runs. A comparative validation of the coupled and stand-alone simulations is helpful to perceive sources of deviations.

2.1.1 ECHAM5

This project work concentrated on the ability of global GCMs to reproduce global angular momentum and global moment of inertia variations associated with changes in the Earth's rotation. The version of the stand-alone atmospheric GCM and the atmospheric part of the coupled model is ECHAM5.3.02 (ROECKNER et al., 2003). The ECHAM model chain was originally derived from the ECMWF (SIMONS et al., 1989) numerical weather prediction model and further developed at the Max Planck Institute for Meteorology (MPI-M) in Hamburg. In 2003 ECHAM5 displaced ECHAM4 as current atmospheric GCM, two years later it was introduced within the project. ECHAM5's dynamic core calculates the following prognostic variables:

- vorticity
- divergence
- logarithm of surface pressure
- temperature
- mixing ratios of the different water species.

Within ECHAM5 the prognostic equations for temperature, surface pressure, divergence and vorticity are represented in the horizontal by a truncated series of spherical harmonics; for the water components (vapour, liquid, solid) a flux form semi-Lagrangian scheme (LIN and ROOD, 1996) is applied on a Gaussian grid (MESINGER and ARAKAWA, 1976).

2.1.2 Stand-alone atmosphere 20th century simulation

The stand-alone simulations cover the 1880 to 2006 period. As for the atmospheric part of the coupled model, ECHAM 5.3.02 (ROECKNER et al., 2003) in its standard troposphere version is used in the stand-alone simulations. An ensemble of five runs has been created by disturbing the initial conditions. The latter were extracted from a short pre-industrial control run with five-year intervals lasting from 1855 to 1880 (see Fig. 2.1.1).

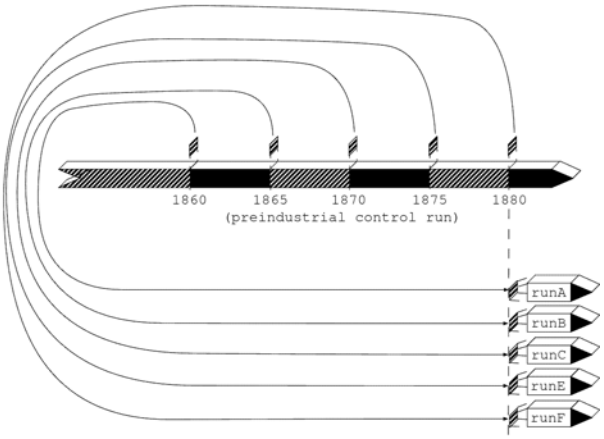

Fig. 2.1.1: Schematic overview of the initialisation procedure.

To obtain realistic states of the atmosphere a broad set of forcing factors was used. It includes greenhouse gas concentrations, an aerosol climatology (TANRE et al., 1984) including volcanic background aerosols, solar variability (FRÖHLICH and LEAN, 1998) and sea surface temperature data as well as sea ice concentration data from the Hadley Centre's reconstruction (RAYNER et al., 2006).

The aerosol climatology is a three-dimensional field depending on time. In the model both the direct (radiation) and first indirect effect (condensation nucleus) are accounted for (KRISTJÁNSSON et al., 2005). Volcanic aerosols have a fixed spatial distribution.

The spatial resolution of the model in this study is T63 in the horizontal and 31 layers in the vertical with the 10 hPa level defining the top of the model atmosphere. A T63 resolution represents a global grid consisting of 192x96 grid points. The distance between two neighbouring grid points is ~1.875°. The time step is $\Delta t = 20 min$. The model output is stored every six model hours and contains all necessary information to derive all variables of the ECHAM5 GCM.

Preparation of SST and SIC Data

To avoid a systematic underestimation of variance when linearly interpolating from monthly means which is the temporal resolution of the Hadley Centre's reconstruction to daily values – as the model expects as input – a filter has been applied to the SST and SIC data (TAYLOR et al., 2000). Fig. 2.1.2 is a fictitious illustration of the Taylor filter applied to monthly mean SST data for a Northern hemisphere grid point. It is indicated that variance is added to the data to face the problem of underestimation, the filtered SSTs are also called "pseudo SSTs". When calculating monthly mean values from the daily values gained from linear interpolation of "pseudo SSTs" one would re-obtain the original Hadley Centre values. A boundary condition of the filter is the conservation of monthly mean values. Thus the method of applying the filter to the data is far more superior instead of directly interpolating the Hadley Centre's reconstructions.

Fig. 2.1.3 shows the difference/correction between "pseudo SSTs" and the original Hadley Centre data for one time step. Regions with high temporal variance generate the highest magnitudes in difference – namely Northwest Atlantic and Northwest Pacific as well as regions just beside the ice border.

March is frequently the coldest month for many sites of the Northern hemisphere. As the second order derivative therefore tends to be positive in March for the Northern Hemisphere and negative for the Southern hemisphere there is a dependence on latitude concerning the algebraic sign of the correction. In most areas the correction is below 0.2K.

The map in Fig. 2.1.3 displays a strong positive correction in the Southwest Atlantic near the Uruguayan coast.

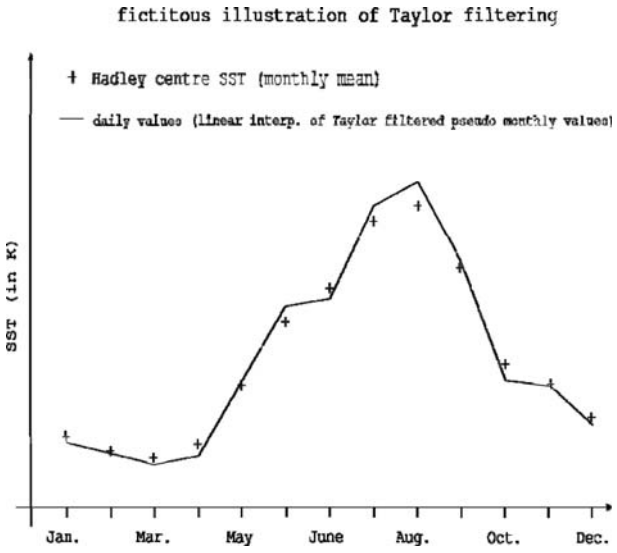

Fig. 2.1.2: Schematic annual cycle of a Northern hemisphere grid point

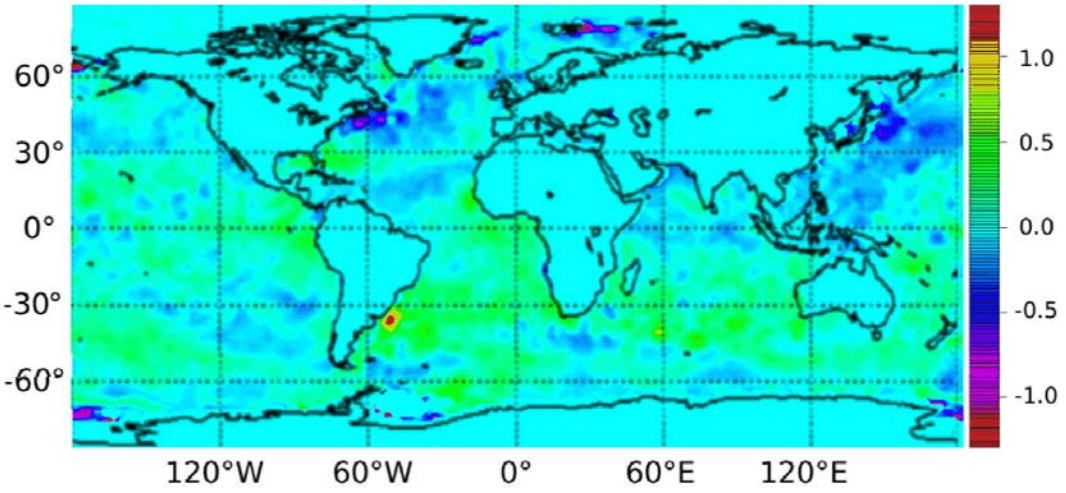

Fig. 2.1.3: Top: difference between Taylor filtered "pseudo SSTs" and Hadley Centre data for March 2003 (in K)

2.1.3 Results

In this chapter the model output of the ECHAM5 ensemble stand-alone simulation will be analysed. The closer distributions of meteorological parameters match "real" values, the higher is the confidence in a good representation of the angular momentum budget. As the stand-alone atmospheric GCM is identical with the atmospheric part of the coupled model, this analysis is also a validation of the atmospheric part of the coupled model. The project work focussed on the angular momentum variations within the GCM, anyhow other meteorological parameters within the model's output should have "realistic" values. "Unrealistic" states in global temperature or pressure distribution would induce unrealistic AAMs implying that the simulations are useless for the purpose of this study. The brief model validation against reanalysis and observed data which follows compares temperature distributions in time and space.

Strong departures from observed temperature would be a good indicator of inconsistencies in the energy budget as temperature is directly linked to energy by the first law of thermodynamics describing energy balance. The global mean 2m temperature over land is compared to observed or reconstructed values from the Climate Research Unit (CRU) (JONES et al., 1999; RAYNER et al., 2003) (Fig. 2.1.4). Over sea a large amount of the variance can be explained by the underlying observed SST which is prescribed as boundary condition. Therefore, a good agreement of observed and simulated values for these grid points is not necessarily obtained due to a good model skill. Thus it is superior to compare land data for validation purpose. Seasonal variations were removed by a LOESS filter. The agreement between the ensemble mean and the observed global 2m temperature anomaly time series is very reasonable. Although the inter-quantile range (IQR) (blue band) is fairly small and rarely greater than 0.1 K which implies a high model certainty, the observed temperatures lie within the IQR for most of the time. High frequency fluctuations are well captured, this hints at a good SST excitation as the SST forcing is the most effective external driver to induce variability on annual and inter-annual time scales. Low frequent patterns also agree well with solar and greenhouse gas forcing as main external drivers. The current warming which started in the 1970s matches the observation in time and amplitude. Since 2000 to present the temperature anomaly of the ECHAM simulation is mostly lower than that of the CRU.

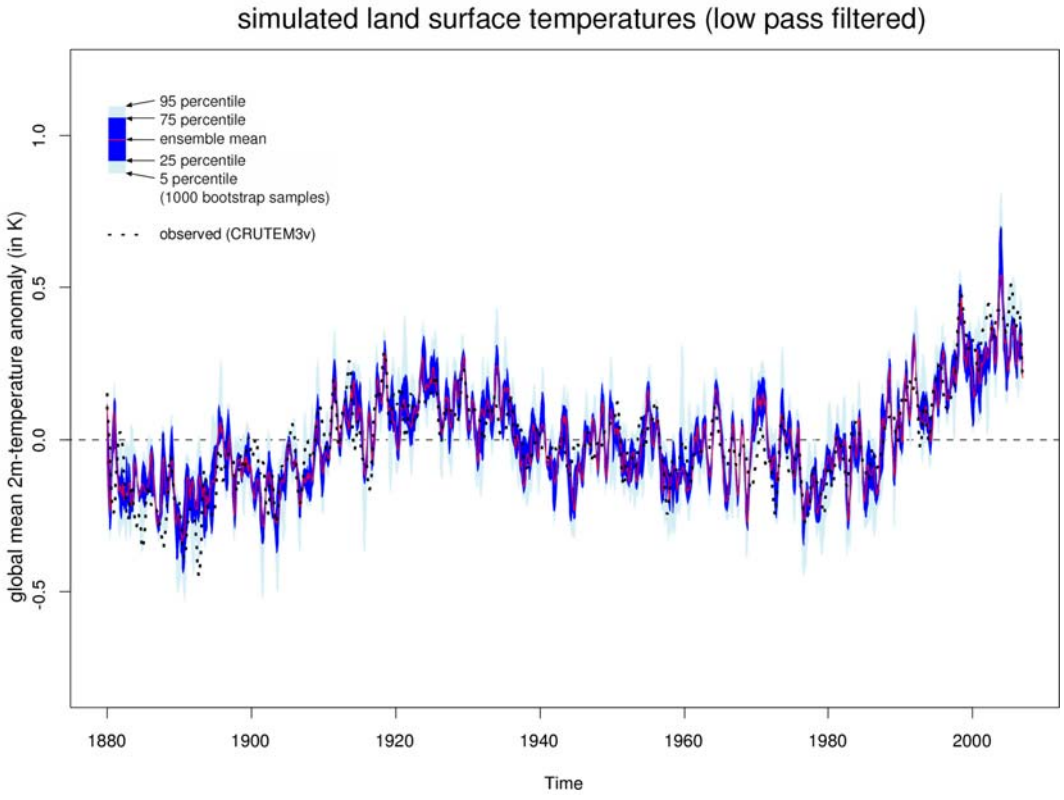

Fig. 2.1.4: Simulated ECHAM5 ensemble mean (blue shadings, red line) and observed global land 2m temperature anomalies (dashed black line) – 12 month bandwidth LOESS smoothed.

When investigating the spatial distribution of certain parameters, reanalysis data form the only reference being available for several decades.

As reference epoch the entire ERA40 (UPPALA et al., 1999) period from 1958 to 2001 is respected. Means over all Januaries and Julies are calculated as well as standard deviations for every grid point and compared to the arithmetic mean of all ensemble members (the ensemble mean) and the mean standard deviation. The reanalysis data is available with a T159 spectral resolution corresponding to a 480x240 Gaussian grid. The grid resolution is finer by factor 2.5 resulting in a number of grid points which is 6.25 times higher. For comparability reasons the ERA40 data has been interpolated to the ECHAM5 grid.

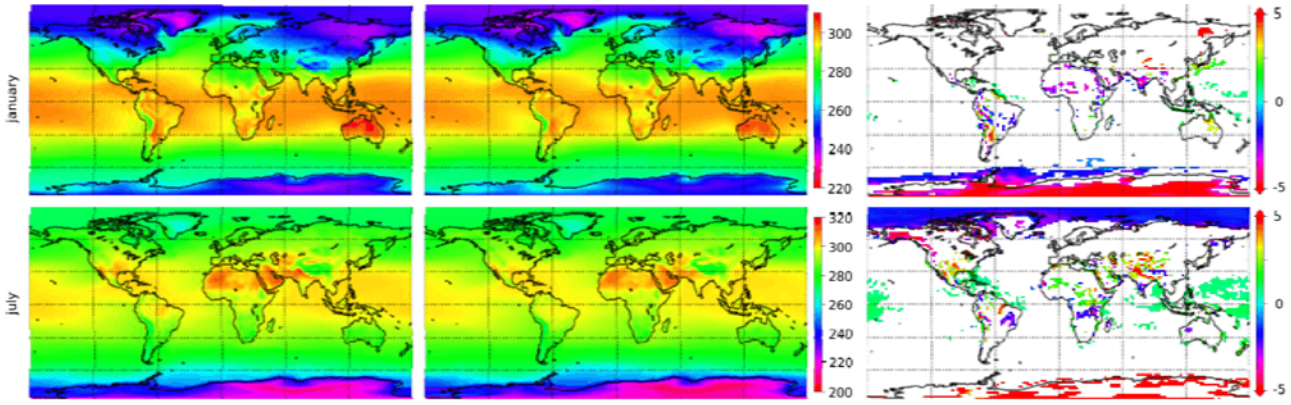

Fig. 2.1.5: Top row: January mean 2m temperature 1958 to 2001 (in K); bottom row: July mean 2m temperature 1958 to 2001 (in K), first column: ECHAM5 ensemble mean; second column: ERA40 and third column: difference between ECHAM5 ensemble mean and ERA40 (ECHAM5-ERA40) tested by a discriminant analysis on five percent significance level (insignificant differences are whitened).

The third column in Fig. 2.1.5 shows the difference between the ECHAM5 ensemble mean and the ERA40 reanalysis data. In general the number of grid points showing a significant difference in January mean temperature is small. In July some grid points over sea in the inner tropics are overestimated significantly by ECHAM5. Of course over sea the underlying SST forcing determines the 2m temperature substantially. Therefore a high consonance is expected. Over land the situation is diverse. Systematic significant differences are present in very high latitudes during summer, particularly over sea ice covered regions ECHAM5 underestimates temperature. Perhaps the snow/ice albedo is set too high within the model. Over Antarctica the difference exceeds five Kelvin at some locations. During winter ECHAM5 tends to overestimation of the 2m temperature in these regions.

Generally the global patterns are consistent with each other. For instance the East Siberian cold pole or the heat of the Australian outback are well pronounced for January. A west-east temperature gradient over mid-latitude winter continents is as well implied in the model pointing at a realistic general circulation.

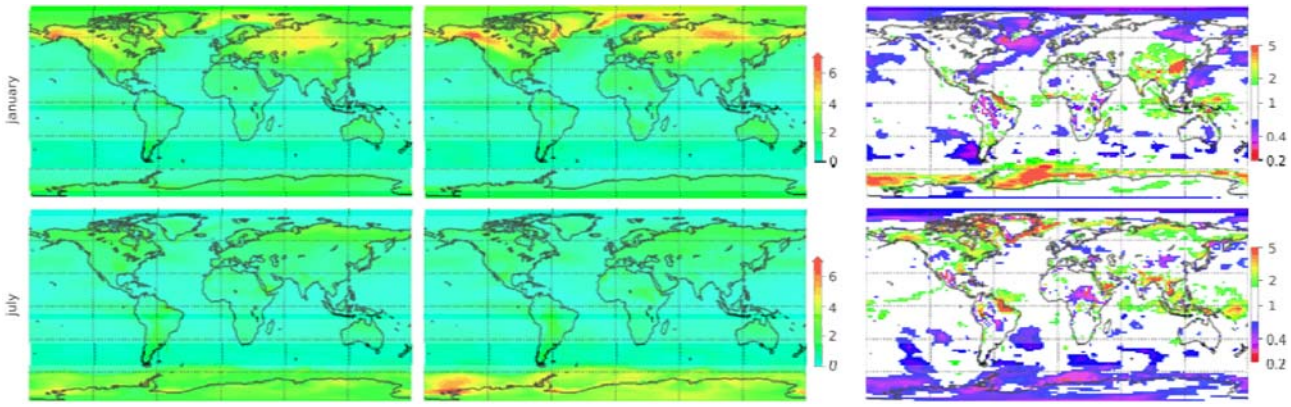

Fig. 2.1.6: Top row: January standard deviation of 2m temperature 1958 to 2001 (in K); bottom row: July standard deviation of 2m temperature 1958 to 2001 (in K), first column: ECHAM5 (mean over all members); second column: ERA40 and third column: difference between ECHAM5 and ERA40 (ECHAM5-ERA40) tested by F-test on five percent significance level (insignificant differences are whitened).

A closer look at the temperature variability is obtained by the standard deviation of the January and July temperature for every grid point (Fig. 2.1.6). As the variability of the ensemble mean is reduced by averaging, the mean standard deviation of all ensemble members is displayed. The variability of ocean grid points is comparatively small in ECHAM5 and ERA40. The highest amplitudes in standard deviations are found at winterly continental areas and along the sea ice border. The physical background can be explained by sensible heat fluxes. Over the open sea the sensible heat flux from the surface to the atmosphere is very strong in arctic winter and traps the 2m temperature close to the freezing point. Whereas over sea ice the sensitive heat flux is reduced dramatically and temperatures drop well below zero. Therefore the standard deviation of sea concentrations and the one of 2m temperature correlate well in this region.

The differences (third column of Fig. 2.1.6) between ECHAM5 and ERA40 standard deviations are small for the majority of grid points. Preferentially over sea a significant systematic underestimation for winter and overestimation for summer at high latitudes can be seen. Nevertheless the variability of the ERA40 data is very well captured by the model resulting in small differences of the standard deviation for most of the sites.

To conclude this chapter and this short model analysis, it is stated, that the deviations seen are predominantly of local nature. The global integrals hardly show any deviations (see Fig. 2.1.4). The quality of the model as far as it is assessed by the analysis here is absolutely adequate pertaining to the purpose of global angular momentum analysis.

2.2 Ocean model OMCT

The first version of the Ocean Model Circulation Tides (OMCT) descend from the Hamburg Ocean Primitive Equation Model (HOPE) (WOLFF et al., 1996; DRIJFHOUT et al., 1994). It was extended by an explicit forcing of the lunisolar tides, the self-attraction and loading effect and the steric sea level correction (THOMAS, 2000).

The tidal forcing comprises the complete lunisolar tidal potential of second degree. The potential is not divided into partial tides, instead the 'full' potential is derived at every time step from the instantaneous position of Sun and Moon. This real time excitation of ocean tides allows for nonlinear interactions between ocean tides and the ocean circulation. The ephemerides are determined with an approximated formula described in detail by VAN FLANDERN and PULKKINEN (1998).

The loading and self-attraction effect is implemented in a parameterized form. The parameterization is derived from the barotropic case (ACCAD and PEKERIS, 1978), where the secondary potential caused by loading and self-attraction is approximated through

$$\Phi_{LSA} = g\,\varepsilon\,\zeta\,,$$

where g is the mean gravitational acceleration, ε is a proportionality factor and ζ the sea surface elevation. In order to include baroclinic effects the approximated formula is rewritten as (THOMAS et al., 2001)

$$\Phi_{LSA} = g\,\varepsilon \int_{-h}^{\zeta} \frac{\rho(z)}{\rho_0}\,dz\,,$$

where h is the ocean depth, ρ_0 a reference density and z the vertical coordinate.

The steric sea level correction is implemented in order to allow for mass conservation. This correction is necessary since the OMCT model is a z-coordinate model and thus the model is volume conserving and not mass conserving. In order to allow for mass conservation a correction term was introduced by GREATBATCH (1994). There, the sea level is horizontally homogenous corrected, by

$$\delta\zeta = \frac{1}{S}\int_V \frac{\delta\rho}{\rho_0}\,dV\,,$$

The sea surface is S and $\delta\rho$ is the density anomaly. In the OMCT this correction is extended by a spatial dependence written as

$$\delta\zeta(\varphi,\lambda) \;=\; -\int_{-h}^{\zeta} \frac{\delta\rho(\varphi,\lambda,z)}{\rho_0(\varphi,\lambda,z)}\,dz\,.$$

This sea level correction is applied after each time step to the global sea level field.

For the second version of the OMCT the basis is the updated version of HOPE, the Max Planck Institute Ocean Model (MPI-OM). The main advantage of the MPI-OM is that it utilizes horizontally a bipolar orthogonal grid where the positions of the North and South pole can freely be chosen. Thus, the singularities at the geographical North pole can be avoided by replacing the grid North pole on land. In this configuration the North pole is centred on Greenland (30°W, 80°N) and the South pole on Antarctica (30°W 80°S). The horizontal resolution of the grid ranges from three to one degree, between 12 km near Greenland and 180 km in the tropical Pacific. Vertically the grid has 40 layers, where 20 layers are distributed over the upper 700 m; partial grid cells resolve the bottom topography. Additionally the subgrid scale parameterization of mixing has been advanced by the implementation of a bottom boundary layer slope convection, based on an isopycnic diffusion scheme and a Gent and McWilliams style eddy-induced mixing parameterization (GENT et al., 1995). Further, a dynamic-thermodynamic sea ice model is embedded in the MPI-OM. A detailed description of the MPI-OM can be found in MARSLAND et al. (2003) and JUNGCLAUS et al. (2006). With the OMCT2 we did not perform stand-alone runs since we are focussing on the coupling to the atmosphere model (compare Chapter 3.1). Extensive analysis concerning the oceanic influence on the Earth's rotation with the stand-alone version of the OMCT1 are performed and published in THOMAS (2000).

2.3 Hydrological Discharge Model HDM

2.3.1 Continental hydrology modelling

In the global water cycle the continental hydrology links the atmosphere with the ocean through water transport processes over land surfaces. It reflects the water distribution in rivers and lakes, groundwater storage, soil moisture and water accumulated as snow and ice as well as water in the biosphere. Although the continental water masses represent only 3.5% of the global water masses in the hydrological cycle, their redistribution and retention mechanisms

affect significantly global integral Earth parameters, such as Earth rotation, the Earth's shape and its gravity field. Knowledge of continental water mass storage and freshwater runoff into the ocean is also essential for the reliable representation of consistent physical fluxes among the atmosphere, the oceans and continental hydrosphere, especially in the focus of a dynamically coupled global climatologic system.

To simulate continental water mass redistribution and to close the global water cycle in the atmosphere-hydrosphere system consistently, the Hydrological Discharge Model (HDM; HAGEMANN and DÜMENIL, 1998a,b) has been applied. For this, several extensions to the existing HDM were necessary. HDM as a discharge model exclusively describes the lateral water flow processes. It requires input data separated in runoff and drainage, contributing to the internal overland flow and base flow respectively. Unlike the atmospheric climate model ECHAM, the weather models from ECMWF and NCEP and corresponding reanalysis data do not directly provide these forcing data sets appropriate for the HDM. Therefore, a second sub-model, describing the land surface processes, has to precede the HDM. The so-called Simplified Land Surface scheme (SLS; HAGEMANN and DÜMENIL-GATES, 2003) allows a separation of precipitation rates into snow accumulation, soil moisture, surface runoff, groundwater drainage, and evaporation back to the atmosphere.

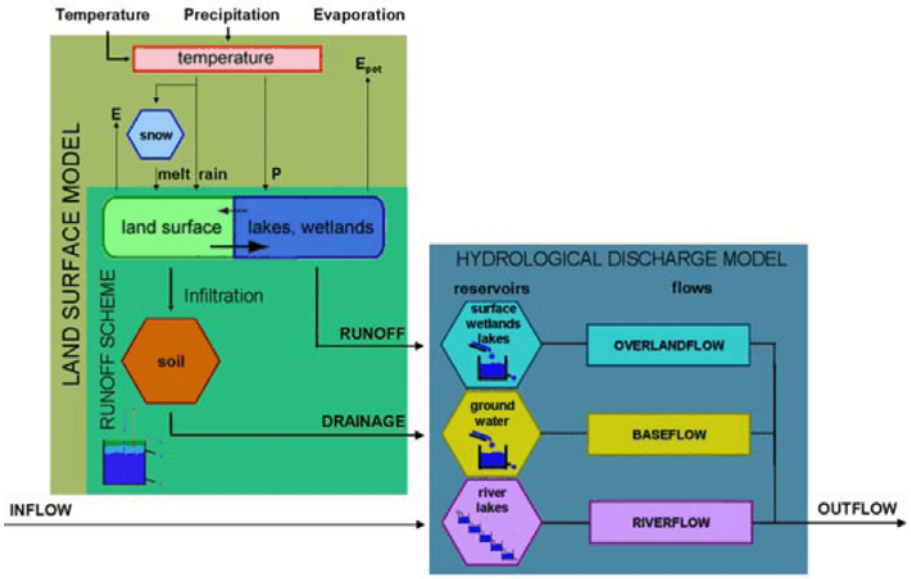

Fig. 2.3.1: Continental hydrological model: Combination of land surface model SLS with discharge model HDM.

2.3.1.1 SLS model component

The Simplified Land Surface scheme is based on the land surface parameterization of the atmospheric climate model ECHAM4 interpolated to a global 0.5° x 0.5° grid. Within each grid cell the incoming precipitation is separated into rain and snow depending on a temperature model according to WIGMOSTA et al. (1994). Snowmelt is estimated with a degree-day factor approach assuming that melt rates are linearly related to the air temperature, like in the model from the Hydrological Bureau Waterbalance (HBV) at the Swedish Meteorological and Hydrological Institute (SMHI) (BERGSTRÖM, 1992). Melt water runoff is delayed by the water holding capacity of snow. Retaining rain or melt water in the snow-pack is allowed to refreeze gradually when temperature decreases below 0° C. Melt water and rain is merged as throughfall reaching the soil. It is separated into surface runoff (fast runoff) and water that may infiltrate into the soil by an improved Arno scheme (DÜMENIL and TODINI, 1992). Additionally drainage (slow runoff) is the amount of water that percolates downwards through the soil. The actual evaporation is derived from potential evaporation estimates using soil moisture capacities and vegetation indices (ROECKNER et al., 1992). Potential evaporation is computed according to the Thornthwaite formula (CHEBOTAREV, 1977) taking annual mean temperature characteristics into account.

Runoff and drainage fields of the SLS model can be passed down to the HDM like the comparable output fields of ECHAM simulations.

2.3.1.2 HDM model component

The HDM simulates the lateral water fluxes by three different parallel types of flows. Water produced within a catchment or gridbox, reaching the land surface by rain or snowmelt as throughfall enters HDM as surface runoff or groundwater drainage. Surface runoff and interflows are merged and fed to the overland flow. Groundwater percolated in the deep soil layers is treated as drainage input, and is passed laterally as base flow. Water entering the catchment from other catchments through the boundaries is transferred by the river network and contributes to the river flow. Each of the three flows is represented by a two-

parameter reservoir model, consisting of a cascade of n equal linear reservoirs with globally distributed retention coefficients k.

The river network is represented by a flow direction map, derived from a 5' x 5' topography dataset of the National Geographic Data Centre. One of eight possible outflow directions is allocated to each gridbox of the HDM model. These are the four main directions North, East, South and West and the four diagonal directions North-East, South-East, South-West and North-West. For base flow and overland flow it is sufficient to use a single reservoir representation (n = 1) where the outflow is proportional to the reservoir content. The retention time coefficients are mainly a function of the average slope. River flow is modelled by a cascade of five equal linear reservoirs (n = 5) and the retention time coefficient depends on the topographic gradient as well as the distance in flow direction. River flow requires calculations with a time step of six hours to pay regard to the minimum travel time through a 0.5° gridbox which is limited by the time step chosen. Wetlands and lakes are represented in the same flow types, but the retention time parameterization is based on a renewal rate concept. An additional discharge delay factor accounts for the percental influence of lake and wetland covering parts of a gridbox.

This initial version of HDM has been extended to compute global mass integrals. The vertical water mass balance from the land surface module (soil moisture storage and snowpack) was included as well as the total water storage in each reservoir type and the moving water masses in flows. From the total water storage and the water masses in motion the corresponding angular momentum variations and low degree gravity field changes are estimated with a daily time step. Additionally, a 3-D topography model was included in order to estimate the sensitivity of the model results with respect to the difference between topographic heights and a mean Earth radius.

The quality of the discharge simulation depends not only on the formulations of the model physics and its parameterizations, but also on the precise definition of the boundaries between land, lakes and ocean. This is especially true if global parameters depending on mass integrals like Earth rotation or gravity field are estimated. Unfortunately the underlying land-sea masks of SLS and HDM differ and both are neither adjusted to the ocean models nor to the atmospheric models. As a workaround all hydrological simulations are done only on compatible gridboxes. Omitted water masses are redistributed to the ocean as a homogeneous layer to ensure mass conservation.

The stand-alone hydrological model (SLS+HDM) has been used to analyse the pure hydrologically induced mass redistribution. Afterwards the fully coupled climate simulations have been performed with the model ECOCTH (ECHAM+OMCT+HDM, see chapter 3.1). In ECOCTH a land surface module is integrated in the comprised ECHAM5 model. The newly developed routines for the calculation of vertical and lateral water storage and of the hydrological angular momentum (matter and motion term) have been taken over from the HDM stand-alone version. Due to different model-optimized resolutions mass fluxes have to be interpolated between the sub-systems in ECOCTH. Since standard interpolation schemes are not exact mass conserving, again, mass conservation in the coupled ECOCTH model is achieved by redistributing residual water masses as a homogeneous layer over the ocean. The same method is adapted to water masses not considered in the HDM routing scheme, like big continental lakes and local dips.

2.3.1.3 Atmospheric forcing data

Several types of atmospheric forcing data have been used for the HDM stand-alone simulations: output from the climate model ECHAM4-T42, from NCEP- and ECMWF-ERA-40 reanalyses and from ECMWF operational products. The SLS model has been applied to derive runoff and drainage from the atmospheric precipitation and 2m-temperature fields. As precipitation rates over the northern hemisphere are significantly overestimated by NCEP-reanalyses in spring and summer, climatological monthly mean values from the Global Precipitation Climatology Centre (RUDOLF et al., 1996), covering the period 1961 – 1990 have been used to scale the NCEP reanalyses. Since 2006 improved NCEP-reanalysis data are available covering the period from 1979 to present.

Thus, five different atmospheric forcing data sets for stand-alone simulations with HDM are available, i.e., ECHAM4, NCEP and NCEP2 reanalyses, ERA-40 reanalyses, and operational ECMWF data.

2.3.2 Results

2.3.2.1 Implementation of a 3-D relief model

Compared to the Earth's radius the topographic height variations are very small. For the calculation of surface mass integrals like changes of the hydrological tensor of inertia or hydrological angular momentum (HAM) functions they are usually neglected. To evaluate the influence of the topographic heights on HAM integrals a global 3-D topography model has been introduced. Further, the impact of an ellipsoidal geometry has also been tested.

The influence of the topography on HAM time series is generally below 0.03%, while an ellipsoidal geometry causes anomalies below 0.4% in c_1, 0.2% in c_2, and only 0.06% in ΔLOD. Since these effects are distinctly smaller than other model uncertainties, the spherical approach of the Earth's shape has been retained unchanged in the hydrological model component of ECOCTH.

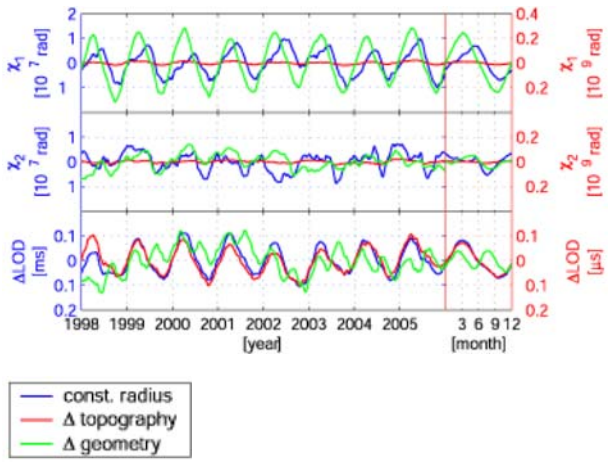

Fig.2.3.2: Influence of topography and surface geometry on hydrological angular momentum functions (HAM). HAM time series assuming a constant Earth's radius of R = 6371000m (blue), impact of topographic heights (red), anomalies resulting from an ellipsoidal approximation of the Earth's shape assuming R_a = 6378137m, R_b = 6356752m (green).

2.3.2.2 Calculation of gravity field coefficients

To calculate gravity field coefficients a subroutine for the expansion into spherical harmonics was implemented in the HDM. Due to the restriction of hydrological water mass variations to the continents and discontinuities at the coasts the spherical harmonic approach causes leakage effects in the oceans (Fig. 2.3.3). Large mass variations in near coastal river basins can leak into estimates of ocean mass variations and vice versa resulting in additional artificial mass signals. The differences between actual water mass distribution and synthesized masses via the spherical harmonic expansion might add up to 10 cm equivalent water heights.

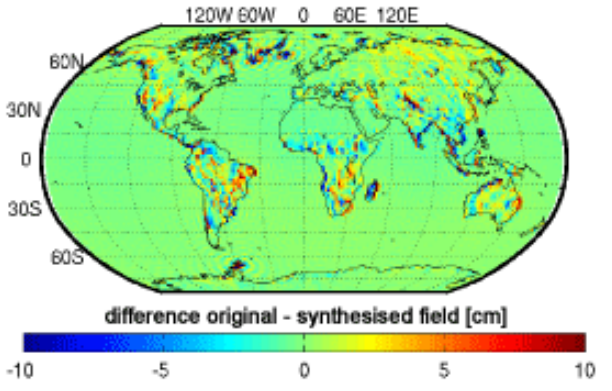

Fig. 2.3.3: Differences between water mass storage from ECOCTH and synthesized field from gravity field coefficients in April 1990 expressed in equivalent water heights.

These leakage effects are avoided by superposing hydrological and oceanic mass distributions before expansion into spherical harmonics. Further analyses of gravity signals due to continental hydrological mass variations will therefore be performed within the analyses and interpretation of the coupled ECOCTH runs and the gyroscopic simulations with DyMEG (see Chapters 3.2, 4).

2.3.2.3 Test simulations and validation of continental discharge with ECHAM4 and NCEP

Simulations of continental discharge with HDM strongly depend on the atmospheric forcing, primarily on the precipitation data. This dependency is more pronounced in models using the SLS component than in models using the ECHAM forcing, because the latter comprehends of a much more complex land surface model including humidity, radiation and wind parameters. The monthly precipitation means of atmospheric models indicate generally a slight overestimation compared to the observed climatologic values from the Global Precipitation Climate Centre (GPCC). While ERA-40 precipitation fields include a positive trend until 1978 correlated with parameter changes in the assimilation background model, the climate model ECHAM produces too low annual precipitation amplitudes, i.e., only 40% of that suggested by GPCC, coming along with less variability. In contrast, NCEP forcing fields generally overestimate annual amplitudes by about 20%. In total, the correlation of monthly mean precipitation rates from GPCC with NCEP is 0.9, with ECMWF 0.8 and with the unconstrained climate model ECHAM 0.4. A detailed description including a principal component analysis of all atmospheric forcing fields can be found in the PHD-thesis of WALTER (2008).

Due to the lack of globally distributed water storage measurements the SLS+HDM model system can only be validated indirectly via the comparison of modelled river discharges with in-situ river runoff measurements. River discharges as simulated with HDM, forced with ECHAM4-T42 (1918-1994), ERA-40 and NCEP (1948-2006) reanalyses (1958-2001), and operational ECMWF analyses (2000-2007) are compared at 142 selected stations with documented runoff data form the Global Runoff Data Centre GRDC. Generally, the test simulations demonstrate the ability of the HDM to reproduce global water storage variations appropriately for Earth rotation and gravity requirements. Again, the quality of atmospheric forcing data is crucial for a realistic simulation of continental discharge. A detailed verification based on statistical analyses has been done by GRIESBACH (2004).

2.3.2.4 Verification of simulated continental runoff (control runs)

In addition to the forced HDM runs mentioned above, continental runoff data from five stand-alone simulations driven by output of ECHAM5 stand-alone runs and from a coupled system simulation with ECOCTH are available.

In general, these simulations underestimate river discharges in low latitudes due to unrealistically low precipitation rates, e.g., in the Amazon catchment. but show very good agreement for all Arctic river catchments. Due to especially high evaporation rates and anthropogenic influences not re-

presented by the atmospheric and hydrological model (e.g., extensive water consumption) discharges of several African rivers are not satisfactorily reproduced. Despite this limitation, the various atmospheric forcing conditions result in significant differences in simulated river discharges. For example, in contrast to the ECHAM4 based HDM simulations the forced ECHAM5 and coupled ECOCTH simulation realistically reproduce episodic discharge characteristics of the Australian river Murray, but the events occur more often than observed by GRDC. However, forcing with reanalysis data from ECMWF and NCEP generally leads to more realistic discharges than simulations driven by climatologic ECHAM data. The coupled model ECOCTH produces slightly lower annual runoff amplitudes than the corresponding HDM stand-alone simulations. In Middle- and South-America, in the Congo basin and in the monsoon regions of South-East-Asia these differences reach up to 20%. A comprehensive comparing statistical analysis of stand-alone HDM runs and output of the coupled ECOCTH simulation is still in progress.

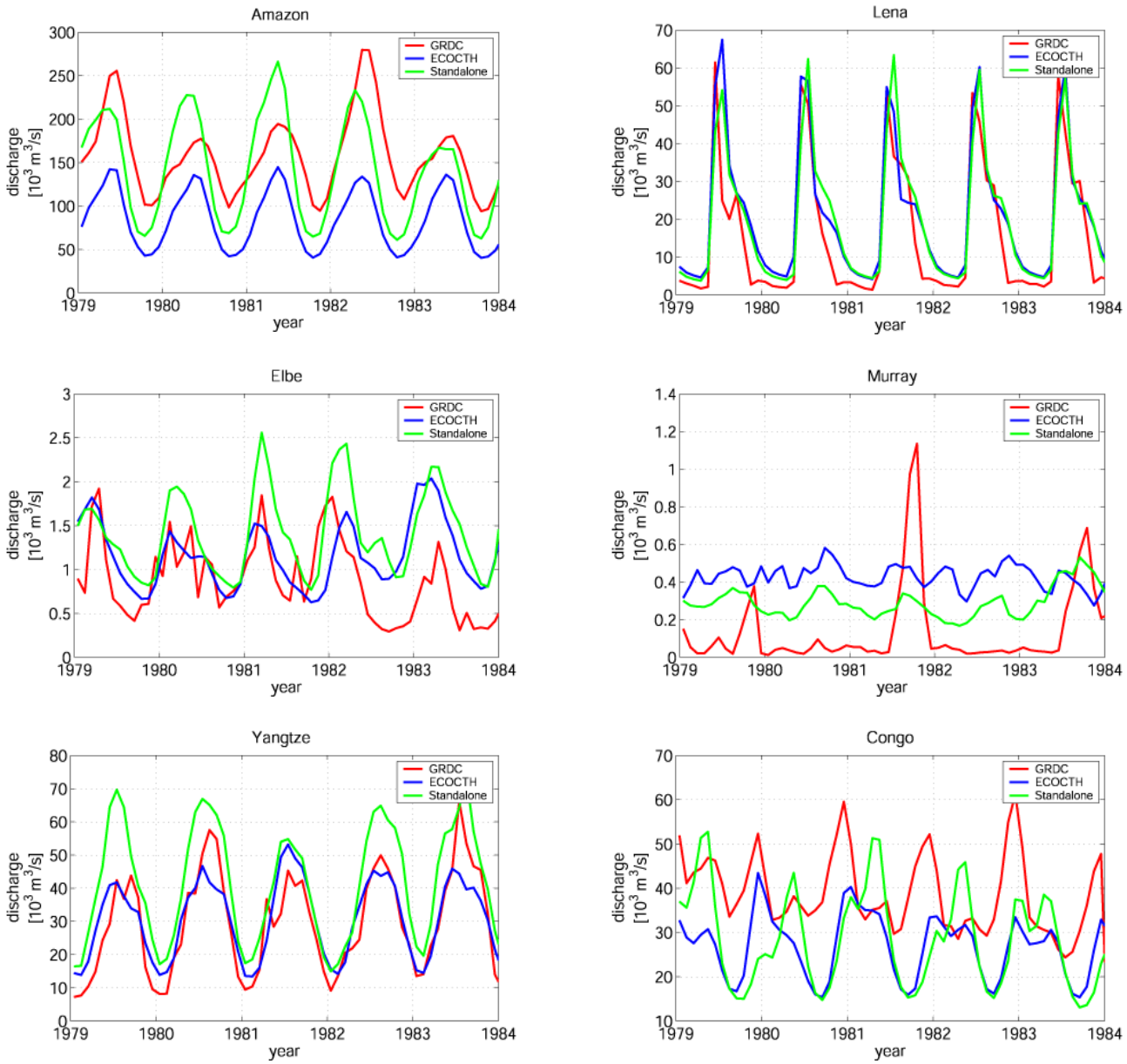

Fig. 2.3.4: River discharge of Amazon, Lena, Elbe, Murray, Yangtze and Congo: GRDC observations (red), HDM stand-alone simulation with ECHAM5 forcing (green), and discharges from coupled ECOCTH runs (mean of five ensembles) (blue).

Since the deviancies of simulated runoff from measured discharges are mainly the result of deficiencies in the precipitation input fields rather than of incorrect model parameterizations, the original HDM default values for retention times, water capacities and vegetation indices as introduced by HAGEMANN and DÜMENIL (1998a) are retained. Significant improvements of simulated continental runoff are expected from the consideration of anthropogenic effects; however, this would go far beyond the scope of this project and has to be tackled in a separate investigation.

Further annual and semi-annual runoff charts as well as detailed explanations for occurring discrepancies between HDM simulations and GRDC data are given by WALTER (2008).

2.3.2.5 Interface adaptation and verification of mass conservation at the boundaries in the coupled model system.

The improved routines of the HDM stand-alone version have been transferred to the coupled model system ECOCTH. To ensure consistent mass exchanges among the sub-systems atmosphere, continental hydrosphere and oceans in the coupled model ECOCTH mass losses due to non-conservative interpolation, differences in land-sea masks, unmodelled continental parts as well as water routed into dips and great lakes are redistributed as additional homogeneous layer to the ocean. This approach has also been adopted to the Arctic and Greenland ice masses, because standard land surface modelling would lead to infinite snow accumulations over glaciated regions.

The analysis of the total continental hydrological outflow determines that the simulated river discharge implies 80% of the fresh water fluxes into the ocean, producing a smooth seasonal signal in HAM and in continental gravity variations. In contrast the residual water masses, redistributed into the ocean as homogeneous layer, cause very high frequency variations of no relevance for the seasonal signal. If the residual waters are not treated correctly, the inconsistent mass balance causes accumulative artificial long-term trends, especially in C_{20}. Therefore, trend analyses of ΔLOD and C_{20} have been used to verify the global water balance among the whole system.

The impact of river runoff on the global ocean circulation and corresponding mass distributions have been estimated by DOBSLAW and THOMAS (2007) by considering continental freshwater fluxes as additional forcing condition in OMCT resulting from HDM stand-alone simulations forced with ECHAM-T42 and particularly with ECMWF. While the sub-monthly mass variability is generally insignificant for GRACE de-aliasing purposes in most oceanic regions, monthly mean mass signals of up to 2hPa occur in the Arctic Ocean during the melt season. Additionally, from total freshwater fluxes due to precipitation, evaporation and river runoff seasonal variations of the total ocean mass have been calculated. Their good agreement with estimates based on GRACE observations suggest that the consistent model combination ECMWF, HDM and OMCT is capable of reproducing mass fluxes among these three subsystems realistically.

2.3.2.6 Validation and analysis of continental water mass transports of ECOCTH

First comparing analyses of ECOCTH results with HDM stand-alone simulations forced by ECHAM5 clearly point out the strong dependency of the modelled water storage variations from the precipitation rates. The simulated precipitation fields of ECOCTH and ECHAM5 show monthly differences of up to 200 mm, mainly in lower latitudes. Generally lower precipitation rates in ECOCTH compared to ECHAM5 are reflected in lower annual river discharge amplitudes. For some river basins like Yangtze and Elbe this reduction is accompanied by a higher agreement with observational data. Although the variability of total continental water masses is lower for ECOCTH than for ECHAM5, too, the latter better agree with GRACE estimations.

Trend analyses of simulated HAM from the first ensemble of five ECOCTH runs discover deficiencies in the treatment of precipitation over ice and its “discharge” to the ocean. The vertical water balance is distorted by infinite snow mass accumulations over Greenland. This problem has been solved for further ECOCTH simulations. Beside the glaciated regions in Greenland the lateral water budget is balanced. Concerning the HDM sub-model simulations the lateral water balance is very stable over long periods.

2.3.2.7 Statistical analysis and validation of simulated gravity field variations

Since gravity field coefficients derived from stand-alone simulations with HDM likely cause non-negligible leakage-effects in the ocean due to discontinuities at the coasts, the harmonic expansion has been performed within DyMEG after superposing the mass distributions of the subsystems atmosphere, ocean and land.

Hence, in contrast to hydrological gravity field coefficients the hydrological angular momentum (HAM) functions do not suffer from continental discontinuities, they yield immediately the preferable global parameters for statistical analyses. Unlike the oceanic angular momentum (OAM) and the atmospheric angular momentum (AAM) the HAM time series are dominated by mass variations, i.e., the matter term, while relative motions of water masses in rivers are subordinated. With the new estimation of the HAM motion term this has been proved and classified for the first time. The dominant contribution in the motion term comes from seasonal variations in river flows with magnitudes three orders lower than the matter term. The impact of overland flows is even five, that of base flows seven orders of magnitude lower and, thus, negligible.

A harmonic analysis of HAM functions reveals annual mass variations and its higher harmonics as the most significant hydrological signals. This corresponds to the annual variation in snow accumulation and soil moisture. Fig. 2.3.5 shows the prograde and retrograde annual and semi-annual

signals of the HAM time series for three simulations with ECHAM4, ERA-40 and NCEP forcing. The magnitudes agree well and reflect the different magnitudes of the forcing fields. However, corresponding phases differ significantly, especially with respect to the annual signal. The reason for this discrepancy might be associated with different land surface modelling resulting in different snow accumulation and soil moisture storage rates.

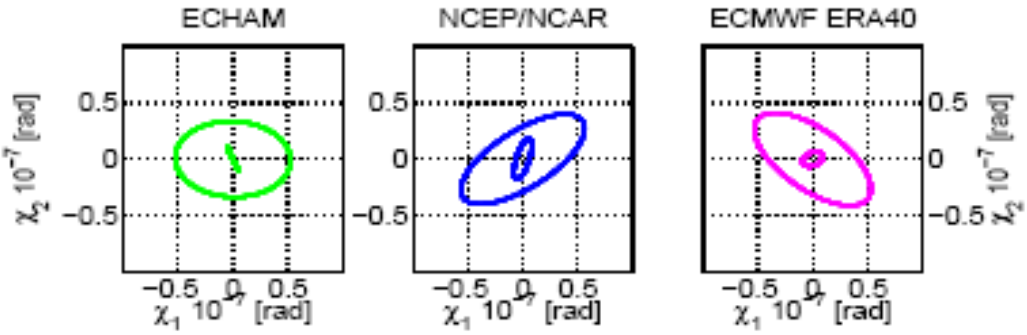

Fig.2.3.5: Annual (big ellipse) and semi-annual (small ellipse) signals in horizontal HAM functions.

Since the ECMWF and NCEP forced HDM simulations are generated with the same land surface model (SLS) the disagreement cannot be exclusively explained by unequal modelling characteristics like the beginning of snow melt, but rather by the dominant dependency from the atmospheric forcing fields, namely precipitation. This is supported by results from other hydrological models using the same atmospheric forcing fields and showing also a wide variance in their phases.

It might be stressed, that any harmonic analysis of HAMs suffers from the periodic but not ideally sinusoidal signals in the time series. Due to snow accumulation, melting, and retention processes the hydrological mass variations are sometimes better illustrated by saw-tooth functions. Any harmonic decomposition of such a signal will result in artificial power shifted to high harmonics. Restricting the harmonic analysis to only one inter-annual period, the semi-annual one, causes unpredictable approximation errors. Aside from the annual period, the semi-annual is therefore not very distinct. Especially the phase estimates and the representation of the equatorial components as prograde and retrograde circular motion are very sensitive to minor changes in the harmonic decomposition. Therefore, it is not surprisingly, that also the first results from the ECHAM5 forcing and from the ECOCTH run show the same variability.

Tab. 2.3.1: Amplitudes, phases and explained variances of annual and semi-annual HAM signals. Simulations forced with ECHAM4, NCEP and ERA-40.

	annual signal			semi-annual signal		
	HS_{ECHAM}	HS_{NCEP}	HS_{ECMWF}	HS_{ECHAM}	HS_{NCEP}	HS_{ECMWF}
χ_1						
Ampl. [10^{-7}rad]	0	0	0	0	0	0
Phase [°]	87	123	105	270	354	354
decl. variance [%]	76	54	64	0	2	2
χ_2						
Ampl. [10^{-7}rad]	0	0	0	0	0	0
Phase [°]	356	75	345	90	305	49
decl. variance [%]	41	16	19	2	2	0
ΔLOD						
Ampl. [ms]	0	0	0	0	0	0
Phase [°]	87	107	88	255	154	196
decl. variance [%]	78	53	26	0	4	1

Nevertheless, harmonic analysis is a common tool to compare seasonal hydrological signals. Keeping the deficiencies of the harmonic approximation in mind the annual signals in the HAM time series from HDM stand-alone simulations (Tab. 2.3.1) have been compared with corresponding runs forced with ECHAM5 and output of the coupled ECOCTH model. The c_1-component of ECOCTH fits very well with 0.50×10^{-7} rad to the HDM stand-alone estimates, while ECHAM5 yields only 0.35×10^{-7} rad. The annual c_2-component of ECOCTH and ECHAM5 is very similar about 0.86×10^{-7} rad, but different from all HDM stand-alone simulations. The c_3-component is also almost

similar for ECOCTH and ECHAM5 and with 0.0084 ms slightly higher than the HDM stand-alone ones.

A more direct representation of the annual variation can be obtained by forming mean annual signals out of several years. In Fig. 2.3.6 the first HAM component demonstrates the accumulation of snow (vertical water balance maximum) until spring and the subsequent entry of melt water into the river network (lateral maximum) in the summer.

Whereas the c_1-component shows generally an obvious seasonal signal, the c_2-component is much lower and turbulent. This is attributed to the fact, that the main hydrological effective regions of North-America and Asia cancel each other in the tensor of inertia element I_{23} reliable for the second HAM component. The remaining signal is affected much more by differences in the precipitation forcing fields. In ΔLOD the seasonal variation of all five simulations agree very well.

Thus, the results indicate that the seasonal continental water mass redistribution is less affected by coupling mechanisms as represented in ECOCTH (compared to HDM runs forced with ECHAM5) than by atmospheric precipitation rates and land surface modelling.

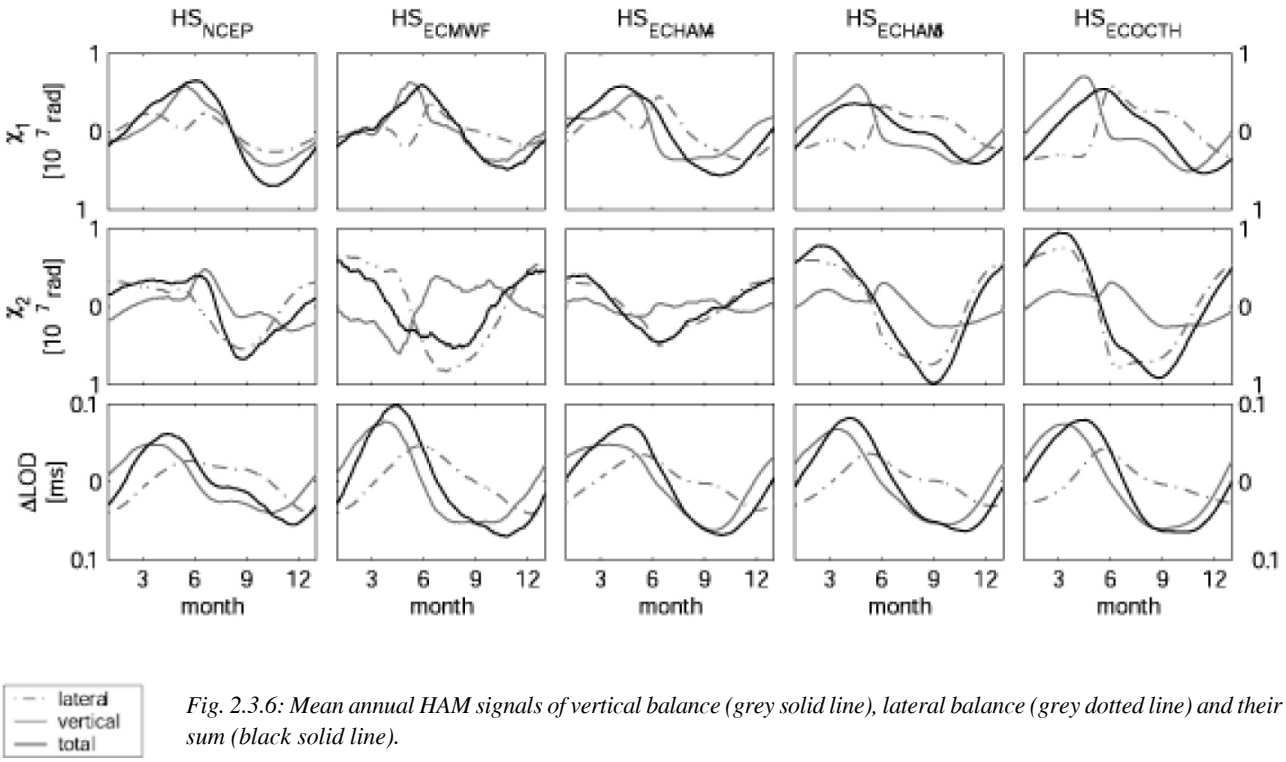

Fig. 2.3.6: Mean annual HAM signals of vertical balance (grey solid line), lateral balance (grey dotted line) and their sum (black solid line).

2.3.2.8 Global water balance

The global hydrological water mass balance can be easily checked by integrating the water masses stored in the oceans, the continental hydrosphere and the atmosphere. Fig. 2.3.7 shows the global sums for the ERA-40 re-analysis data whereas the ocean model treats the ocean mass as constant.

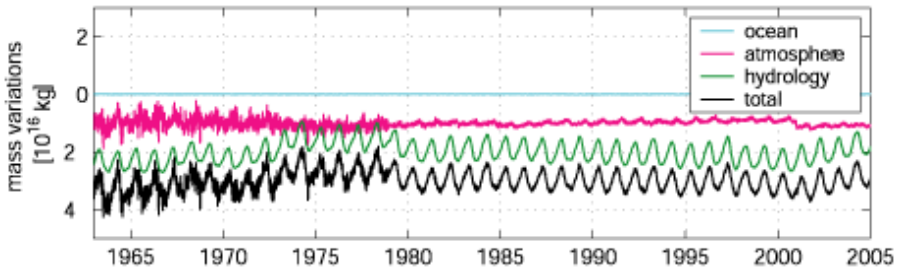

Fig. 2.3.7: Variations of total water masses in the oceans, atmosphere, and continental hydrosphere and the sum of the three sub-systems. Note that the time series of the individual sub-systems have been arbitrarily shifted.

The most obvious mass variation comes from the hydrology with annual amplitudes of $3.83 * 10^{15}$ kg. Due to its storage capability the continental hydrology produces significant runoff delays reflected especially on seasonal time scales. The atmosphere shows much lower seasonal variations with annual amplitudes of $0.46*10^{15}$ kg. The variability of the high-frequency noise in the continental hydrosphere is reduced since 1979 with the introduction of satellite measurements in the ECMWF assimilation technique. The change from ERA-40 to operational data in 2001 provokes a discontinuity in the atmosphere and a trend in hydrology. The changing implementation of VTPR (Vertical Temperature Profile Radiometer) data 1973 – 1978 also affects the global sums adversely.

Assuming a closed water cycle of atmosphere, ocean and continental hydrology the global water mass is constant. Ice masses over Antarctica and Greenland are not considered in the model approach, so far, because no adequate ice model is currently available. Transient mass variations causing trends in length-of-day have been detected in a two-step procedure. First, the sum of continental water storage and ocean was examined only, while. the mass of the atmosphere was assumed to be constant. Continental mass variations were balanced by ocean mass variations distributed in a homogenous water layer. In a second step the atmospheric mass anomalies were distributed, either global over land and oceans or exclusively over the oceans, depending on the reliability of simulated atmosphere-land mass exchange (difference of continental precipitation and evaporation). Fig. 2.3.8 depicts the impact on ΔLOD resulting from these corrections.

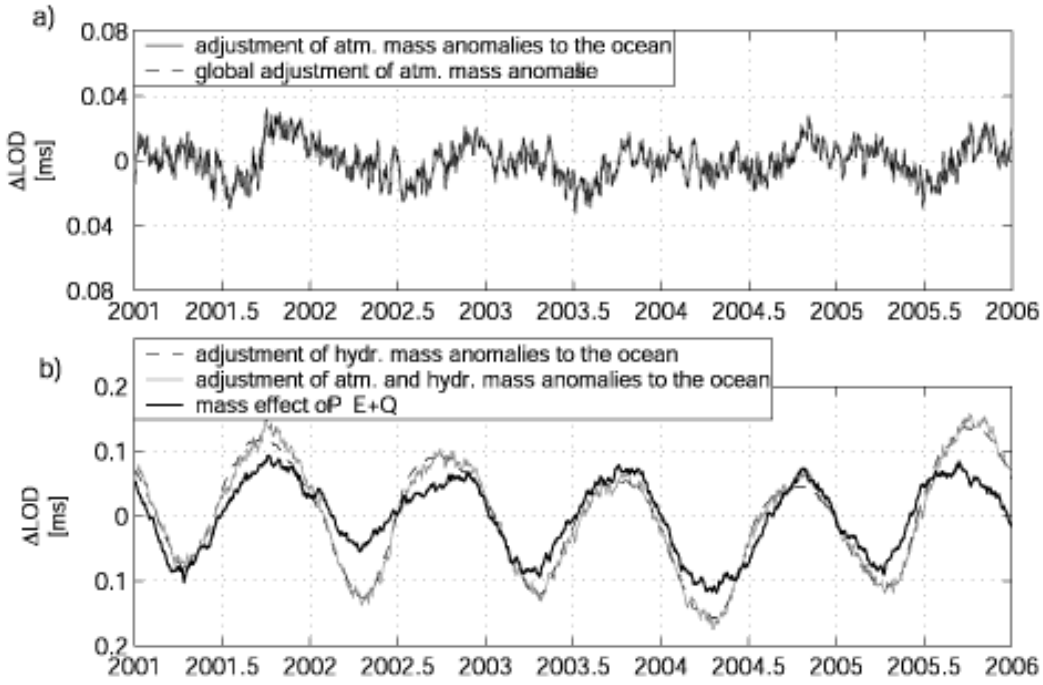

Fig. 2.3.8: Corrections of ΔLOD due to global mass inconsistencies. a) atmospheric mass anomalies. b) hydrological mass anomalies, sum of atmospheric and hydrological mass anomalies distributed over the ocean, effect of freshwater fluxes into the oceans.

Obviously, the impact of hydrological mass corrections is generally significantly higher than the atmospheric ones, and the difference between the global and the oceanic distribution of the atmospheric mass anomalies is very small. As expected the distribution of hydrological masses on the ocean indicates a distinct seasonal signal. To test the approximation of the instantaneous homogenous distribution of the continental runoff over the ocean, the ocean model has also been forced with freshwater fluxes from HDM runs. The seasonal amplitude is about 33% lower, while the phase of the annual signal differs only by 2.5°. These differences can be explained with the additional constraints in the ocean model to keep the annual ocean mass constant (Dobslaw, pers. communication). This constraint is necessary to avoid infinite ocean mass accumulation resulting from unrealistic atmospheric precipitation rates over the ocean as a consequence of an unclosed mass balance of the atmospheric ECMWF analysis data. It is not mandatory that the prognostic atmospheric mass variation matches the diagnostic mass exchange due to precipitation and evaporation.

Angular momentum variations due to hydrological mass redistributions and due to the mass conserving correction partly cancel each other, especially in the equatorial components. The major remaining effect appears in ΔLOD due to the direct dependency on the total water mass in each subsystem.

2.3.3 Summary

The hydrological discharge model HDM is capable of reproducing continental water mass variations on a global scale. The good agreement of modelled gravity field variations with estimates based on GRACE observations suggest that the consistently coupled model ECOCTH represents realistically water mass exchanges among the three Earth subsystems atmosphere, ocean and continental hydrosphere, in particular on seasonal time scales. Furthermore, the coupled model offers the possibility to assess deficiencies in the global hydrological cycle. Inconsistencies in the mass fluxes between the sub-models are accumulated in the global geodetic parameters and reflected as trends. Therefore the long-term quality of the hydrological model suffers particularly from modelling errors in water mass fluxes between the atmospheric model component, land surface model and HDM. The achieved results motivate for further improvements to implement a fully adjusted land surface scheme into HDM. The use of mass-conservative remapping procedures and the adoption of evaporation rates from the atmospheric model will help to avoid mass losses within the land surface processing. Most evident is the problem of the unclosed water balance over glaciated regions. As recently as a convenient ice model can close this last gap in the hydrological cycle coupled climatologic models are able to reliably predict long-term water mass redistributions via global geodetic parameters.

3. Models of the coupled system

3.1. Coupled atmosphere-hydrosphere model ECOCTH

A state-of-the-art climate model is used for the determination of earth rotation parameters. This climate model is modified in order to obtain an earth system model with consistent mass, energy and momentum fluxes. Thus, the influence of all parts of the Earth near-surface system, namely the atmosphere, the oceans and the continental hydrology, on the Earth's rotation can be consistently analyzed on sub-daily to decadal timescales.

3.1.1 Model description

The model chosen is the coupled atmosphere-hydrology-ocean-ice model of the Max Planck Institute for Meteorology Hamburg, which was used for the IPCC fourth assessment report simulations.

The atmosphere model is the European Centre/Hamburg model version 5 (ECHAM5) and it is run at T63L31 resolution (ROECKNER et al., 2003) (Chapter 2.1). The ECHAM5 is coupled via the OASIS interface (TERRAY et al., 1998) without any flux correction to the Max Planck Ocean Model (MPI-OM). This is an updated version of the HOPE model which built the basis for the OMCT (compare Chapter 2.2).

Several modifications are done in order to allow for mass, energy and momentum conservation:

- The OASIS-Interface couples momentum, heat and fresh water fluxes between the atmosphere and the ocean. In the original version of the climate model atmospheric pressure on the ocean surface is not considered by OASIS. We added the 'dynamic pressure' to the coupling variables of OASIS. The 'dynamic pressure' is defined as the atmospheric pressure on the ocean surface and thus the ocean gets explicitly forced by atmospheric pressure.
- The ocean model is extended by a steric sea level correction following GREATBATCH (1994).
- The ocean tides are essential when considering Earth Rotation Parameters, but are still missing in all state-of-the-art climate models. We extended the MPI-OM by the implementation of the complete lunisolar tidal forcing of second degree. This real time forcing describes the tidal potential of second degree in terms of ephemerides (THOMAS et al., 2001) and is the same which was used for the OMCT model (Chapter 2.2). Thus all tidal harmonics of second degree are forced in the model explicitly.

Further, routines are included into the model to compute online the Earth Rotation Parameters from the atmosphere, the ocean and the continental hydrology. The time resolution of the atmosphere and the ocean model are 720 s and 2160 s, respectively. The time-step of the ocean model is reduced compared to the original value of 3600 s for the reliable representation of semi-diurnal and diurnal ocean tides.

Five 200 year experimental runs are performed, with simulation periods from 1860 to 2059. Till the year 1999 the model is forced by observed greenhouse gas (GHG) emissions and pre-calculated sulfate aerosols. For future climate predictions the model is forced by the A1B scenario. For the initial conditions we are using the 500 year IPCC pre-industrial control experiment, where the model was ran with fixed pre-industrial GHG conditions. The state of the Earth system is taken in one hundred year intervals from the control experiment and each of these five states are used to initialize the five experimental runs.

3.1.2 Validation

3.1.2.1 The lunisolar ocean tides

Extracting partial tides by means of harmonic analysis in an arbitrary selected model year indicates that the tidal patterns are successfully represented by the ocean model. Exemplarily the M_2 tidal sea surface elevations are shown in Fig. 3.1.1.

A comparison with the observations of the ST103 dataset (LEPROVOST, 1995) yields that the amplitudes of the obtained tidal sea surface elevations are in good agreement with the observations (RMS amplitude value: 12.9 cm M_2; 4.8 cm K_1). The quality of the tidal patterns is comparable with that of classical tidal models without assimilation of satellite data. The phases are generally delayed. This is most likely through the missing self-attraction and loading effect (MÜLLER, 2008). For ongoing approaches this effect should be included with a parameterization for baroclinic models (THOMAS et al., 2001). For the climate simulations performed in the present study it is not expected that the phase delay will have a significant influence.

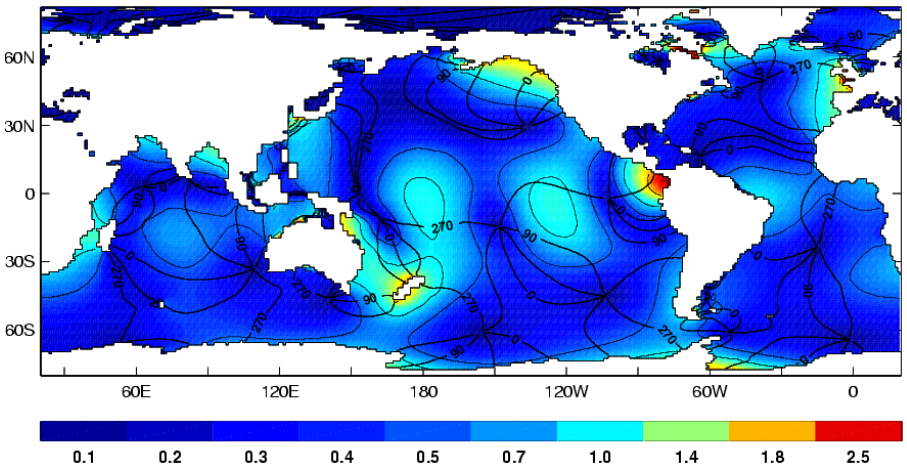

Fig. 3.1.1: Sea surface elevation of the M_2 tide. Amplitudes [m] are color contoured. Solid lines show the phases in degrees.

3.1.2.2 Global ocean circulation

The global ocean circulation is sufficiently represented in the ocean model. The large scale ocean transports can be quantified by the zonally integrated meridional overturning stream-function (MOC). In Fig. 3.1.2 the MOC is shown for the Atlantic sector. The clockwise rotating cell in tropical-subtropical latitudes and in depths down to 2500m represents the formation of North Atlantic Deep Water (NADW). The counter-clockwise rotating cell in depths near the ocean bottom is associated with the Antarctic Bottom Water. The maximum of the NADW cell is of 18.5 Sv at about 40°N and compares well with the observational estimate of 18 Sv (TALLEY et al., 2003). Further visible are the Ekman cells in the upper 500m.

The horizontal barotropic stream-function, shown in Fig. 3.1.3, represents the horizontal transport of water masses. On the Northern Hemisphere the western boundary currents, namely the Kuroshio and Gulf Stream, in the Pacific and Atlantic are presented, respectively. Both currents transport warm tropical water northward towards the polar region. These currents are part of the subtropical gyres with clockwise circulation on the Northern Hemisphere. In polar regions at around 60 degree the subpolar gyres form counter-clockwise rotating circulations, seen in Fig. 3.1.2 as negative values of the barotropic stream-function.

The subpolar circulation in the southern hemisphere is dominated by the Antarctic Circumpolar Current (ACC) in the Southern Ocean. It connects the Indian, Atlantic and Pacific Ocean since there are no landmasses breaking up the Southern Ocean. The strength of this current is measured in the Drake Passage, the passage between South-America and Antarctica, and is about 165 Sv.

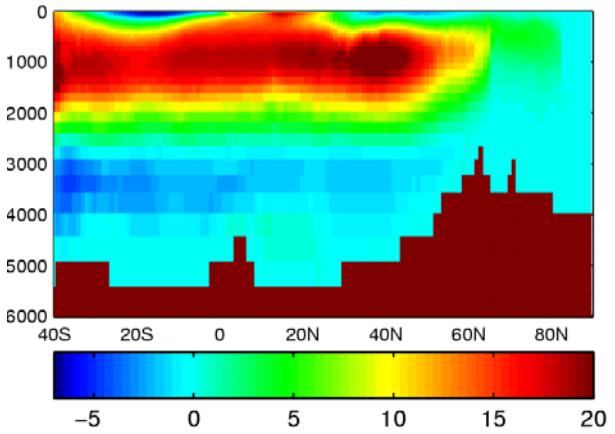

Fig. 3.1.2: Zonally integrated stream-function of meridional overturning in the Atlantic [Sv]

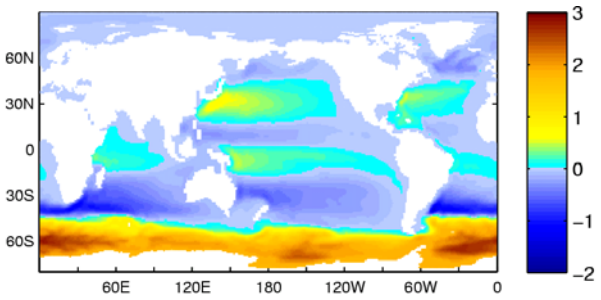

Fig. 3.1.3: Horizontal barotropic stream-function [100 Sv]

3.1.2.3 Tropical variability and global warming

The inter-annual variability of the Pacific Ocean, the El Niño – Southern Oscillation (ENSO) is an coupled ocean-atmosphere phenomenon. El Niño (EN) describes the temperature fluctuations in surface waters of the tropical Eastern Pacific Ocean. The atmospheric signature, the Southern Oscillation (SO), is represented by a monthly or seasonal fluctuation in the air pressure difference between Tahiti and Darwin, Australia. The interplay of the ocean and the atmosphere determines the irregular appearance of EN events.

The coupled ocean-atmosphere model ECHAM5/MPI-OM is able to simulate the tropical variability properly in space and time (JUNGCLAUS et al., 2006). An intercomparison of 20 IPCC AR4 models yielded that the ECHAM5/MPI-OM coupled model produces relatively realistic ENSO variability (VAN OLDENBORGH et al., 2005). However, the magnitude of the SST anomalies is overestimated in the model by a factor of three. The dominant frequency of ENSO is between 3.5 and 4 years and compares well with observational results.

The observed global warming since the mid-twentieth century is consistently represented in the climate model. It shows an increasing of the global averaged surface temperature of the Earth's near-surface air and ocean.

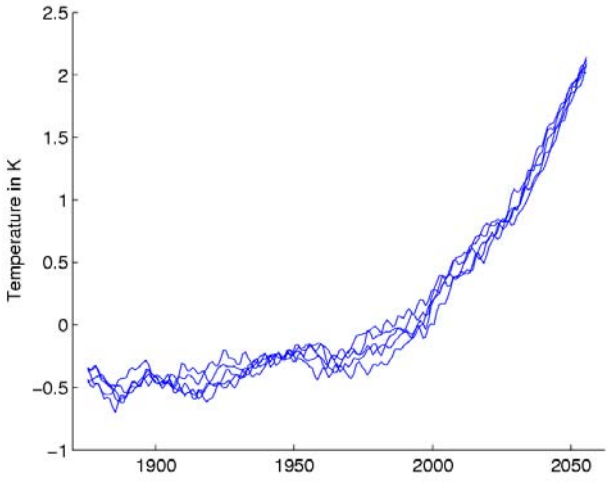

Fig. 3.1.4: Global mean surface temperature anomaly in [K] relative to 1960-2000 of five SRES A1B scenarios.

The future projection, based on the emission scenario A1B with the assumption that a future world will have more global economic growth, indicates that the average global surface temperature will likely rise a further two degree during the first sixty years of the twenty-first century (Fig. 3.1.4).

3.1.3 Results

For all five experimental runs performed with the climate model the corresponding Earth Rotation Parameters are computed and allow for a detailed analysis on the variability of the Earth's rotation. Further, the IPCC A1B future projection enable a description of secular changes of the Earth's rotation in a warming climate. In the following the contribution of the atmosphere, the ocean and the continental hydrology to inter-annual variations and secular trends in length of day and polar motion are analyzed.

3.1.3.1 Inter-annual variations and secular trends in length of day

Changes in the length of day (LOD) are caused through pressure torque induced by zonal pressure gradients on the solid Earth, through changes in the moment of inertia of the coupled system (matter term) and through changes in the angular momentum stored in the ocean and atmosphere (motion term). The motion and matter terms are analyzed in the following sections.

The motion term

The motion term is defined by the angular momentum stored in the ocean and atmosphere:

$$L_1 = R \int_V \rho u(\varphi, \lambda) \cos\varphi \, DV$$

where u are the zonal velocities of fluid elements with density ρ, R is the distance to the Earth's center and φ and λ are geographical coordinates. Solely the zonal ocean currents and atmospheric winds cause changes in LOD. The LOD is written as

$$\Delta LOD = 86164\,s \; \frac{L_1 - L_{1(t=0)}}{L_1^E + L_1} \quad ,$$

where L_1^E is the angular momentum of the solid Earth.

The major zonal ocean current is the Antarctic Circumpolar Current (ACC, Chapter 3.1.2.2) and indeed variations in the motion term are mainly controlled by changes in the magnitude of the ACC (BROSCHE and SÜNDERMANN, 1985; SEGSCHNEIDER and SÜNDERMANN, 1997). In Fig. 3.1.5b the variation of the ACC, measured in the Drake Passage, and the LOD variation induced by the motion term are shown. The magnitude of the ACC shows an inter-annual variability with an amplitude of around 5 Sv and induces LOD variations of up to 10^{-5}s. The correlation map in Fig.

3.1.5a shows the correlation of the horizontal barotropic stream-function and the LOD variation. The highest correlations are in the Southern Ocean close to the coast of Antarctica, where the ACC is strongest. This clearly supports previous studies and shows that the ACC determines to a large extent the LOD variations induced by the oceanic motion term.

The secular changes of the oceanic motion term are, as the inter-annual variations, determined by the ACC. In the MPI-OM the strength of the ACC decreases in a warming climate and thus the LOD decreases as well. However, this signal is small by about $0.4*10^{-6}$ s till the year 2060 accompanied by a decreasing ACC of around 4 Sv (Fig. 3.1.6).

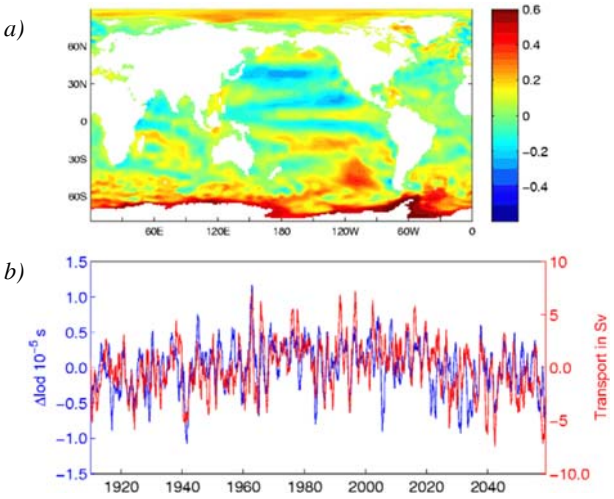

Fig. 3.1.5: (a) The correlation of the horizontal barotropic stream-function with LOD variations caused by the oceanic motion term. (b) Mass transport in the Drake Passage and LOD. Blue line shows the variation of LOD (detrended, 12-month running mean) caused by variations of the oceanic motion term. Red line depicts the variation in transport of the ACC (detrended, 12-month running mean) measured in the Drake Passage.

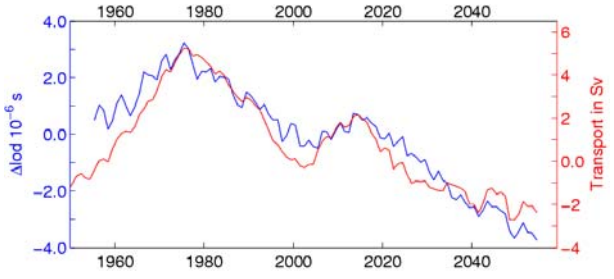

Fig. 3.1.6: Secular trend of LOD induced by the oceanic motion term. 12-year running mean of the LOD (blue line) and ACC transport through the Drake Passage (red line).

The matter term

The matter term depends on the moment of inertia I_{33} relative to the Earth's axis of rotation, defined through

$$I_{33} = R^2 \int_V \rho(\varphi, \lambda) \cos^2 \varphi \, dV \quad .$$

The variations of the matter term (or the moment of inertia) induced by the ocean, the atmosphere and the continental hydrology is determined through the meridional and vertical redistribution of mass. The induced change in LOD is written as

$$\Delta LOD = 86164\, s \frac{I_{33} - I_{33(t=0)}}{I_{33}^{E} + L_{33}} \quad .$$

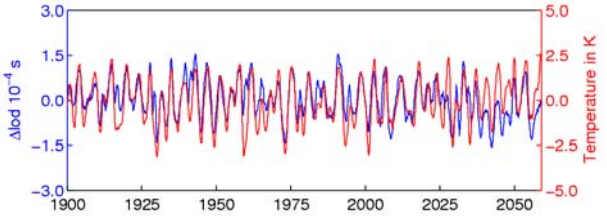

Fig. 3.1.7: Sea Surface Temperature (SST) in the Western Tropical Pacific and LOD. Blue line: The LOD variations induced by the oceanic matter term. Red line: Sea surface temperature anomalies in the Nino3.4 region.

The ocean induced inter-annual variations of LOD are shown in Fig. 3.1.7. Further the red line depicts the temperature anomaly in the Niño 3.4 Region. This region is in the western equatorial Pacific, bounded by 120°W – 170°W and 5°S – 5°N (TRENBERTH, 1997). El Niño events are accompanied by warming the central and eastern tropical Pacific Ocean, thus are indicated by positive temperature anomalies in Niño 3.4 Region. The El Niño episodes are often followed by La Niña events, indicated through negative temperature anomalies in the tropical Pacific Ocean. Obviously the temperature anomaly of the Nino3.4 region correlates well with the ocean induced LOD variation. El Niño events lead to positive LOD changes with values up to $1.5*10^{-04}$ s and La Niña events lead to negative LOD changes, vice versa.

The variation in the matter term can either result from redistribution of density in the ocean water column or through changes in sea level. The averaged sea level change in the equatorial Pacific region, extending from 9°S to 9°N and 150°W to 270°W, is shown in Fig. 3.1.8b. It is well correlated with the LOD and thus with the Niño 3.4 temperature anomalies, as well. Further, in Fig. 3.1.8a the correlation of sea level with the LOD is shown. The largest positive correlations are in the eastern tropical Pacific. This supports the hypothesis that the sea level variation, and not the density redistribution, is mainly responsible for inter-annual LOD variations.

To clarify the role of the sea level variation, the contribution of the sea level variation to the total moment of inertia is determined in the following. As Fig. 3.1.8b shows, the averaged amplitude in sea level is around 5 cm. The size of the region (9°S-9°N, 150°W-270°W) amounts to $2.6*10^{13}$ m². This corresponds to a water mass of around $1.4*10^{15}$kg, which in turn is equivalent to a variation of the moment of inertia of about 5.6 10^{28} kg m². This variation of moment of inertia results in a LOD variation of around 0.7 10^{-4}s, comparable with the LOD variations shown in Fig. 3.1.8b. This clearly suggests that the inter-annual LOD variations induced by the oceanic matter term are due to the sea level anomaly in the tropical Pacific interconnected with the ENSO variability.

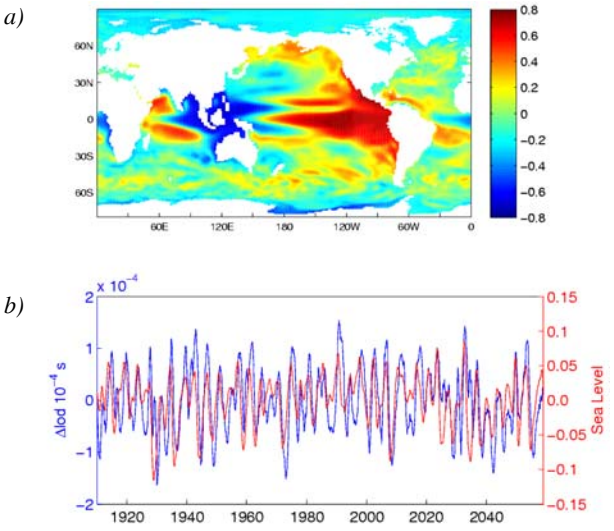

Fig. 3.1.8: (a) The correlation of the sea level with the LOD variations caused by the oceanic matter term. (b) Blue line shows the variation of LOD (detrended, 12-month running mean) caused by variations of the oceanic matter term. Red line depicts the variation in sea level (detrended, 12-month running mean) averaged over the equatorial Pacific region extending from 9°S-9°N and 150°W-270°W.

3.2 Dynamic model of Earth rotation, gravity and surface deformation DyMEG

In the framework of the three DFG-funded interdisciplinary bundle-projects DR143/10 (Earth rotation vector), DR143/12-1 and DR143/14-2 (Earth system model) the non-linear dynamic Earth system model DyMEG (Dynamic model for Earth rotation, gravity and surface geometry) has been developed at DGFI (SEITZ, 2004). In its present set-up DyMEG is a forward model which has been designed for theoretical studies of the Earth's reaction on gravitational and geophysical excitations.

It comprehends physical transfer functions which relate gravitational and geophysical model data and/or observations to time series of geodetic parameters of rotation, gravity field and surface geometry of the Earth. Since the parameters of these three so-called "pillars of geodesy" are resolved simultaneously within one consistent model, DyMEG corresponds with the goals of IAG's Global Geodetic Observing System (GGOS).

DyMEG is based on the balance of angular momentum in the Earth system. It is forced by various combinations of atmospheric, oceanic and hydrological data from reanalyses or GCMs, ocean circulation and hydrology models. Among the most important input parameters for DyMEG are fields of atmospheric surface pressure, ocean bottom pressure and continental water storage variations as well as time series of corresponding angular momentum variations in these subsystems. In addition, lunisolar gravitational torques and mass redistributions of the solid Earth and the oceans due to tides are considered.

DyMEG computes time series of EOP via numerical solution of the non-linear Liouville differential equation (SEITZ and KUTTERER, 2002), cf. Chapter 3.2.1. This approach is in contrast to most of the hitherto approaches in which the Liouville equation is solved analytically after some simplifications (e.g., MORITZ and MUELLER, 1987). Deformations of the solid Earth due to mass loads are computed in DyMEG from the pressure and mass load fields using either the common Green's functions approach (FARRELL, 1972) or a refined method based on site-dependent weighting functions (cf. Chapter 3.2.2). The mass redistributions due to these load deformations are subsequently converted into variations of the Earth's tensor of inertia and modelled in the Liouville equation (so-called indirect effect on Earth rotation). Variations of the second degree spherical harmonic coefficients of the Earth's gravity field are computed from the tensor of inertia as well. Corresponding time series of higher degree coefficients are deduced from the atmospheric and oceanic pressure fields and from the continental water storage change following the theory outlined by CHAO (1994). A viewgraph of the dynamic Earth system model is shown in Fig. 3.2.1.

It has been shown in several studies that the model results of DyMEG agree well with geodetic observations (details will be provided in Chapter 4). Simulated time series of EOP (pole-coordinates and length-of-day variations) are reproduced over a time span of more than two decades with a correlation of better than 0.95 (SEITZ, 2002; SEITZ, 2004; SEITZ et al., 2004; SEITZ, 2005a). Since the model numerically integrates the Liouville equation from given initial conditions (taken from the C04-series of the IERS) over an arbitrary time span, DyMEG can be used for the prediction of geodetic parameters. In addition, studies are possible which are related to the effect of global change when climate predictions are introduced as forcing (WINKELNKEMPER et al., 2008).

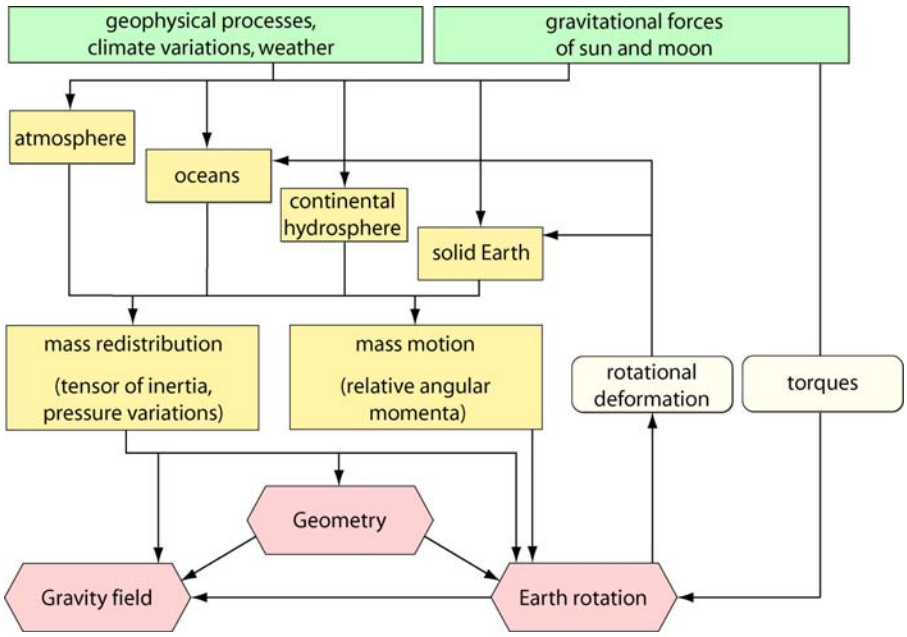

Fig. 3.2.1: Set-up of the dynamic Earth system model DyMEG.

3.2.1 Numerical solution of the Liouville differential equation

Studies of the temporal variation of Earth rotation are based on the solution of the well-known Liouville differential equation that describes the balance of angular momentum in the Earth system. With respect to the rotating terrestrial reference system the Liouville equation reads (MUNK and MACDONALD, 1960):

$$\frac{d}{dt}(\underline{I}\cdot\omega + h) + \omega \times (\underline{I}\cdot\omega + h) = L \qquad (1)$$

The reaction of the rotating and deformable Earth on internal mass redistributions and external gravitational torques follows from the solution of the Liouville equation for the vector ω which denotes the rotation vector of the terrestrial system with respect to an inertial reference system. In the equation $\underline{I}$ is the Earth's tensor of inertia and the vector h stands for angular momenta with respect to the terrestrial reference system (so-called relative angular momenta). The vector L on the right hand side of the Liouville equation denotes torques due to gravitational forces of Sun and Moon.

Mass redistributions in the Earth's subsystems, e.g., in the atmosphere and the oceans, cause perturbations of the tensor of inertia and relative angular momenta. Thus all quantities in the Liouville equation are time-dependent:

$$\underline{I} = \underline{I}(t),\ \ h = h(t),\ \ \omega = \omega(t),\ \ L = L(t)$$

Variations of Earth rotation are commonly modelled as small deviations from a uniform rotation. The z-axis of the applied terrestrial reference system is oriented approximately towards the Earth's maximum moment of inertia C; its equatorial axes x and y point towards the Greenwich meridian and 90° East, respectively. In this system, the coordinates of the rotation vector $\omega(t)$ are expressed by

$$\omega(t) \;=\; \Omega \cdot \begin{pmatrix} m_1(t) \\ m_2(t) \\ 1 + m_3(t) \end{pmatrix}, \qquad m_i \ll 1$$

where $\Omega = 2\,\rho$ / 86164 s means the approximate angular velocity of the terrestrial system. The dimensionless quantities m_i (I = 1, 2, 3) represent slight disturbances of the uniform rotation and are the unknown parameters in the Liouville differential equation (MUNK and MACDONALD, 1960). The two components m_1 and m_2 describe the time-variable orientation of the instantaneous rotation axis with respect to the z-axis of the inertial system (polar motion). Deviations of the Earth's angular velocity with respect to Ω are equivalent to changes of the length-of-day (ΔLOD). They follow from the temporal variation of the absolute value of the Earth rotation vector:

$$|\omega(t)| \;=\; \Omega\,\sqrt{m_1(t)^2 + m_2(t)^2 + (1+m_3(t))^2}$$
$$\approx\; \Omega(1+m_3(t))$$

The error for ΔLOD due to this approximation is 10^{-16} s and therefore negligible. The correspondence between the variation of the $|\omega(t)|$ and ΔLOD results from the definition of ΔLOD as the time span of one revolution of the Earth reduced by 86400 s:

$$\Delta LOD = \frac{2\pi\kappa}{|\omega(t)|} - 86400\,s$$

where

$$\kappa = \frac{\Omega}{2\pi} \cdot 86400\,s = \frac{86400}{86164}\,.$$

The introduction of the absolute value of $\omega(t)$ delivers

$$\Delta LOD = \frac{2\pi\kappa}{\Omega\,(1+m_3(t))} - 86400\,s$$

$$\approx -\,m_3(t) \cdot 86400\,s$$

The Earth's tensor of inertia $\underline{I}(t)$ comprehends the two components $\underline{I}_0$ and $\Delta\underline{I}(t)$ (LAMBECK, 1980), where $\underline{I}_0$ is an approximate tensor. If the axes of the reference frame would coincide with the principal axes of inertia, the approximate tensor would have the diagonal structure

$$\underline{I}_0 = \begin{pmatrix} A & 0 & 0 \\ 0 & B & 0 \\ 0 & 0 & C \end{pmatrix}$$

where A, B, C are the principal moments of inertia of the Earth (C > B > A). But since the axes of the principal moments of inertia differ from the axes of the applied terrestrial reference frame by approximately 15° in the equatorial plane, this divergence has to be taken into account by means of a rotation (MARCHENKO and SCHWINTZER, 2003; SEITZ, 2004). Consequently $\underline{I}_0$ does not have a diagonal structure with respect to the axes of the terrestrial reference frame.

The tensor $\Delta\underline{I}(t)$ describes the instantaneous deviation of the tensor of inertia from $\underline{I}_0$ due to mass redistributions in the Earth's subsystems (MORITZ and MUELLER, 1987). With the tensor elements (so-called deviation moments) $c_{ij}(t)$ << A,B,C, (i, j = 1, 2, 3), the symmetric tensor $\Delta\underline{I}(t)$ reads:

$$\Delta\underline{I}(t) = \begin{pmatrix} c_{11}(t) & c_{12}(t) & c_{13}(t) \\ & c_{22}(t) & c_{23}(t) \\ sym. & & c_{33}(t) \end{pmatrix}$$

The tensor of inertia $\Delta\underline{I}(t)$ and relative angular momenta $h(t)$ are computed from atmospheric and hydrospheric model simulations and/or observations. Deviation moments $c_{ij}(t)$ are computed from atmospheric and oceanic pressure fields as well as hydrological water mass variations. The elements of the vector $h(t)$ are calculated from wind fields and ocean currents. Torques $L(t)$ are computed in DyMEG on the basis of the lunisolar ephemerides DE405 (STANDISH, 1998) according to

$$L(t) = \sum_{j=s,m} \frac{3G\,M_j}{r_{ej}^5(t)} \begin{pmatrix} y_j(t) & z_j(t) & (C-B) \\ x_j(t) & z_j(t) & (A-C) \\ x_j(t) & y_j(t) & (B-A) \end{pmatrix}$$

(MORITZ and MUELLER, 1987) where the index j = s, m stands for Sun and Moon. The distance between the geocenter and the respective celestial body with the (point-) mass M_j is denoted with $r_{ej}(t)$; $x_j(t)$, $y_j(t)$, $z_j(t)$ are its coordinates with respect to the Earth-fixed reference frame and G is the gravitational constant. Details on the transformation procedure of the ephemerides from the space-fixed system (in which they are provided) into the Earth-fixed system are provided by SEITZ (2004). Additional influences on the tensor of inertia $\Delta\underline{I}(t)$ that are regarded in DyMEG are due to deformations of the Earth's body due to loading (section 3.2.2), solid Earth tides (MCCARTHY and PETIT, 2004), and rotational variations (see below). Time series for polar motion and ΔLOD follow from the solution of the Liouville equation for $\omega(t)$.

Forced polar motion due to the redistribution and motion of mass elements in the Earth system and external gravitational torques is superposed by free oscillations of the Earth. The most prominent of those is the Chandler oscillation which is caused by the misalignment of the Earth's rotation and figure axes. It is well known that the prolongation of the Euler period of 304 d (which is the period of the free oscillation of a rigid body with the Earth's dimensions) to the observed Chandler period σ_0 of about 432 d is due to rotational deformations of the Earth's body (MORITZ and MUELLER, 1987). Changes in the centrifugal potential which are caused by mass redistributions in the Earth system lead to back-coupling effects on the tensor of inertia (so-called rotational deformations). As a consequence the mass redistributions are accompanied by modified resonance conditions of the Earth. Therefore, both amplitude and frequency of the Chandler oscillation are time variable as they are directly influenced by the excitations. Since the effects of rotational deformations are regarded, DyMEG is able to react on rotational variations. This makes the model an ideal tool to study the interaction between forced and free polar motion and led to new conclusions on the excitation mechanism of the Chandler oscillation (SEITZ, 2005b; SEITZ et al., 2005; SEITZ and SCHMIDT, 2005). See Chapter 5.3 for more details.

In contrast to former investigations, the characteristics of the Chandler oscillation are not explicitly predetermined with respect to period and damping but reproduced by the model on the basis of geometric and rheological Earth parameters (SEITZ et al., 2004). The geometry of the Earth is specified by parameters of the GRS80 ellipsoid (MORITZ, 1980) and the principal moments of inertia A, B, and C are based on satellite gravity observations (MARCHENKO and SCHWINTZER, 2003). In DyMEG a simple Earth model is employed which consists of an anelastic mantle and a spherical liquid core which are assumed to be completely decoupled (SEITZ et al., 2004; SEITZ and SCHMIDT, 2005).

Therefore the numerical values of A, B, and C are transformed into A_m, B_m, and C_m which are attributed to the mantle alone (SASAO et al., 1980). The exchange of angular momentum between core and mantle influence polar motion mainly on sub-daily time scales. Since the main focus of the project is on seasonal to inter-annual time scales, decoupling of these system components is justified. (Note that this statement only holds for polar motion. In the case of ΔLOD huge decadal variations are caused by core-mantle interaction which can not be described by DyMEG in its present set-up; cf. SEITZ, 2004). As the core is assumed not to participate in the wobble, the period of the free polar motion is shortened from the Euler period of 305 d (which would be the period of a rigid Earth including the core) by approximately 50.5 days (SMITH and DAHLEN, 1981).

In DyMEG the Earth is regarded as a rotating deformable body. Temporal variations of the rotation vector $\omega(t)$ lead to variations of the centrifugal potential and thus yield deformations of the Earth's body and the oceans (WAHR, 1985). While the deformations that result from ΔLOD(t) are below one mm and are therefore negligible, deformations due to polar motion produce significant effects on the Earth's rotational dynamics as they lengthen the period of the free polar motion by approximately 173 days (SMITH and DAHLEN, 1981).

The back-coupling effects of rotational deformations on the geopotential are described by disturbances of the spherical harmonic coefficients $\Delta C_{21}(t)$ and $\Delta S_{21}(t)$ which are directly linked to the elements of $\Delta\underline{I}(t)$ via

$$\Delta C_{21}(t) = \frac{-c_{13}(t)}{a^2 M_E}$$

$$\Delta S_{21}(t) = \frac{-c_{23}(t)}{a^2 M_E}$$

(LAMBECK, 1980). The time series for $\Delta C_{21}(t)$ and $\Delta S_{21}(t)$ are calculated from the model results for $m_1(t)$ and $m_2(t)$ according to

$$\Delta C_{21}(t) = -\frac{\Omega^2 a^3}{3 G M_E} \left(\mathrm{Re}(k_2) \cdot m_1(t) + \mathrm{Im}(k_2) \cdot m_2(t) \right)$$

$$\Delta S_{21}(t) = -\frac{\Omega^2 a^3}{3 G M_E} \left(\mathrm{Re}(k_2) \cdot m_2(t) + \mathrm{Im}(k_2) \cdot m_1(t) \right)$$

(MCCARTHY and PETIT, 2004) and are subsequently transformed into perturbations of the tensor of inertia. The tensor elements $c_{13}(t)$ and $c_{23}(t)$ describe the mass redistributions caused by rotational deformations. They are superposed to variations of the tensor $\Delta\underline{I}(t)$ due to other effects and are thus used for the computation of polar motion at the next time step. For investigations of Earth rotation, contributions of higher degree spherical harmonic coefficients are negligible.

In the above equations, a denotes the Earth's mean equatorial radius, G is the gravitational constant, and M_E is the total mass of the Earth. The effects of rotational variations on the centrifugal potential of the deformable Earth are described by the complex pole tide Love number $k_2 = \mathrm{Re}(k_2) + i\,\mathrm{Im}(k_2)$ where Re and Im stand for the real and imaginary part, respectively. The pole tide Love number k_2 applied in DyMEG accounts for the effects of equilibrium ocean pole tides as well as for the anelastic response of the Earth's mantle (SMITH and DAHLEN, 1981; SEITZ et al., 2004). The latter leads to an extension of the period of the free wobble by another 8.5 days (WILSON and HAUBRICH, 1976) and is accompanied by energy dissipation which causes an attenuation of the free polar motion. This means, the free oscillation of the gyro is a damped oscillation which would diminish (i.e. the rotation axis would be shifted to the figure axis) if no excitation mechanism would counteract the dissipation (cf. section 4). In DyMEG this damping effect is considered by a complex surcharge to the numerical value of k_2 (MCCARTHY and PETIT, 2004). Within a sensitivity analysis of the dynamic model (SEITZ and KUTTERER, 2005) the dependence of the numerical solution was assessed with respect to parameters which are entered into the model. In particular, the influence of the value of k_2 was discussed, as it is directly linked to period and damping of the free rotation of DyMEG. For $k_2 = 0.3520 + 0.0042i$ the resulting polar motion series showed optimum agreement with geodetic observations. This value was determined empirically from multiple model runs applying two independent atmosphere-ocean combinations (SEITZ et al., 2004; SEITZ 2004). It corresponds to a Chandler period of 434 days and a quality factor of Q = 69 which is in line with the results of other recent investigations.

For the numerical solution the Liouville differential equation (1) is written less compact as

$$\dot{\underline{I}}\,\underline{\omega} + \underline{I}\,\dot{\underline{\omega}} + \dot{h} + \omega \times \underline{I}\,\underline{\omega} + \omega \times h = L \qquad (2)$$

As above, all terms in this equation are time-variable. The individual terms of this equation read explicitly:

$$\dot{\underline{I}}\,\underline{\omega} = \begin{pmatrix} \dot{c}_{11} & \dot{c}_{12} & \dot{c}_{13} \\ \dot{c}_{12} & \dot{c}_{22} & \dot{c}_{23} \\ \dot{c}_{13} & \dot{c}_{23} & \dot{c}_{33} \end{pmatrix} \cdot \Omega \begin{pmatrix} m_1 \\ m_2 \\ 1 + m_3 \end{pmatrix} \qquad (3)$$

$$\dot{\underline{I}}\,\underline{\omega} = \begin{pmatrix} A + c_{11} & c_{12} & c_{13} \\ c_{12} & B + c_{22} & c_{23} \\ c_{13} & c_{23} & C + c_{33} \end{pmatrix} \cdot \Omega \begin{pmatrix} \dot{m}_1 \\ \dot{m}_2 \\ \dot{m}_3 \end{pmatrix} \qquad (4)$$

$$\dot{h} = \begin{pmatrix} \dot{h}_1 \\ \dot{h}_2 \\ \dot{h}_3 \end{pmatrix}$$

$$\omega \times \underline{I}\,\omega = \Omega \begin{pmatrix} m_1 \\ m_2 \\ 1+m_3 \end{pmatrix} \times \begin{pmatrix} A+c_{11} & c_{12} & c_{13} \\ c_{12} & B+c_{22} & c_{23} \\ c_{13} & c_{23} & C+c_{33} \end{pmatrix} \cdot \Omega \begin{pmatrix} \dot{m}_1 \\ \dot{m}_2 \\ 1+\dot{m}_3 \end{pmatrix}$$

$$\omega \times h = \Omega \begin{pmatrix} m_1 \\ m_2 \\ 1+m_3 \end{pmatrix} \times \begin{pmatrix} h_1 \\ h_2 \\ h_3 \end{pmatrix}$$

In order to solve the Liouville equation numerically, time derivatives of $m_i(t)$ shall be assembled on the left hand side of equation (2). Since rotational deformations are regarded, the tensor of inertia includes deviations, which are dependent on $m_1(t)$ and $m_2(t)$. Consequently derivatives of $m_i(t)$ appear in both terms (3) and (4). Therefore, the derivative of the tensor of inertia is divided into two parts: One component (index R) describes the effect of rotational deformations and depends on the derivatives of $m_i(t)$. The second component (index G) comprehends the geophysically induced mass redistributions in the atmosphere, the ocean and the solid Earth due to loading and tidal deformations. This second component is independent of the derivatives of $m_i(t)$. The first component is placed on the left hand side, the second component on the right hand side of the Liouville equation:

$$\dot{\underline{I}}_R\,\omega + \underline{I}\,\dot{\omega} = L - \dot{\underline{I}}_G\,\omega - \dot{h} - \omega \times h - \omega \times \underline{I}\,\omega \qquad (5)$$

If the products of the $m_i(t)$ with their (very small) derivatives are neglected, the first term of equation (5) turns into

$$\dot{\underline{I}}_R\,\omega = \frac{\Omega^3 a^5}{3G} \begin{pmatrix} \mathrm{Re}(k_2) \cdot \dot{m}_1 + \mathrm{Im}(k_2) \cdot \dot{m}_2 \\ \mathrm{Re}(k_2) \cdot \dot{m}_2 + \mathrm{Im}(k_2) \cdot \dot{m}_1 \\ 0 \end{pmatrix}$$

$$\approx \frac{\Omega^3 a^5}{3G} \mathrm{Re}(k_2) \begin{pmatrix} \dot{m}_1 \\ \dot{m}_2 \\ 0 \end{pmatrix}$$

The imaginary part of k_2 is two orders of magnitude smaller than the real part. Consequently its products with the derivatives of $m_i(t)$ can also be neglected, and the left hand side of system (5) is written as

$$\dot{\underline{I}}_R\,\omega + \underline{I}\,\dot{\omega} = \left[\frac{\Omega^3 a^5}{3G} \mathrm{Re}(k_2) \begin{pmatrix} 1 & 0 & 0 \\ 0 & 1 & 0 \\ 0 & 0 & 0 \end{pmatrix} + \Omega\,\underline{I} \right] \begin{pmatrix} \dot{m}_1 \\ \dot{m}_2 \\ \dot{m}_3 \end{pmatrix}$$

$$=: \underline{F} \begin{pmatrix} \dot{m}_1 \\ \dot{m}_2 \\ \dot{m}_3 \end{pmatrix}$$

For the Liouville equation follows

$$\begin{pmatrix} \dot{m}_1 \\ \dot{m}_2 \\ \dot{m}_3 \end{pmatrix} = \underline{F}^{-1} \left(L - \dot{\underline{I}}_G\,\omega - \dot{h} - \omega \times h - \omega \times \underline{I}\,\omega \right) \qquad (6)$$

This coupled system of three first order differential equations is solved as an initial value problem in DyMEG. Initial values for $m_i(t = t_0)$ are deduced from the geodetically observed time series for polar motion and length-of-day variations which are published in the C04 series by the IERS (DICK and RICHTER, 2008). The relation between the geodetic observations and the values $m_i(t)$ has been described in detail by GROSS (1992). In contrast to the traditional analytical approach, polar motion and ΔLOD are computed simultaneously in DyMEG.

The sensitivity of the numerical solution with respect to the choice of the initial values was tested by varying the values within the interval +/- $3\sigma_i$ with respect to the observations of polar motion and ΔLOD which have the standard deviations σ_i (SEITZ, 2004; SEITZ and KUTTERER, 2005). As the initial amplitude of the Chandler wobble and its phase are directly linked to $m_1(t = t_0)$ and $m_2(t = t_0)$, DyMEG was expected to be rather sensitive to variations of the initial values. However, the sensitivity analysis revealed that the interpretation of the numerical results is not limited by the choice of the initial values as long as the values stay within these reasonable intervals (see section 4.2). Deviations between different time series were maximum at the beginning of the simulations (due to the starting situation), but convergence increased with time and DyMEG reached a steady state after few years (see section 4). For the numerical evaluation of equation (6), a one-step-solver based on the $4^{th}/5^{th}$ order Runge-Kutta-Fehlberg method is applied (PRESS et al., 1987). It was shown that the results for polar motion and ΔLOD are reliable from the algorithmic point of view (SEITZ and KUTTERER, 2002).

3.2.2 Inverse model approach for surface deformations of the solid Earth due to mass loads

Mass redistributions in various components of the Earth system, e.g. in the atmosphere and the hydrosphere, exert time-variable surface loads on the solid Earth. This way they cause deformations of the Earth's body which are up to several centimetres in the vertical and several millimetres in the horizontal (SUN et al., 1995). The change of the surface geometry entails the redistribution of mass elements within the solid Earth which significantly influences the Earth's gravity field and its rotational dynamics. Therefore the effect of load deformations is also regarded in DyMEG. The computation is a two step procedure in the model: First, the vertical surface deformations are computed using the procedure developed by SEITZ and KRÜGEL (2008); the method is described briefly below. In the second step the vertical deformations are transformed into variations of the Earth's tensor of inertia $\Delta\underline{I}(t)$ (see SEITZ, 2004, for details). The tensor variations due to the mass redistributions within the solid Earth as a consequence of loading are called the indirect effect, whereas the variations of $\Delta\underline{I}(t)$ due to the evocative mass redistributions within the atmosphere and the oceans are called the direct effect.

Usually the effect of loading on crustal deformation is computed by means of a weighting function (Green's function) which is based on site-independent load Love numbers (FARRELL, 1972; MORITZ and MUELLER 1987). But since the Earth's crust is composed of heterogeneous material with different density, thickness and structure, the application of a site-independent approach appears not to be appropriate. In the framework of this project an alternative method has been developed for the computation of vertical crustal deformations in which the Green's function is substituted by a site-dependent exponential function (SEITZ and KRÜGEL, 2008). In this inverse model approach the unknown parameters of the exponential function are estimated by least-squares adjustment using time series of globally distributed GPS sites as observations.

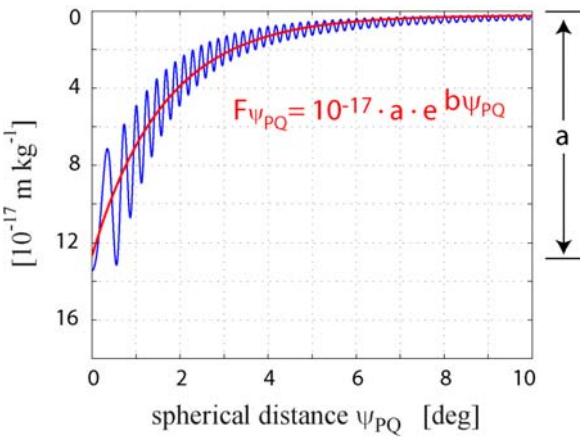

Fig. 3.2.2: Green's function for continental crust based on PREM up to degree 2000 (thin line) and exponential function for the parameters a = -12.5 and b = -35 (thick line).

In general the surface deformation due to loading is computed using a function $F(\psi_{PQ})$ which works as a weighting operator. The function relates an individual (point) load $q(\lambda,\varphi)$ (units [kg/m^2]) at position $Q(\lambda,\varphi)$ on the Earth's surface to the associated deformation at position $P(\lambda,\varphi)$; the spherical distance between P and Q is denoted by ψ_{PQ}. The blue curve in Fig. 3.2.2 shows the usually applied weighting function (Green's function) for continental crust as computed from load Love numbers up to the spherical harmonic degree n = 2000. The load Love numbers applied here are based on the Preliminary Reference Earth Model (PREM) (DZIEWONSKI and ANDERSON, 1991; SCHERNECK, 1990). The strong variability of the curve reflects the truncation error.

Since the load Love numbers are global mean values, this weighting function is not capable of regarding local crustal inhomogeneities in the model. Therefore a site-dependent weighting function is proposed in which the common Green's function is substituted by a simple exponential function of the general form

$$F(\psi_{PQ}) := 10^{-17}\, a\, e^{-b\psi_{PQ}}$$

The parameter a (unit [m/kg]) means the vertical deformation of a cell on the Earth's surface if loaded by a certain mass. The parameter b determines the decay of the curve, i.e., the effect of a load on neighbouring cells as a function of their spherical distance. Approximate values for which the function $F(\psi_{PQ})$ fits best to the displayed Green's function are a = -12.5 and b = -35 (Fig. 3.2.2, red line). A choice of different numerical values for the parameters a and b allows to account for regional discrepancies of crustal densities. Parameter a shall be related to the density of the actually loaded grid cell whereas parameter b is associated with the (mean) density of surrounding cells. Consequently the two parameters are considered to be independent. The principle of the approach is displayed in Fig. 3.2.3.

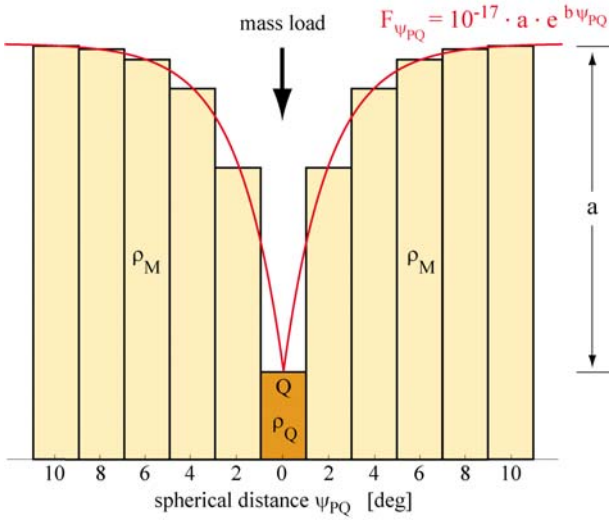

Fig. 3.2.3: Principle of the site-dependent approach: Parameter a is related to the density ρ_Q of the loaded grid cell, parameter b is related to the mean density ρ_M of the surrounding cells.

The numerical values of the parameters a and b are estimated for cells of 2° x 2° using geodetic observations of vertical site displacements from globally distributed GPS permanent stations. On the basis of the crustal model Crust2.0 (BASSIN et al., 2000) clusters of grid cells are predefined for which identical parameters a and b shall be determined. The model Crust2.0 provides global information on crustal material, thickness and density for 2° x 2° blocks.

The numerical values of the parameters are estimated by least-squares adjustment. The observation equation reads

$$d_r(P) = \sum_{\substack{k=1 \\ \psi_{PQ_k} < 10^\circ}}^{N} 10^{-17}\, q_{Q_k}\, A_{Q_k} \left(a_{ik}\, e^{b_{ik}\, \psi_{PQ_k}} \right)$$

where A_{Qk} is the area of the loaded grid cell k. Observations of vertical site displacements on the left hand side of the equation are taken from weekly solutions of the global GPS station network of the International GNSS Service (IGS). These station position time series are based on homogeneously combined data sets as they were prepared for the ITRF2005 computation. They are available since 1996. Up to now the IGS processing strategy does not account for non-tidal loading effects. Consequently the time series contain the variations due to atmospheric, hydrological and non-tidal oceanic mass loads. In order to ensure that the interpretability of the station position time series is not limited by slight discrepancies with respect to the geodetic datum of individual IGS solutions, the weekly solutions are transformed to a combined multi-year solution applying a seven parameter similarity-transformation (MEISEL et al., 2005). The resulting station position time series are subsequently reduced by mean and trend (which is performed separately for individual sections if there are discontinuities in the time series).

Mass load fields $q(\lambda,\varphi)$ are computed from modelled or observed atmospheric surface pressure and oceanic bottom pressure variations $p(\lambda,\varphi)$ [Pa]. These pressure variations are converted into mass loads according to the equation $q(\lambda,\varphi) = p(\lambda,\varphi)/g$ where g is the gravitational acceleration. Variations of continental hydrology are also taken into account. Respective data are derived from models for global water and groundwater storage [mm] as well as snow loads. Numerical results of modelled vertical surface deformations are provided in Chapter 4.

Is has been shown that the adjusted parameters a and b agree quite well with the above mentioned approximate values a = -12.5 and b = -35, and in principle the results match the expectations: For cells with low densities the deformation is stronger (i.e. values for a are larger) and the function is steeper (i.e. values for b are larger) than for cells with higher densities (SEITZ and KRÜGEL, 2008). Compared to the Green's function approach significant improvement is achieved for some regions, and in general the proposed approach is more effective in explaining the observations: For none of the stations the agreement between observations and model results deteriorates when the site-dependent weighting functions are applied instead of the Green's function. Explicit improvement is achieved in regions which are covered well with GPS sits and where high annual vertical displacements are observed, e.g., in Siberia, the Arctic regions of North America and the Gulf region. However in regions like Africa and Antarctica parameter estimation is difficult due to the sparse distribution of GPS sites. Here either no parameters a and b can be estimated at all for some grid cells, or the estimates are not significant because stations are too far away from the respective cells or contain errors which are sometimes larger than the signal itself. Consequently surface deformations were computed using the traditional approach in these areas. Even though there remains some challenge, and further refinement of the model is necessary, it has been demonstrated, that a site-dependent approach for the computation of load deformations is in principle superior.

4. Results for Earth rotation, surface deformation and gravity

Variations of the Earth's rotation, gravity field and surface geometry are computed with the Earth system model DyMEG. The model is forced by fields of atmospheric surface pressure, ocean bottom pressure, continental water storage variations, and corresponding time series of atmospheric and hydrospheric variations of the Earth's tensor of inertia and relative angular momenta.

4.1 Validation of DyMEG with NCEP and ECCO

In a first step reliability and potential of the Earth system model DyMEG shall be assessed. Since ECOCTH is an integrated (i.e. mutually coupled) model of atmosphere and hydrosphere in which no data assimilation is applied, the approximation of real nature is expected to be somewhat inferior than in the case of models that treat the subsystems separately (SÜNDERMANN and HENSE, 2009). Many of such individual models use data assimilation, and the influences of other subsystems are prescribed by boundary values that are based on observations. Consequently mass redistributions and motions from respective data sets are better related to real time than in the case of ECOCTH. The use of constrained models therefore allows a comparison of the results of DyMEG with the geodetic observations in the time-domain. On the other hand, the forcing of DyMEG with the output of ECOCTH ensures maximum consistency among the involved models and allows for future projections of atmospheric and hydrospheric influences on geodetic parameters. However the evaluation of the results is restricted to the spectral domain and statistical interpretation. Therefore the conceptual differences among the forcing conditions of DyMEG should be kept in mind when numerical model results are analysed.

The quality of DyMEG shall be validated by a direct comparison of the model results with geodetically observed time series for polar motion, ΔLOD, second degree spherical harmonic coefficients and variations of the Earth's surface geometry in the time domain. Therefore the model is forced by atmospheric reanalyses from NCEP/NCAR (National Centers for Environmental Prediction/National Centers for Atmospheric Research) (KALNAY et al., 1996) and the global ocean circulation model ECCO (STAMMER et al., 2002). Two different versions of ECCO, namely the unconstrained version c20010701 and the version kf049f that assimilates observations have been applied in this study. In both cases the ocean dynamics described by ECCO is computed from NCEP forcing fields comprising wind stress, heat and freshwater fluxes. The ocean's response to atmospheric pressure variations is assumed to be exactly inverse barometric. Simulations with DyMEG are performed for the epoch between 1.1.1980 and 1.3.2002.

The results of DyMEG under NCEP+ECCO forcing are described in the following publications: For polar motion and ΔLOD see SEITZ (2004, 2005a, b), SEITZ and SCHMIDT (2005); for the 2nd degree spherical harmonic coefficients of the Earth's gravity field see SEITZ (2004); for the surface deformations of the solid Earth due to loading see SEITZ and KRÜGEL (2008). For details concerning the computations we refer to the mentioned publications. Here we want to restrict ourselves to the numerical results.

Fig. 4.1.1 shows the DyMEG result for polar motion and the corresponding geodetic observation published in the well-known C04-series of the International Earth Rotation and Reference Systems Service (DICK and RICHTER, 2008). For both the x- and the y-component model result and observation agree very well, and the beat of 6.5 years which is due to the superposition of annual and Chandler oscillation is reproduced by the model. Correlation coefficients amount to 0.99, the RMS of the difference between model result and C04 series are 29.5 mas (x-component) and 23.3 mas (y-component).

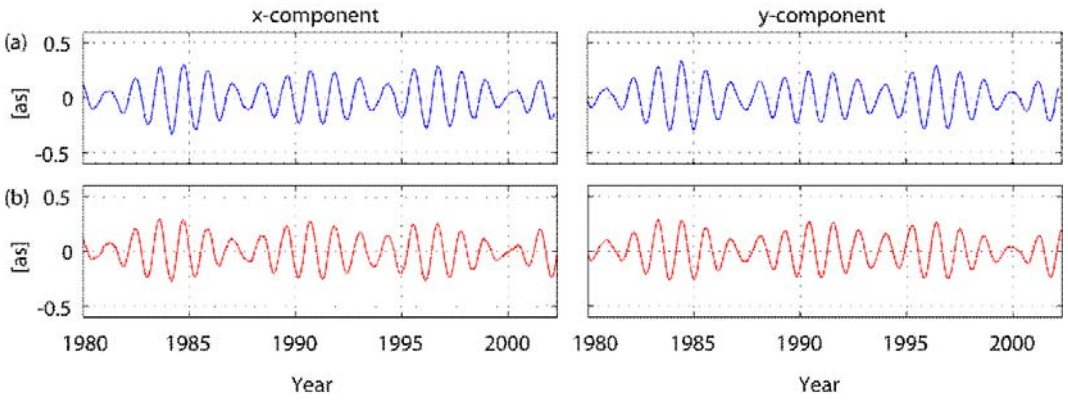

Fig. 4.1.1: Model result for polar motion from DyMEG under NCEP + ECCO forcing (a) and geodetic observations from the C04 series (b); taken from Seitz (2004).

The results of a wavelet analysis using the Morlet wavelet are shown in Fig. 4.1.2. For details on the analysis method, see SCHMIDT (2000, 2001). While the retrograde part of the annual signal appears nearly unchanged in the scalogram of the difference between model result and C04 series, the prograde scalogram of the difference features almost no signal. Slight discrepancies in the prograde spectrum can be seen in the range of the annual component. The observed Chandler oscillation (prograde, 434 days) is reproduced by DyMEG very well.

Fig. 4.1.3 displays the comparison between modelled and observed variations of LOD. A moving average over 5 years has been removed from the observations, since decadal scale variations due to core-mantle interaction are present in the C04-ΔLOD series. Since core and mantle are assumed to be decoupled in DyMEG (which is a valid assumption on time scales between weeks and few years) this long-term change of LOD cannot be reproduced by DyMEG. Significant variations of LOD are also caused by tidal effects. The right panel of Fig. 4.1.3 shows the time series after tidal effects have been removed. Like for polar motion very good agreement between modelled and observed ΔLOD is obvious. The correlation coefficient amounts to 0.98, the RMS of the difference between model time series and C04 is 120 ms.

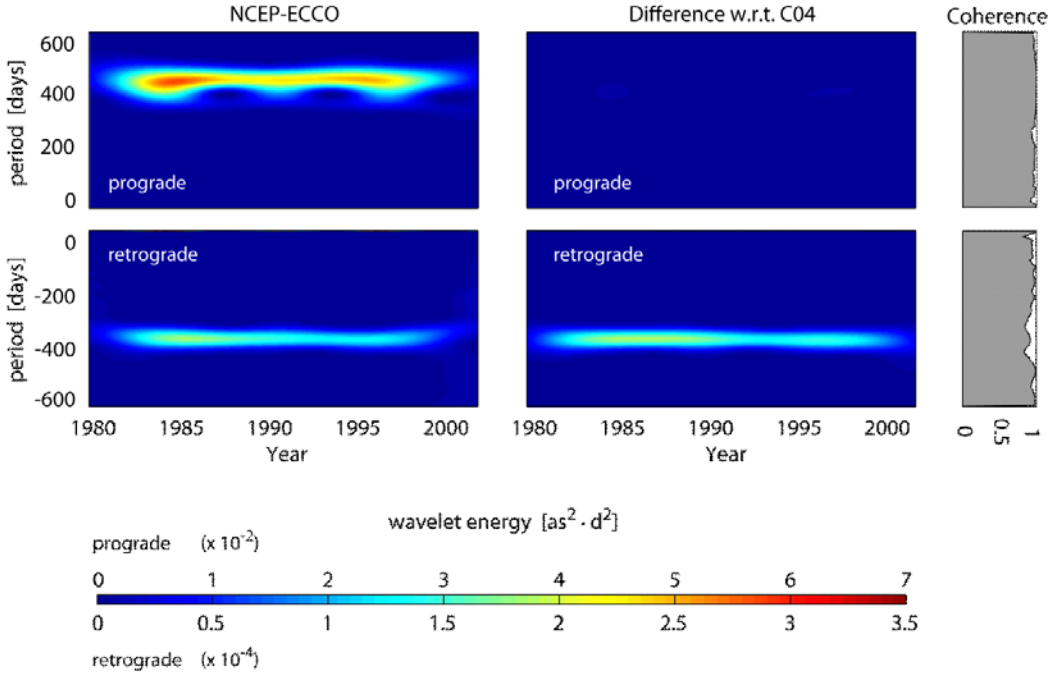

Fig. 4.1.2: Wavelet scalograms of the model result for polar motion from DyMEG under NCEP + ECCO forcing (left) and of the difference between model result and geodetic observation (right). Note the different scaling of the colour-bar for prograde and retrograde scalograms.

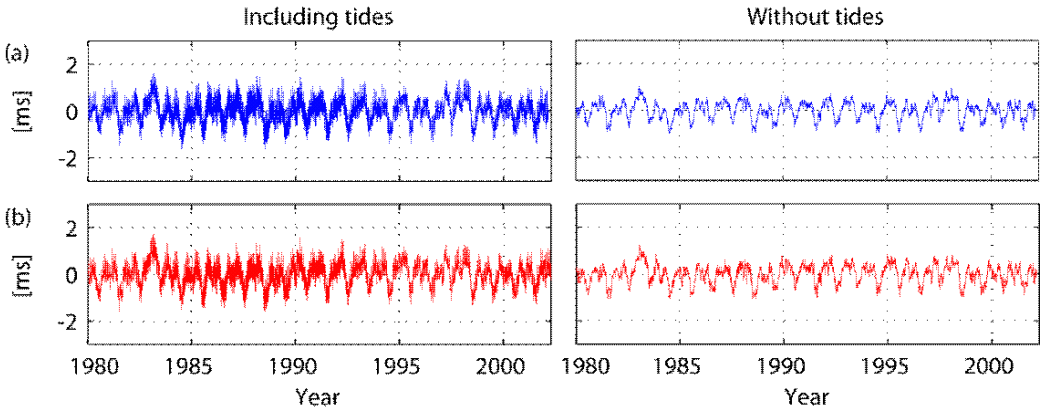

Fig. 4.1.3: Left panels: Model result for ΔLOD from DyMEG under NCEP + ECCO forcing (a) and geodetic observations from the C04 series reduced by a moving average over 5 years (b). Right panels: The same after reduction of tidal effects.

Signal decomposition by means of Morlet wavelet analysis results in the scalograms shown in Fig. 4.1.4. The strongest signals are visible in the annual and semi-annual band of the model result, which match the observations perfectly. During 1983 and 1998 the signal energy in the range between 44 and 53 months increases. This effect is related to ENSO episodes (cf. section 4.2). Increased signal amplitudes can also be seen in the time series (Fig. 4.1.3) during those years.

For lack of space the discussion of model results for low degree coefficients of the Earth's gravity field shall be restricted to one example. Fig. 4.1.5 shows the model time series of the coefficient ΔC_{20} which is related to the variation of the Earth's oblateness. For comparison a geodetic time series of ΔC_{20} in monthly resolution is displayed which has been derived from Satellite Laser Ranging (SLR) analysis (COX and CHAO, 2002). During the first years of SLR the accuracy of the observations amounts to $1.5 \cdot 10^{-10}$. Towards the end of the time series this value improves to $0.3 \cdot 10^{-10}$.

As in the case of ΔLOD a large fraction of the variation of ΔC_{20} is caused by solid Earth tides on sub-monthly to monthly time scales. The tidal effects on the low degree gravity field coefficients are about one order of magnitude larger than the variations caused by atmosphere and hydrosphere. When the model result is monthly averaged, the comparison with SLR yields a correlation of 0.85. The RMS of the difference between both series is 0.55 •10-[10].

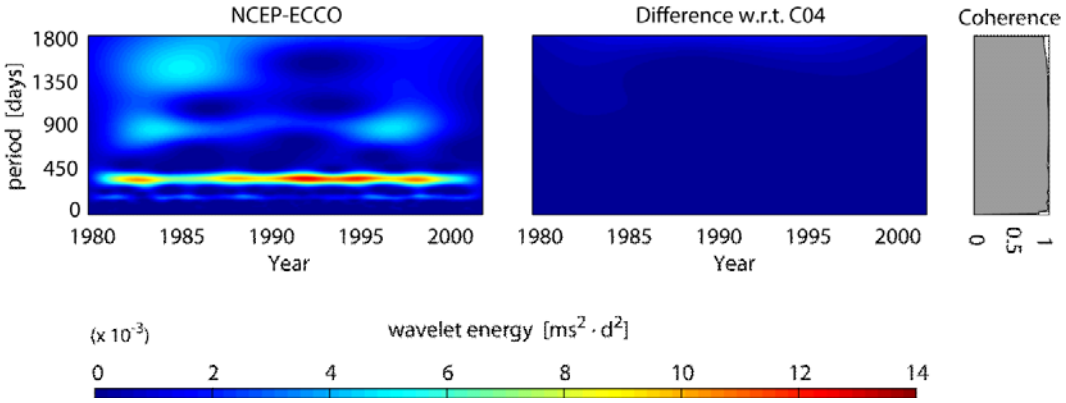

Fig. 4.1.4: Wavelet scalograms of the model result for ΔLOD from DyMEG under NCEP + ECCO forcing (left) and of the difference between model result and geodetic observation (right).

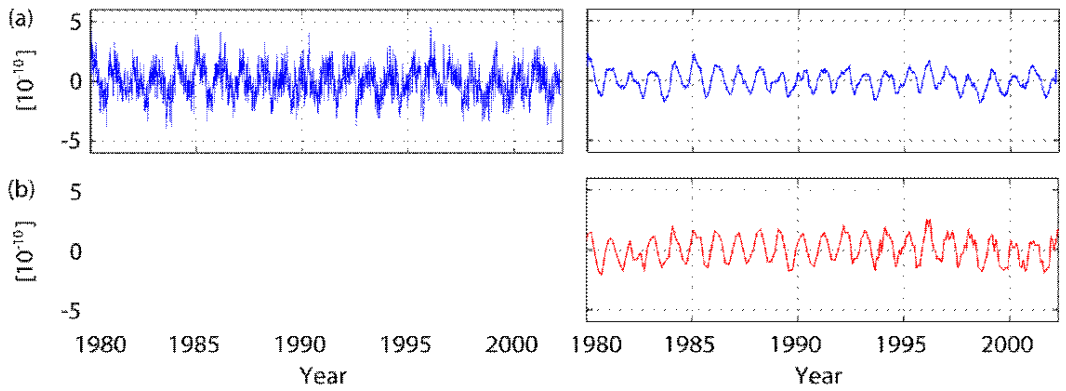

Fig. 4.1.5: Model result for ΔC_{20} in fully normalised representation from DyMEG under NCEP + ECCO forcing (a) (left: Daily values; right: Monthly mean values) and geodetic observations from SLR analysis (b) (monthly values).

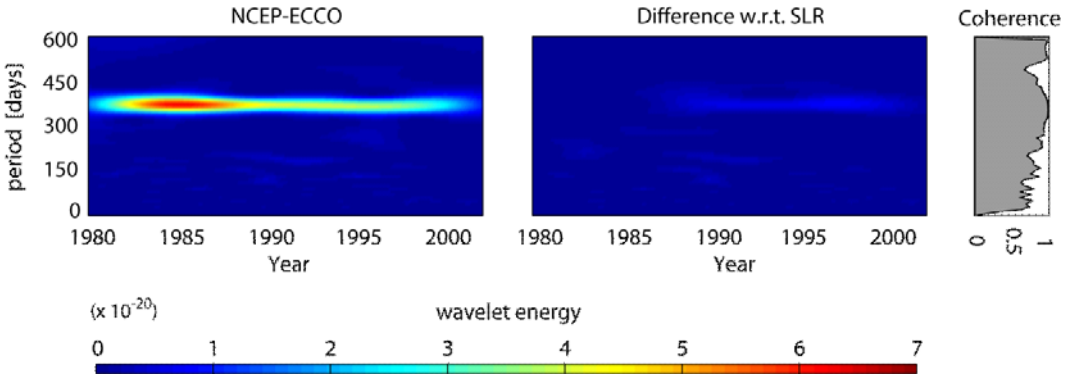

Fig. 4.1.6: Wavelet scalograms of the model result for ΔC_{20} from DyMEG under NCEP + ECCO forcing (left) and of the difference between model result and geodetic observation (right).

The wavelet scalogram of the model result (Fig. 4.1.6, left) shows a pronounced annual signal which agrees well with the observations during the first decade of the simulation period. But after 1990 the annual signal induced by NCEP+ ECCO decreases steadily, while the amplitude is almost constant in the observations. Therefore the scalogram of the difference shows an increasing signal in the annual band after 1990. In the spectral range below 300 days the SLR series features only little energy, even though its temporal resolution is 30 days. Consequently the scalograms of model result and its difference w.r.t. the observations are similar in this part of the spectrum.

Model results for surface deformations due to loading effects are computed in DyMEG using the site-dependent inverse model approach described in section 3.2.2. Besides atmospheric surface loads from NCEP and oceanic bottom pressure variations from ECCO we considered continental water mass variations from the Land Dynamics Model (LaD, version Euphrates) (MILLY and SHMAKIN, 2002) in the computations (SEITZ and KRÜGEL, 2009). LaD provides monthly values of global water and groundwater storage as well as snow loads on a 1°x1° grid. Fig. 4.1.7 displays the results from DyMEG for load deformations at three locations of GPS-sites of the International GNSS Service (IGS). In addition model time series for the deformations are shown that follow from the traditional Green's function approach (FARRELL, 1972) applying identical forcing.

Correlation coefficients between the results of the site-dependent approach and the GPS time series are also provided. The respective correlations between the Green's function approach and the observations are almost identical since the overall patterns of the model curves (e.g. spikes) are largely imposed by the applied geophysical forcing. The curves differ mainly with respect to their amplitudes for which the correlation coefficient is less sensitive.

Analyses of the RMS differences reveal that in general the proposed approach is more effective in explaining the observations: For none of the stations in our study the agreement between observations and model results deteriorates when the site-dependent weighting functions are applied instead of the Green's function. The largest discrepancies between both methods (RMS differences up to 2 mm) are apparent in regions where high annual vertical displacements are observed, e.g., in Siberia, the arctic regions of North America, and the Gulf region. But on the other hand there are regions where the improvement is marginal, e.g., Europe and SE-Asia.

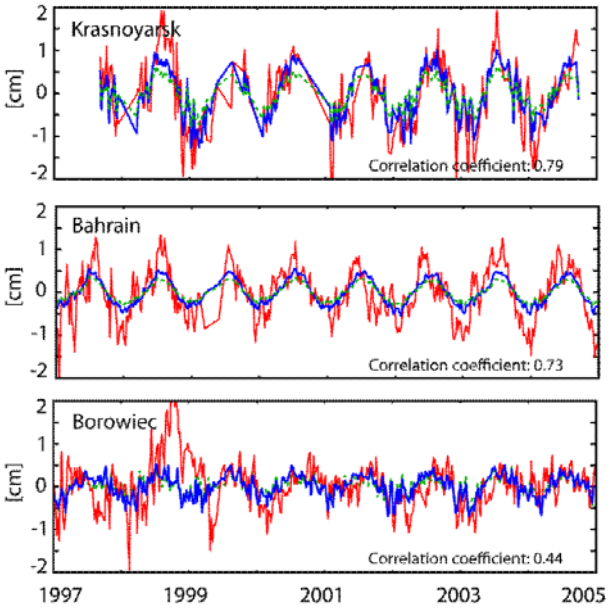

Fig. 4.1.7: Model results for load deformations from DyMEG under NCEP + ECCO forcing for three IGS sites on different continents (solid blue: site dependent approach; dotted green: usual Green's functions approach) and geodetic observations from GPS (red).

Since the applied inverse model approach is based on GPS observations, the adverse distribution of GPS sites is one of the crucial points for its global applicability. While the Green's function approach can be applied everywhere since it is based on site-independent Love numbers, the site-dependent approach relies on dense and high quality GPS observations. In other words the approach has a high potential for the geophysical interpretation of GPS time series (higher than the site-independent approach), but it

is not so reliable, if deformations shall be computed in areas which lack GPS observations. There are large regions for which either no parameters of the site-dependent weighting functions can be estimated (e.g., Africa, where hardly any GPS stations are located) or where the estimates are not significant because stations are far away from the respective cells or contain errors which are sometimes larger than the signal itself (e.g., the erroneous pattern in the time series of Borowiec around 1999, see Fig. 4.1.7.). Consequences and suggestions for improvements are discussed by SEITZ and KRÜGEL (2009).

4.2 Results of DyMEG with ECOCTH forcing

The described model runs using NCEP + ECCO forcing have shown DyMEG's potential for modelling parameters related to Earth rotation, gravity field and surface geometry. The results turned out to be realistic and agree very well with geodetic observations when DyMEG is forced with atmospheric reanalysis data and an assimilating ocean model.

Now the results of the integrated atmosphere-hydrosphere model ECOCTH shall be introduced into DyMEG. Discussion of the results will be restricted to Earth rotation parameters and second degree gravity field coefficients. Time series of load deformations and their indirect effect on Earth rotation have been computed from the ECOCTH pressure fields using the site-dependent weighting functions that have been determined in the course of the run forced by NCEP + ECCO + LaD as described above. This is inevitable due to the following reason:

The deformation module of DyMEG is based on a two-step procedure: First the parameters of the site-dependent weighting functions are estimated for cells of 2°x2° (see section 3.2.2), where both the GPS observations and the model pressure fields are used as input. In the second step the determined weighting functions are applied in order to compute load deformations from the pressure fields. In order to obtain reasonable results, phase and amplitude relations between observed vertical site displacements and modelled pressure variations must match. Therefore no meaningful results for the estimated parameters of the weighting functions can be expected, when DyMEG is forced with the free model ECOCTH. So we used the weighting functions determined in the NCEP + ECCO + LaD forced run, and applied those in the second step, i.e. for the computation of deformations from the ECOCTH pressure fields.

The resulting load deformations are transformed into variations of the Earth's tensor of inertia (indirect effect; cf. section 3.2) and introduced into DyMEG together with the (direct) atmospheric and hydrospheric tensor variations, relative angular momenta and pressure variations from ECOCTH.

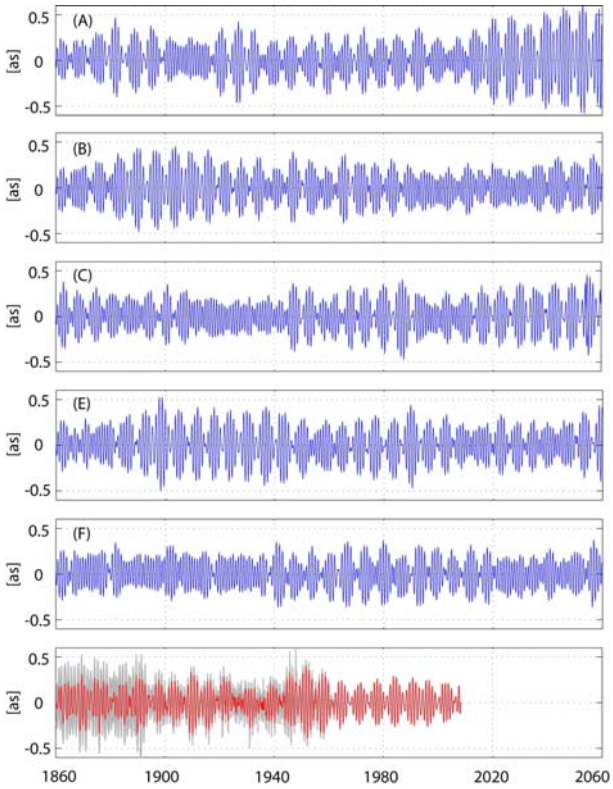

Fig. 4.2.1: Model results for polar motion from DyMEG under ECOCTH forcing (x-components of five scenario runs) and geodetic observations from the C01 series. The grey curve shows the 3σ error margin of the observations.

Initial values for the numerical integration are taken from the long-term C01 series of the IERS. In this time series the IERS provides observations of polar motion since 1846 in a temporal resolution of 0.1 years (1846-1889) and 0.05 years (1890 until mid 2008). During the first decades the astrometrical observations of polar motion are very inaccurate (standard deviations up to $\sigma = 0.16$ as). Today modern space geodetic techniques allow for observations at an accuracy level of a few mas. The time series C01 is shown together with the 3σ error margin in the lowest panel of Fig. 4.2.1.

In order to save computing time, the runs presented below were performed without considering solid Earth tides in DyMEG. The top panels of Fig. 4.2.1 show the model results for polar motion (x-components) for the five scenario runs (A, B, C, E, F) of ECOCTH.

Corresponding wavelet scalograms of the curves in Fig. 4.2.1 are provided in Fig. 4.2.2. There are significant differences between the runs that reflect the internal variability of the five ensemble members of ECOCTH. In all cases a clear beat between the two prominent signals, the annual and the Chandler oscillation, is obvious. In general the signal amplitudes appear to be reasonable in comparison with the observations.

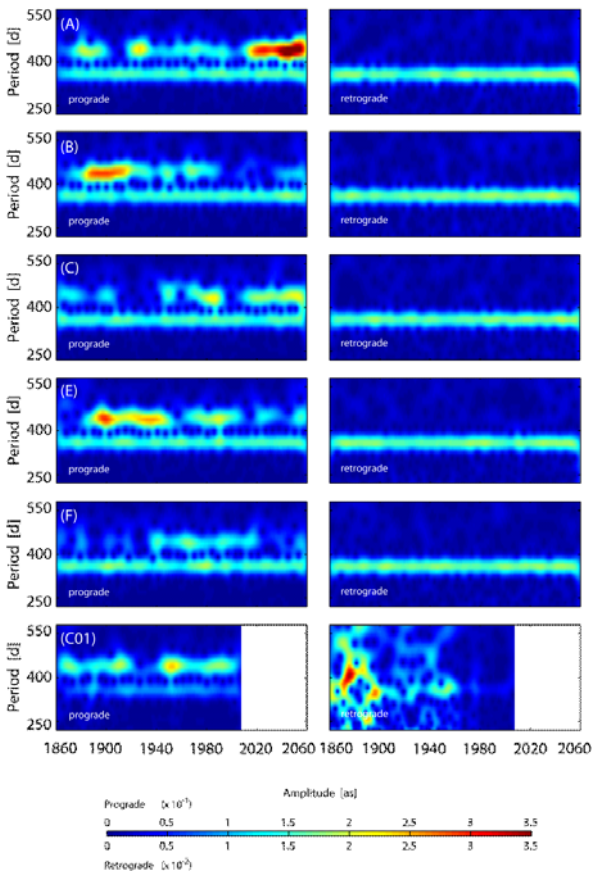

Fig. 4.2.2: Wavelet scalograms of the model results for polar motion from DyMEG under ECOCTH forcing (five scenario runs) and geodetic observations from the C01 series. Note the different scaling of the colour bar for prograde and retrograde scalograms.

In order to assess the influence of the choice of the initial values on the solution, an experiment has been performed for scenario run A by setting the initial values for polar motion to 0.5 as (red) and 1 as (green). The result is shown in Fig. 4.2.3. Depending on the initial values the time series departure significantly from each other during the first 60 years of the simulation. After this time DyMEG reaches a steady state, i.e. the influence of the initial values vanishes. Due to the large inaccuracy of the observations from 1860, the first 60 years of the simulated time series should be interpreted with care. However the experiment shows that the interpretation of the results after 1920 is uncritical.

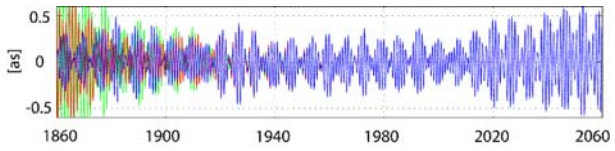

Fig. 4.2.3: Model results for polar motion from DyMEG under ECOCTH forcing (scenario run A) using different initial values for the integration.

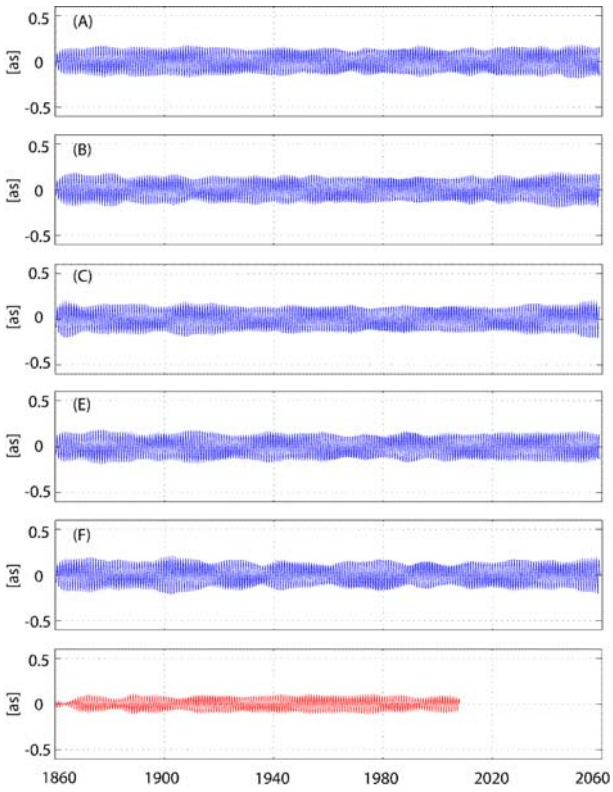

Fig. 4.2.4: Annual components of the model results for polar motion from DyMEG under ECOCTH forcing (x-components of five scenario runs) and geodetic observations from the C01 series as determined by wavelet filtering.

Signal analysis of the model results by means of wavelet filtering (SEITZ and SCHMIDT, 2005) reveals, that the annual components of all runs are characterised by rather stable amplitudes over the entire time span of 200 years (Fig. 4.2.4). However, the mean annual amplitudes of all runs amount to 0.16 as (arc seconds), which is almost twice as much as observed (0.09 as). This implies that the annual cycle is overestimated by ECOCTH. While the annual oscillations of the five results are very similar, there are large discrepancies between the modelled Chandler oscillations (Fig. 4.2.5).

While the annual component of polar motion is a forced phenomenon due to the annual variability of atmosphere and hydrosphere, the Chandler oscillation is a free rotational mode of the Earth which is caused by misalignment of figure axis and rotation axis. However since the Earth's body is deformable this misalignment would diminish, until both axes would coincide after few decades if no counteracting mechanism would perpetuate the Chandler oscillation. The deformations of the Earth's body which occur as a consequence of polar motion (so-called rotational deformations) are a back-coupling mechanism of polar motion on mass redistributions within the solid Earth as a consequence of centrifugal potential variations.

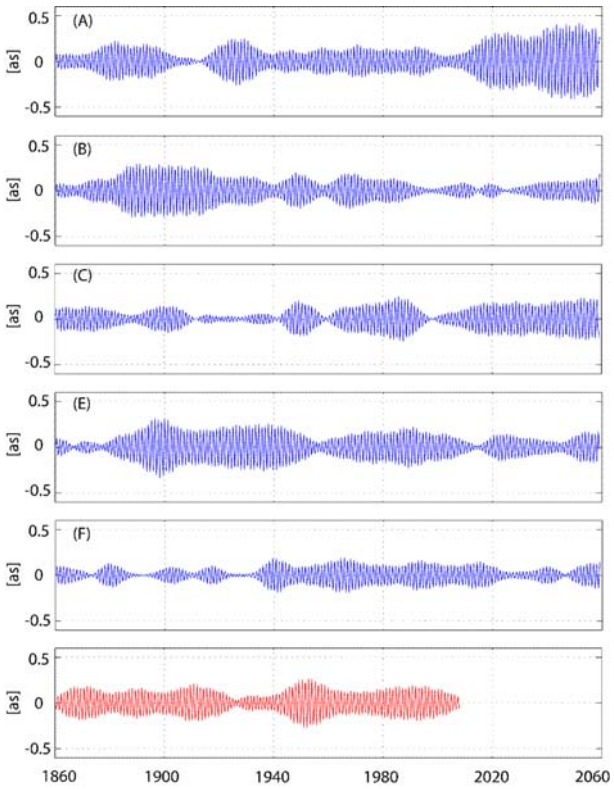

Fig. 4.2.5: Chandler components of the model results for polar motion from DyMEG under ECOCTH forcing (x-components of five scenario runs) and geodetic observations from the C01 series as determined by wavelet filtering.

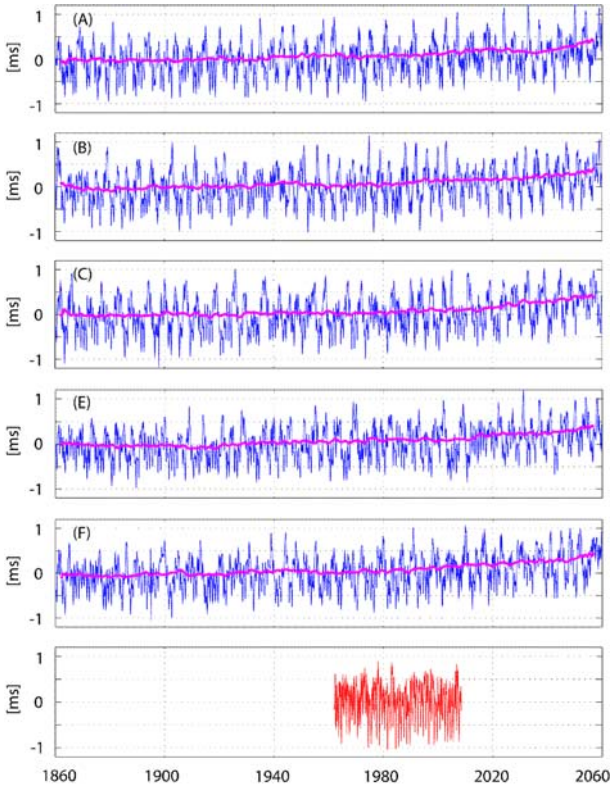

Fig. 4.2.7: Model results for ΔLOD from DyMEG under ECOCTH forcing (five scenario runs) and geodetic observations from the C04 series reduced by tides. Purple curves are running means over 15 years.

As described in section 3.2, the Chandler oscillation is modelled in DyMEG as a damped oscillation on the basis of rotational deformations and complex Love-Numbers. This way forced variations of Earth rotation due to atmospheric and hydrologic excitations influence the Chandler oscillation of the model. Obviously all runs of ECOCTH allow for the excitation of the Chandler oscillation, even though the shapes of the resulting curves are very different. But concerning the general signal characteristics (distribution of nodes and maxima) the runs are similar and agree well with the observations. Since the Chandler frequency is a resonance frequency of the Earth, energy is required in a spectral band close to the Chandler frequency in order to excite the oscillation. But since there are no periodic or quasi-periodic signals present in the Chandler frequency band of the spectra of the atmospheric and hydrospheric forcing, it is assumed that the necessary energy arises from background noise due to stochastic weather phenomena as simulated by ECOCTH. Further studies on the excitation of the Chandler oscillation by random variability in atmosphere and hydrosphere are provided in section 5.3 and by SEITZ and DREWES (2009).

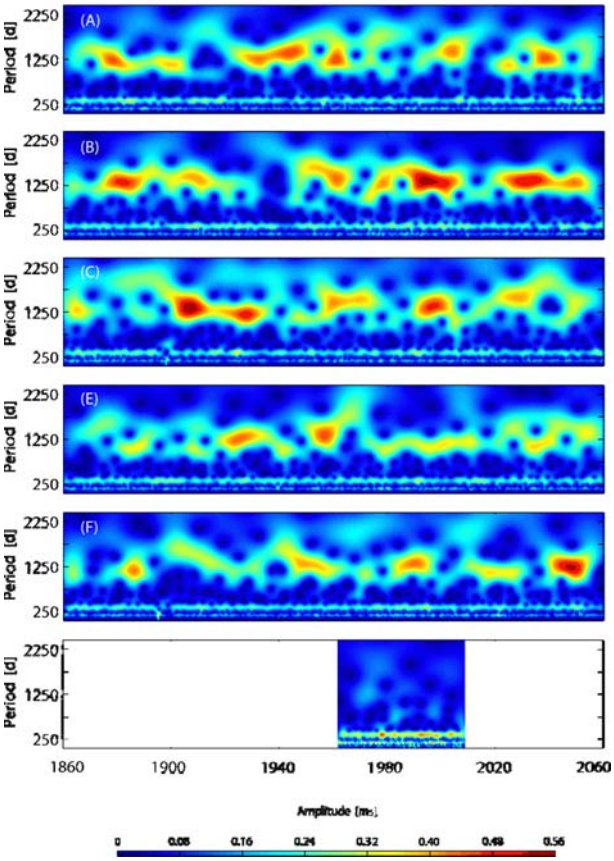

Fig. 4.2.8: Wavelet scalograms of the model results for ΔLOD from DyMEG under ECOCTH forcing (five scenario runs) and geodetic observations from the C04 series reduced by tides.

Variations of the length-of-day, i.e. the variation of the angular velocity of Earth rotation, are closely linked to solid Earth tides and winds. Especially the axial component of the atmospheric relative angular momenta which is related to zonal winds causes strong variations of ΔLOD with annual and semi-annual periods (SEITZ, 2004). The observed mean annual amplitude amounts to approximately 350 ms between 1962 and 2008, the mean semi-annual amplitude is approximately 290 ms. Fig. 4.2.7 compares the geodetic observations from the C04 series (lowest panel) with the model results of the five runs with DyMEG. As above (Fig. 4.1.3.) tides are removed from the observations. A running mean over 15 years is also displayed for the model time series. Respective wavelet scalograms of all curves are provided in Fig. 4.2.8.

When model results for ΔLOD are compared with geodetic observations it should be kept in mind that the available time series of ΔLOD is very inaccurate in the years before 1980 (i.e. before the VLBI era). Fig. 4.2.9 shows the observations together with the 3σ error margin which is much larger than the signal itself during the first two decades.

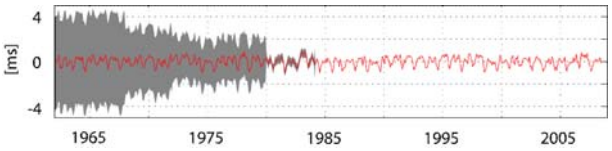

Fig. 4.2.9: Geodetic observations of ΔLOD from the C04 series reduced by tides. The grey curve shows the 3σ error margin of the observations.

Signal analyses of the model results reveal that the amplitudes of annual and semi-annual components are smaller than observed. For runs A, C, E, and F the mean amplitudes are around 220 ms (annual) and between 150 and160 ms (semi-annual). For run B both amplitudes are a bit larger (230 ms and 207 ms respectively). It can be concluded from the results, that the annual and semi-annual variability of the axial component of the relative angular momenta of ECOCTH is underestimated. Since the largest part of ΔLOD on these time scales is explained by zonal winds it is likely that especially the atmospheric axial relative angular momenta of ECHAM5 are too small. Similar problems were detected in previous studies using former versions of ECHAM (see SEITZ, 2004).

On the other hand there are pronounced signals in the spectral range of the model results between 1000 and 2000 days (2.7-5.5 years) which are significantly larger than in the geodetic time series. The observed fluctuations in this band are related to ENSO events during 1973, 1983 and 1998. Fig. 4.2.10 contrasts the C04 curve reduced by tides, annual and semi-annual components with a time series of the Southern Oscillation Index (SOI) which is a function of seasonal air pressure differences between Tahiti and Darwin (cf. section 3.1.2.3). The dimensionless values of SOI range between -30 and 30, where ENSO episodes are associated with negative SOI values. In order to demonstrate the clear relation between ΔLOD and SOI graphically, the SOI curves in Fig. 4.2.10 is scaled to the amplitude of ΔLOD by multiplying it with a factor of -35. The negative sign allows for a direct comparison of ΔLOD and ENSO. During the ENSO situations of 1973, 1983 and 1998 (black arrows) a clearly increased signal of ΔLOD is obvious.

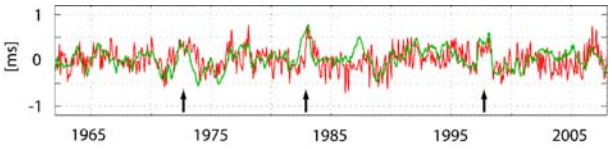

Fig. 4.2.10: Geodetic observations of ΔLOD from the C04 series (red, reduced by tides, annual and semi-annual component) in comparison with a time series of the Southern Oscillation Index (SIO, multiplied by -35).

As stated already in section 3.1.2.3 the temporal variability of ECOCTH on the ENSO time scale appears to be reasonable while the amplitudes of the signal are overestimated (see also section 5.2.1). This leads to modelled variations of LOD in the inter-annual spectral band that are too high by a factor of up to two. Especially run B, which also shows the strongest annual and semi-annual signals, features the highest variability between 1000 and 2000 days of the five runs.

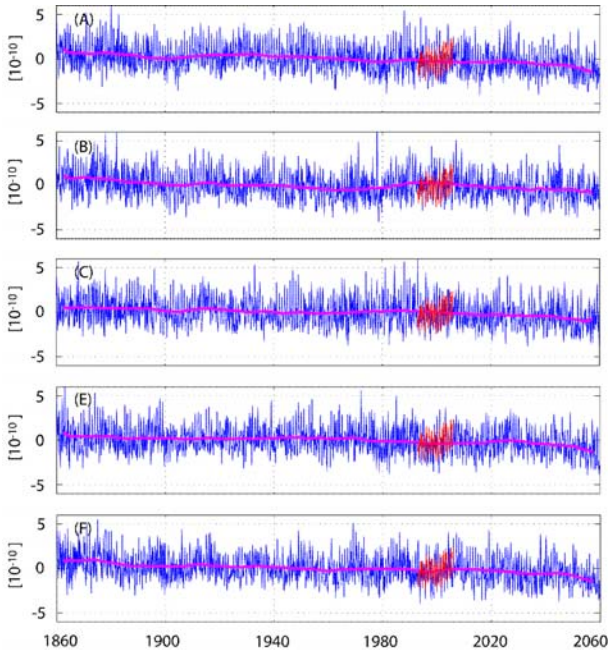

Fig. 4.2.11: Model results for ΔC_{20} in fully normalised representation from DyMEG under ECOCTH forcing (five scenario runs, blue) and geodetic observations from SLR analysis (red). Purple curves are running means over 15 years.

The curves of the running means of the model results over 15 years shown in Fig. 4.2.7 indicate a clear increase of ΔLOD until the year 2060. A detailed discussion of the causes of this increase predicted by DyMEG under ECOCTH forcing can be found in section 5.2.2.

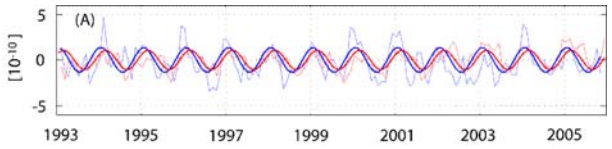

Fig. 4.2.12: Model results for ΔC_{20} in fully normalised representation from DyMEG under ECOCTH forcing (scenario run A, blue) and geodetic observations from SLR analysis (red). Thick curves are the respective annual oscillations.

The increase of ΔLOD is accompanied by a decrease of the spherical harmonic coefficient ΔC_{20} of the Earth's gravity field. The relation between both parameters has been addressed by BOURDA (2008). Time series of the variation of ΔC_{20} are shown in Fig. 4.2.11.

Our model results are compared with variations of ΔC_{20} from SLR analysis between 1993 and 2006. The SLR time series were provided from the JCET ILRS Analysis Centre (PAVLIS, 2006, private communication). Amplitudes of model results and SLR observations match well, and a negative secular trend of the running mean over 15 years is obvious. The annual cycles described by the curves are plotted for run A in Fig. 4.2.12. Both the signal amplitude (modelled: $1.3 \cdot 10^{-10}$; observed: $1.1 \cdot 10^{-10}$) and the phase relation (phase shift between the curves: 17 days) show a very satisfying agreement.

The comparison of the remaining four spherical harmonic coefficients of degree 2 (ΔC_{21}, ΔS_{21}, ΔC_{22}, ΔS_{22}) with corresponding SLR results is shown for run A in Fig. 4.2.13. Again amplitudes of SLR observations (from the same analysis as for ΔC_{20}) and model results agree quite well. The displayed time series of the coefficients of order 1 feature secular variations which are also present in the other runs, albeit with different amplitudes and temporal characteristics.

Time series of spherical harmonic coefficients of higher degree and order are computed by DyMEG on the basis of the atmospheric and hydrospheric pressure fields. However geodetic observations for comparisons are available for only 6 years (2003-2008) from GRACE analyses which impedes a reliable validation of the model results. Therefore time series of higher degree and order shall not be discussed at this point.

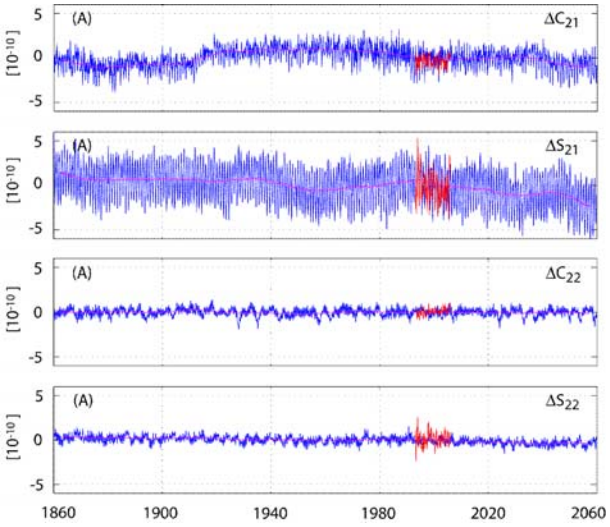

Fig. 4.2.13: Model results for ΔC_{21}, ΔS_{21}, ΔC_{22}, ΔS_{22} in fully normalised representation from DyMEG under ECOCTH forcing (scenario run A, blue) and geodetic observations from SLR analysis (red).

5. Scientific highlights

5.1 Tidal mixing

Ocean dynamics are classically divided into barotropic and baroclinic motions. Normally, ocean tide models are barotropic, decoupled from the ocean circulation. In the last decades, the existence of significant interactions between the barotropic tides and the ocean circulation became evident. These effects are important for both dynamical systems, the ocean circulation and the ocean tides.

A very strong interactive effect between ocean tides and ocean circulation is the mixing induced by internal tides, which are generated at topographic features, e.g. oceanic islands, oceanic trenches and mid-ocean ridges. The internal tides are breaking and thus contribute to vertical mixing processes in the ocean (GARRETT, 2003). It is taken as evident that the internal tides enhance mixing processes and that they are not spatially uniform, rather dependent on the roughness of the ocean bottom topography. This is supported by observations along a section at the Brazil Basin (TOOLE et al., 1997), showing an enhanced mixing over rough topography of the Mid Atlantic Ridge. These studies suggest that the bottom topography plays an important role in the spatial distribution of the vertical mixing. Further LEDWELL et al. (2000) demonstrated a modulation of

dissipation over the spring neap cycle and therefore emphasize the essential role of internal tides. Due to the fact that internal tides contribute to mixing processes in the ocean, a large amount of tidal energy is provided to mix the ocean. Indeed, this amount of energy is necessary to explain the global ocean circulation (MUNK and WUNSCH, 1998).

Most ocean general circulation models (OGCMs) parameterize the vertical mixing with a horizontal uniform approach. Usually the mixing rates are assigned by tuning the model's meridional transports of heat and mass. This method is problematic since it adjusts the ocean properties to the presently observed state of the ocean and might not be appropriate for a changing ocean. This in turn challenges of course any climate prediction. Thus, more physically based parameterizations of vertical mixing are necessary.

Only a few models take into account the influence of gravitational tides. They can be divided into two groups, the first one directly includes tidal velocities, e.g. deduced from observations (LEE et al., 2005) and the second one takes into account an energy field determined from tidal models (SIMMONS et al., 2004; MONTENEGRO et al., 2007). The first group neglects the internal tide generation in the deep ocean, where the latter one does not account for mixing in shallow waters. None of these models explicitly force the global tides and thus neglect nonlinear interactions between the ocean's general circulation and barotropic tides. The reason is mainly due to numerical stability problems (SCHILLER, 2004) and considerably different timescales of OGCMs and tidal models. However, it is very important to account for variations in tides through changing resonance conditions of the world ocean, e.g. due to sea level rise or melting pole caps (ARBIC et al., 2004). In turn, these variations of the tides might change the vertical mixing and thus influence the meridional heat fluxes.

The OMCT1 described in Chapter 2.2 was the first ocean model with an explicit ocean tide forcing (THOMAS et al., 2001), it allows for an interaction of the ocean tides with ocean circulation. The ocean tides affect the low frequency motion via nonlinear bottom friction and vertical mixing. In this Chapter we show that the tides have a strong effect on the ocean circulation and that they improve the description of the present state of the North Atlantic on large scales.

5.1.1 Tidal mixing in OMCT2

In the OMCT2 the vertical mixing is parameterized with a Richardson number dependent mixing term following PACANOWSKI and PHILANDER (1981). The Richardson number is given through

$$Ri = \frac{N^2}{\left(\frac{\partial U}{\partial z}\right)^2},$$

N is the Brunt-Väisälä frequency and $\left(\frac{\partial U}{\partial z}\right)$ the vertical velocity shear. The vertical diffusivity is defined in the model as

$$A_v = A_{v0}\,(1 + C \cdot Ri)^{-2} + A_b + A_w$$

where A_{v0} and C are constants, A_b is a small constant background diffusivity representing mixing induced by internal wave breaking and A_w is the mixing generated by the wind and the sea surface.

In regions where the tidal velocities are large the vertical velocity shear increases in the bottom layer through bottom friction. In the following our study focuses towards the North Atlantic region where the highest tidal velocities occur (Fig. 5.1.1).

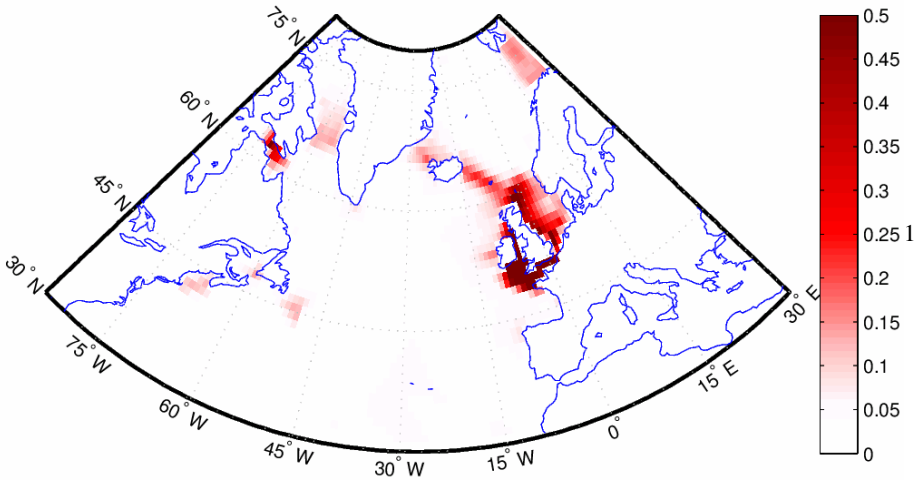

Fig. 5.1.1. The amplitudes of M2 tidal velocities in the North Atlantic (m/s).

In the regions of high tidal velocities the inverse Richardson number becomes up to ten times larger due to the tidal velocity shear than in the model without tides. This amplification of mixing is localized to a few small regions, but has a strong effect on the ocean dynamics in the North Atlantic.

5.1.2 Effect of tidal mixing on ocean water mass properties

The sea surface temperature in the North Atlantic is strongly influenced by the subtropical gyre, which transports large amounts of heat to northern latitudes (see Chapter 3.1.2.2). Global ocean models which are used in state-of-the-art climate models have to get along with a coarse resolution of the global ocean. Thus, the subtropical gyre in particular the North Atlantic Current (NAC), the extension of the Gulf Stream, is not properly represented in the models, which results in a temperature bias in the North Atlantic region (IPCC, 2007). In our model the NAC crosses the Atlantic too zonally at around 40 degree north, instead of meandering in north eastward direction.

The effect of ocean tides change the pathway of the NAC and thus reduces the temperature bias in the middle of the North Atlantic region (Fig. 5.1.2). Further, in the Nordic Seas and the Labrador Sea, the ocean tides lead to a cooled sea surface temperature, which is closer to observations, as well (MÜLLER et al., 2009).

In the future scenarios the ocean tides have the opposite impact, in the Nordic Seas the warming in increased, and in the North Atlantic region the warming is damped in some regions the sea surface temperature even gets cooler in the future (Fig. 5.1.3). These changes are attributed to a modification of the pathway of the NAC and further research has to be done in order to understand this strong effect of the ocean tides on the currents of the North Atlantic.

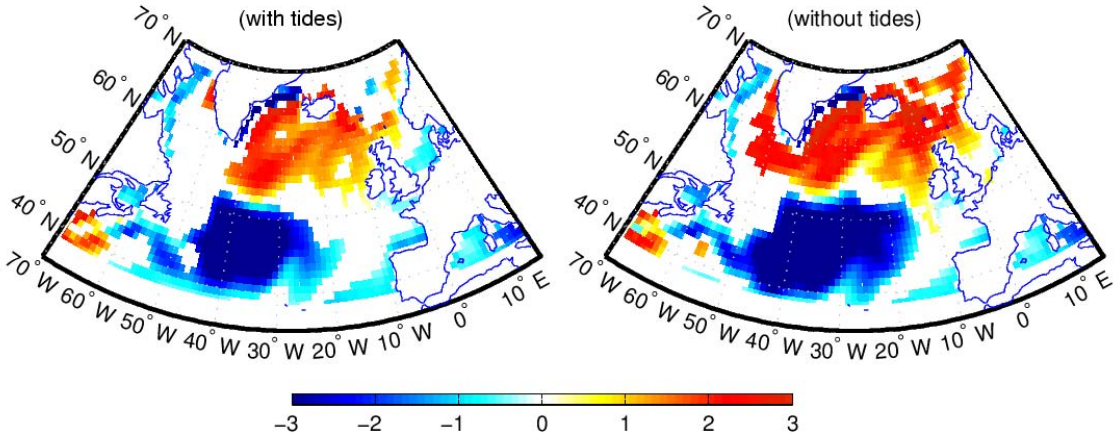

Fig. 5.1.2: Deviation of the sea surface temperature (long term mean 1950-1999) in the North Atlantic from Levitus data (K). Left: Ensemble mean with ocean tides. Right: control run without ocean tides (masked by 95% significance with the ensemble standard deviation).

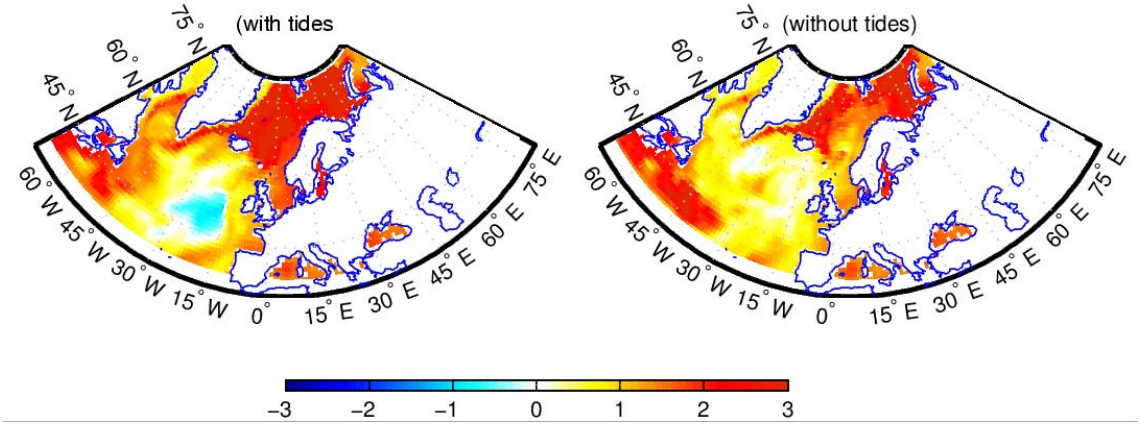

Fig. 5.1.3: Increase of the sea surface temperature (K) between the long term mean of (1950-1999) and (2030-2059) Left: Ensemble mean with ocean tides. Right: control run without ocean tides.

5.2 Secular and decadal variations

5.2.1 Coupled simulation of Earth Rotation Parameters

An experiment with the coupled ECOCTH model (see Chapter 3.1) was conducted. Ensemble member runs only differing in their initial conditions started in 1860. The simulation period ended in the year 2000, from then on the A1B scenario was applied to the model runs ending in the year 2060. In this chapter an AAM analysis of the ECHO-G and ECOCTH A1B scenario runs follows a brief analysis of the ECOCTH simulation period.

The global 2m temperature anomaly of the ECOCTH simulations shows very small departures from the observed time series (Fig. 5.2.1). The inter-annual variability is overestimated strongly and results from an overestimation of ENSO by about 300 percent. The nature of the ensemble mean implies that it fluctuates less intensely in time.

From the ECOCTH simulations, AAM have been calculated. The power spectrum of the axial AAM component of NCEP, ECHAM5 standalone and ECOCTH is plotted in Fig. 5.2.2. The dominant annual and semiannual signals are comprehended by the ECOCTH containing slightly less energy than NCEP and ECHAM at these frequencies. An analysis in the time-frequency domain by wavelet decomposition is not advisable as the ECOCTH is a free model and thus generates SST oscillations internally and independent of time, whereas the ECHAM5 model is forced by time dependent SSTs.

In the power spectrum, strong ECOCTH overestimations are found at the ENSO region. The unrealistically strong ENSO amplitude leaves a fingerprint in the temperature time series and the axial AAM spectrum as well. It seems, as if the deviation is limited to the frequency band mentioned and does not disturb other parts. In a high frequency region with frequencies of four to six times a year the free coupled model (ECOCTH – red) comprises higher energy densities than the standalone runs (ECHAM – blue). Here, the free coupled model is closer to the atmospheric reanalysis, demonstrating that the dynamic coupling might enhance the atmospheric variability on these time scales effectively. Except for the ENSO estimation no significant systematic error can be revealed at this point within the free coupled simulations. As the model succeeds in following major AAM and global 2m temperature structures in the past, a scenario run is conducted to examine possible future long term trends under a climate change scenario.

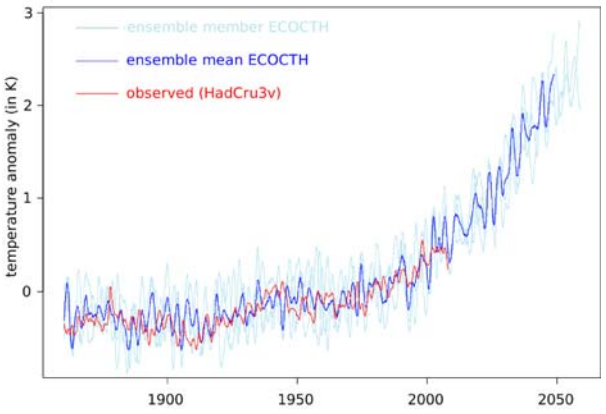

Fig. 5.2.1: Global combined land-sea 2m temperature anomaly time series for ECOCTH simulations – three members (light blue), ensemble mean (blue) and observed HadCruTem3v values (red).

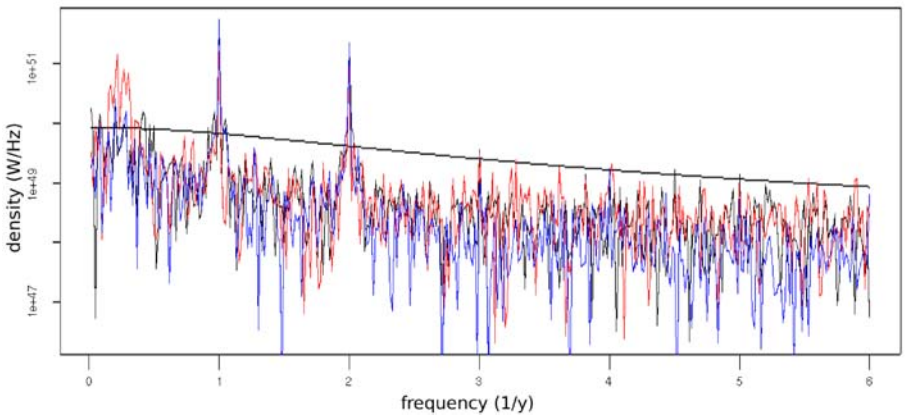

Fig. 5.2.2: Global axial AAM (mass/non-IB+motion) power spectrum for ECOCTH ensemble mean (red), ECHAM5 stand-alone ensemble mean (blue), NCEP (black) and 95 percent confidence level (fullblack) for 1948 to 2006 period.

5.2.2 Axial AAM long-term trends in 21st century scenario runs

Future climate conditions explicitly depend on future boundary conditions. Future boundary conditions are uncertain and not subject of the meteorologists or climatologists theirselves. In climate change studies the research processes as follows: Different sets of possible future boundary conditions are derived from economic, technical and demographic models. These scenarios are independently applied to climate models. The results of the climate models should not be interpreted as particular climate forecast. They

are rather the outcome of a model given the specific scenario applied and climate model version used. For this work only one scenario is used. All common scenarios do not differ much in the beginning of the 21st century; therefore the results of different scenarios show a much bigger spread in the second half of the 21st century (IPCC, 2007). To make statements over future climate conditions in the second half of the century all common scenarios should be respected. The AAM study in the following section ends in the year 2060. The axial AAM long-term trend of the free coupled model ECOCTH and the coupled atmosphere ocean model ECHO-G (LEGUTKE and VOSS, 1999; MIN et al., 2005; MIN et al., 2006), which was part of the 4th assessment report of the IPCC, will be analysed.

A lot of studies project an increasing global axial AAM for the 21st century. LORENZ and DEWEAVER (2007) investigated the zonal wind response to global warming. They analysed the IPCC models under climate change scenarios and obtained an amplification of zonal wind in global terms. The dynamic reason of the increase cannot be retraced easily. Strongly increased temperatures in the upper tropics enhance the meridional temperature gradient. In the inner tropics the tropopause level is rising. Therefore, the tropopause slope towards the poles is getting intensified. Stratospheric cooling and tropospheric warming increase the meridional temperature gradient and due to the thermal wind balance, westerlies become stronger. The increase in kinetic energy at the tropopause level is consistent with the rise in tropopause height because synoptic waves are trapped in the troposphere. This does not contradict with the popular impression that the Arctic is especially warming, as the Arctic warming is primarily confined to the near surface levels.

In his study de VIRON, DEHANT, GOOSSE, and CRUCIFIX (2002) analysed a CMIP2 (MEEHL et al., 2000) model ensemble with an increase in CO_2 concentrations of one percent per year which is higher compared to the A1B-scenario (~0.6 percent per year). In the CMIP2 study, the HadCM2 model showed a 0.53 ms/century trend in ΔLOD in the AAM motion-term while other models only reached 0.1 ms/century. The discrepancy between different models in the ΔLOD trend indicates that model uncertainty is an important issue.

The uncertainties of the ECOCTH and ECHO-G A1B scenario runs in Fig. 5.2.3 are again deduced from bootstrapping. As the number of ensembles is critically small the subset sample size was set to five years to ensure sufficient possible combinations. After drawing 1,000 bootstrap samples, a LOESS smoother with a 20 year bandwidth was applied to every sample. The reference is the 2000 to 2009 ensemble mean. Both models induce a significant positive trend in the axial AAM motion term for the 2000 to 2060 period. The ECHO-G model possesses a higher uncertainty in general embodied by a broader ensemble spread. Interestingly, the strongest trend is simulated for the period between 2025 and 2045, thereinafter the slope flattens. In contrast, the ECOCTH simulates the strongest increase in the last two decades and reaches an AAM motion term induced lengthening of LOD nearly twice as high as ECHO-G for the year 2060. A linear trend estimation does not seem very suitable because the ECHO-G somehow shows a stepwise increase, whereas the ECOCTH time series rather follows an exponential law.

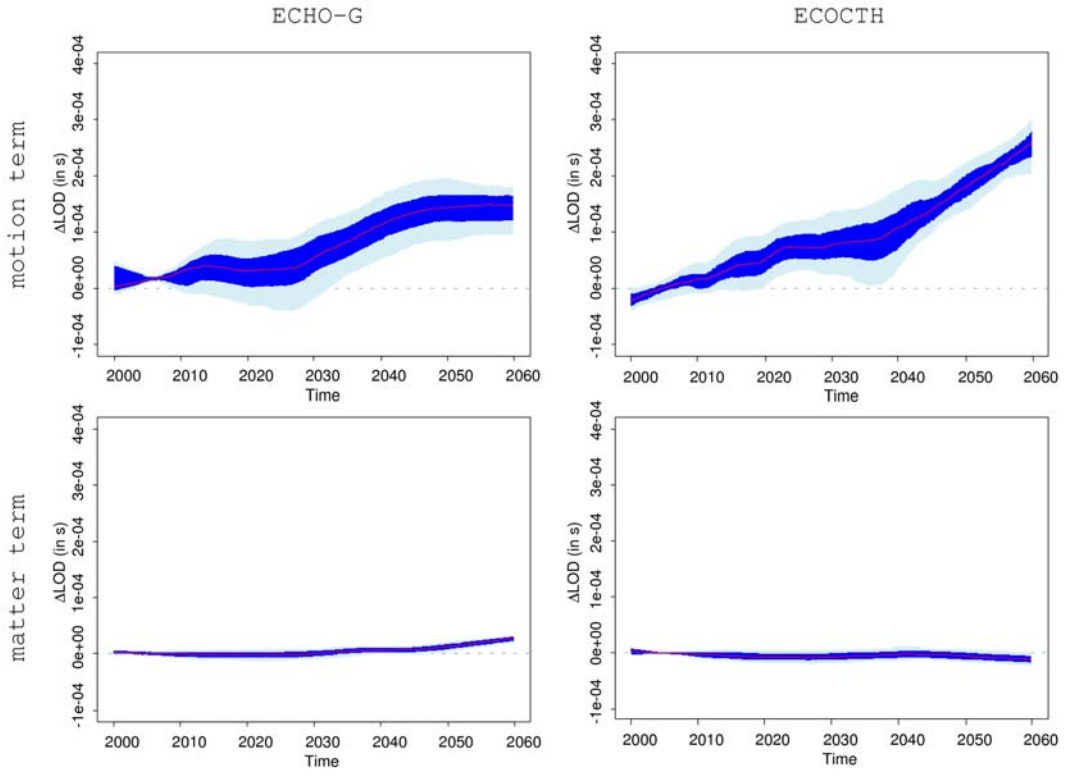

Fig. 5.2.3: AAM motion (top) and matter (bottom) term effects on ΔLOD of ECHO-G (left) and ECOCTH (right), 25th to 75th percentile range (blue band), 5th to 95th percentile range (light blue band) and median (red line).

The matter term trends have much smaller uncertainties and do not differ significantly from zero until 2045 in case of ECHO-G and not at all for ECOCTH at the five percent significance level. De Viron deduced a compensating effect of the matter term. For the year 2100 he estimated an expectation value of the CMIP2 model ensemble by approximately -0.075ms. His estimation is not backed by the two models in this analysis. ECOCTH shows a slightly negative but not significant trend, while ECHO-G even deduces a positive trend. A positive trend in the matter term would mean that under the assumption of mass conservation, more mass will be concentrated at lower latitudes equivalent to higher surface pressure at low latitudes.

In the year 2060, the increased axial AAM (matter/non-IB+motion) within the model would cause a lengthening of a solar day by about 0.17±0.03 *ms* for ECHO-G and 0.26±0.03 *ms* for ECOCTH. The estimated errors only reflect the model uncertainty. Of course, other sources of errors exist, for instance the scenario itself is "uncertain". However it should be kept in mind that the model Δ*LOD* result comprehends solely the effect of the atmosphere which is superimposed by other effects on the inter-decadal/centurial time scales. To give an impression of the size of the atmospheric effect, other effects are estimated for the year 2060 and summarised in Tab. 5.2.1 referring to de Viron.

Tab. 5.2.1: Estimates for the 2000 to 2060 trend in ΔLOD (in ms/60y) (de Viron et al., 2002).

Effect	60 year trend in Δ*LOD* estimate
Tidal friction	1.2
Contininental. water reservation	-0.36
Post glacial rebound	-0.3
Sea level (thermal exp.)	0.03
Glacier melting	0.024

The Earth constantly loses angular momentum to the Moon due to tidal friction. This effect is very strong on the centurial time scale. Unfortunately, no error estimates are available for the effects, but tidal friction effect estimates have a relatively high accuracy. The accuracy of the estimates decreases from the top to the bottom of the table. Continental water reservation leads to an decreased moment of inertia resulting in a faster Earth rotation. The third effect accounts for the rise of continents which were covered by glaciers in the past. Siberia and Fennoscandia are still rising.

In a changing climate the distribution and concentration of water and ice masses will change when temperatures increase. The last two effects can directly be linked to climate change.

The effect of an increased AAM on LOD in a future climate has the same order of magnitude as that of post glacial rebound of continents or the reservation of continental water. The differences and discrepancies between certain models in predicting future LOD conditions point at high uncertainties. Interestingly, from the year 2040 on the models start diverging. This behaviour is rather similar to the projections of the global 2m temperature, where the models are in high accordance until approximately 2040 and start diverging in the following (IPCC, 2007).

5.3 Forcing mechanisms of the Chandler oscillation

Forced polar motion due to the redistribution and motion of mass elements in the Earth system is superposed by free oscillations of the Earth, like the Chandler wobble and the nearly diurnal free wobble. As described in Chapter 3.2, the Chandler oscillation is not explicitly predetermined in DyMEG with respect to its period and damping, but reproduced by the model based on geometrical and rheological parameters. Since the effects of rotational deformations are regarded, the model reacts on polar motion. This back-coupling mechanism of rotational deformations causes perturbations of the second-degree spherical harmonic geopotential coefficients ΔC_{21} and ΔS_{21} which are directly linked to the elements ΔI_{13} and ΔI_{23} of the tensor of inertia. Since these elements have the largest influence on polar motion, time-varying mass distributions are accompanied by modified resonance conditions and thus affect the free polar motion of the model. Therefore DyMEG allows for studies of the interactions between forced and free polar motion. The amplitude of the Chandler wobble would diminish within a few decades due to friction without perpetual excitation. In Fig. 5.3.1 the x-component of an unforced run (i.e. without tidal and geophysical excitations) with DyMEG is shown in a normalised representation. It can clearly be seen, that the amplitude of the Chandler oscillation is reduced by half after about 25 years.

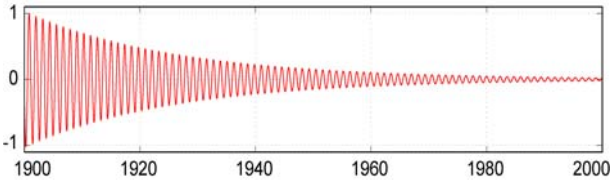

Fig. 5.3.1: Free polar motion of DyMEG without excitations applied (x-component, normalised).

However, spectral analyses of geodetic observations over the last century reveal significant variations of the Chandler amplitude, which implies the existence of some excitation mechanism. In Fig. 5.3.2 (top), the observed polar motion is displayed for the period between 1900 and 2006 (x-component after removal of a linear trend). As the two prominent signal components, i.e., the Chandler and the annual oscillation are almost circular; the y-component

looks very similar. Until 1962 the observation time series is based on optical astrometry (VONDRAK et al., 1995). Subsequent values are taken from the C04 series of the IERS (DICK and RICHTER, 2008) which is mainly based on space geodetic observations. By means of wavelet filtering the signal is decomposed into its two main constituents, the Chandler oscillation (Fig. 5.3.2, middle) and the annual oscillation (bottom). The Chandler oscillation features much stronger amplitude variations than the annual signal which has been rather uniform during the last century. Although the accuracy of the elder astrometric data is two orders of magnitude below the accuracy of modern space geodetic techniques which is up to 0.1 mas, the amplitude variations are significant since the signal exceeds some 100 mas.

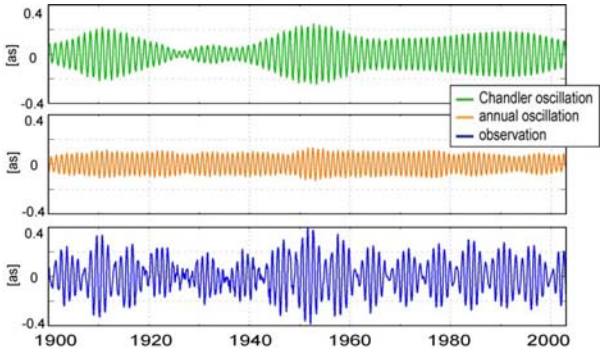

Fig. 5.3.2: Geodetic observations of polar motion (x-component, linear trend removed) between 1900 and 2000 (top) and the Chandler (middle) and annual (bottom) signal component determined by wavelet filtering.

The origin of the amplitude variations and thus the reason for the perpetuation of the Chandler wobble has been under discussion since many years (e.g., GROSS, 1986; HINDERER et al., 1987; SIDORENKOV, 1992; FURUYA et al., 1996; AOYAMA et al., 2003). Since the Chandler wobble is a resonance oscillation of the Earth, potential excitation mechanisms require energy in a band close to the Chandler frequency in order to excite the free polar motion and thus to counteract its damping. By now, it is understood that the Chandler oscillation is excited by a combined effect of atmosphere and ocean. However the individual contributions of these two subsystems could not be fully assessed yet. Earlier, GROSS (2000) and BRZEZINSKI and NASTULA (2002) concluded from spectral analyses of atmospheric and oceanic angular momentum variations, that the excitation energy which is contained in a spectral band between approximately 400 and 500 days is sufficient to excite the observed Chandler oscillation between 1985 and 1996. Both studies were based on the reanalyses of NCEP/NCAR (KALNAY et al., 1996) and an ocean model of the Massachusetts Institute of Technology (MARSHALL et al., 1997). While the analyses of GROSS (2000) revealed, that the largest part of the excitation energy originates from oceanic bottom pressure variations, BRZEZINSKI and NASTULA (2002) concluded, that the contribution of atmosphere and ocean is nearly equal.

Spectral analyses give no hint for increased excitation energy in either spectra of atmospheric and oceanic excitations in the Chandler band (GROSS, 2000; SEITZ et al., 2004; STUCK et al., 2005). Though different patterns of climate variability exist on inter-annual time scales (e.g. the Quasi-Biennial Oscillation, the North Atlantic Oscillation or El Nino), none of these phenomena gives rise to any periodic or quasi-periodic excitation mechanism in the Chandler frequency range as they affect differing parts of the spectrum. However, ongoing stochastic weather phenomena lead to a random distribution of excitation energy in the whole atmospheric spectrum (white noise). As atmosphere and hydrosphere interact, the stochastic signal is carried forward from the atmosphere into the hydrosphere. The resulting random distribution of energy affects the spectra of atmospheric and hydrospheric excitations entirely.

In the following the influences of atmosphere and ocean on the Chandler wobble are analysed quantitatively and with respect to their temporal variations by means of wavelet filtering. Bandpass filtered excitations are introduced into DyMEG. We compare the numerical results for polar motion with geodetic observations in the time domain (Chapter 5.3.1) and enter into the question if a purely flat distribution of excitation energy is capable of provoking a resonant reaction of the rotating Earth via rotational deformations (Chapter 5.3.2).

5.3.1 Atmospheric and hydrospheric excitation of the Chandler oscillation

In a first experiment (for more details see SEITZ and SCHMIDT, 2005), DyMEG is driven by realistic geophysical and gravitational excitations. Geophysical forcing is limited to the primary fluid components of the Earth system, i.e., the atmosphere and the ocean. Contributions of other subsystems are neglected since their influence on polar motion is much smaller on seasonal to inter-annual time scales. Atmospheric and oceanic angular momenta were deduced from the NCEP reanalyses and the unconstrained version c20010701 of the global ocean circulation model ECCO which has already been applied in the investigations described in section 4.1. Again the run covers the time span between 1980 and 2002.

In section 4.1 the angular momentum time series were introduced into DyMEG with their full spectral content (cf. Fig. 4.1.1 for the numerical results with combined atmospheric and oceanic forcing). It has been shown that the agreement between modelled and observed polar motion is excellent, and the study with separated forcing revealed the importance of both the atmospheric and the oceanic angular momentum variations for the excitation of the Earth's free oscillation. Either model result featured a clear signal in the Chandler band over more than two decades. As the Chandler frequency is a resonance frequency of the Earth, the amount of energy which is contained in the respective frequency band of the excitations is decisive for

the reaction of the Earth. Based on this consideration it is studied, if the free rotation of DyMEG is excited by resonant interaction when the model is forced with bandpass filtered angular momenta. Therefore, a wavelet filter with a passband between 400 and 460 days is applied to the excitations. This narrow bandwidth of approximately +/- 30 days around the Chandler period is chosen in order to avoid spectral leakage from the adjacent annual into the Chandler band.

In the following, solely the tensor elements $\Delta I_{13}(t)$ and $\Delta I_{23}(t)$ are regarded. Other deviations of the tensor influence polar motion only marginally. The effect of relative angular momenta does not exceed a few percent of the pressure driven excitations. They have comparatively little influence on the amplitude of polar motion and do not affect its general characteristics substantially (GROSS, 2000; SEITZ et al., 2004). Therefore, relative angular momenta shall also be neglected. For validation, the model time series is subsequently compared with the "observed" Chandler oscillation, which has been determined from the geodetic observations applying the same filtering method (cf. Fig. 5.3.2, top). The wavelet filter procedure is described in detail by SEITZ and SCHMIDT (2005).

The extracted signals of the spectral band between 400 and 460 days of the angular momentum series are introduced into DyMEG. Initial values for the integration are taken from the actually "observed" Chandler oscillation. In order to achieve consistent results, the filtering of the observations has been performed with identical parameters as the filtering of the atmospheric and oceanic excitations.

Applying no further excitations, this experiment yields the polar motion series displayed in Fig. 5.3.3 (x-components). As clearly visible, the filtered excitations of both the atmosphere and the ocean are capable of exciting the free polar motion of the model. The result with filtered NCEP excitations (Fig. 5.3.3 a) features an enhanced Chandler signal between 1984 and 1987. Using filtered ECCO excitations, the free polar motion of DyMEG (Fig. 5.3.3 b) remains rather stable before its amplitude decreases slightly after 1995. The lower panels of Fig. 5.3.3 show the integral signal energy that is contained in the prograde Chandler band of the respective complex-valued excitation time series $g(t) = \Delta I_{13}(t) - i\, \Delta I_{23}(t)$ between 400 and 460 days. This signal energy has been determined by means of wavelet-transformation. For details see SCHMIDT (2001). The maxima of the energy and the maxima of the Chandler amplitude are not always syncing. Obviously not only the amount of excitation energy in the Chandler band but also the instantaneous phase relations of the excitations and the Chandler wobble are very important. Hence, the knowledge of the absolute amount of excitation energy does not allow for a definite conclusion of the resulting Chandler amplitude. Nevertheless, this experiment reveals, that the energy of the atmospheric and oceanic excitations is high enough to counteract the damping of the Chandler wobble.

Now the bandpass filtered excitations of NCEP and ECCO are introduced into DyMEG simultaneously. In Fig. 5.3.4 the resulting polar motion and the actually observed Chandler oscillation are contrasted. The agreement between both curves is excellent. Thus the correlation coefficients for the x- as well as for the y-component (not shown) are 0.99, the corresponding RMS differences amount to 16.2 and 16.6 mas. For the entire period, the characteristics of the observations, i.e., the increase of the Chandler amplitude between 1980 and 1990 and the decrease after 1993, are in concordance with the free polar motion of DyMEG.

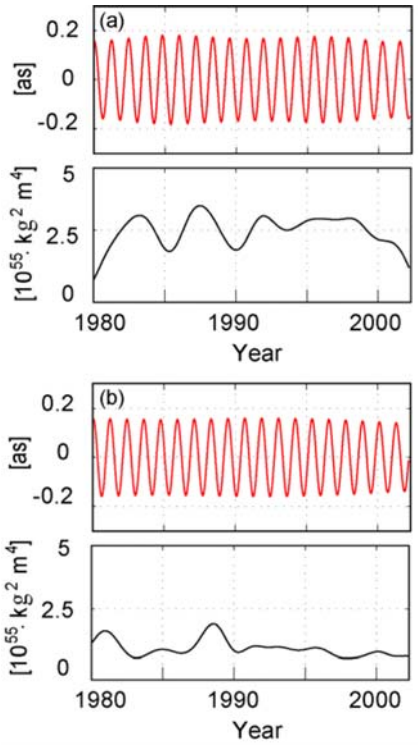

Fig. 5.3.3: Model results for polar motion (x-component) applying band-pass filtered (a) atmospheric and (b) oceanic time series of the tensor elements $\Delta I_{13}(t)$ and $\Delta I_{23}(t)$ (upper panels) in comparison with the integral wavelet energy of the excitations in the spectral band between 400 and 460 days (lower panels).

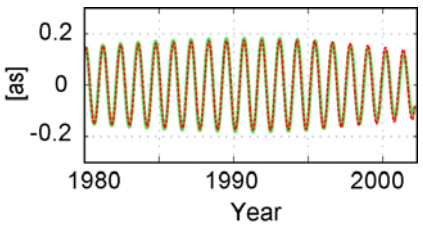

Fig. 5.3.4: Model results for polar motion (x-component) applying the combined bandpass filtered atmospheric and oceanic time series (NCEP+ECCO, red dashed). For comparison, the Chandler oscillation deduced from the C04 series by means of wavelet filtering (cf. Fig. 5.3.1) is added in green.

5.3.2 Noise as excitation mechanism of the Chandler oscillation

In a second experiment (for more details see SEITZ, 2004; SEITZ, 2005b; SEITZ et al., 2005), the excitations g(t) are substituted by equally distributed random numbers (white noise) from the interval [-1,+1] (Units [kg m^2]). This purely synthetic excitation is multiplied by a constant factor l which corresponds to a variation of the noise level. Instead of $\Delta I_{13}(t)$ and $\Delta I_{23}(t)$ two of these time series are introduced into DyMEG. As expected, no reaction of the gyro becomes obvious for small values of l. For $l = 1\times10^{27}$ first effects on the free rotation of DyMEG are visible as the damping is attenuated. In Fig. 5.3.5 the x-components of polar motion are displayed for three runs over 100 years (1900-2000) which are computed using the three different noise levels of $l = 1\times10^{28}$, $l = 1\times10^{29}$, and $l = 1\times10^{30}$. Initial conditions are identical for all runs. Analogous to Fig. 5.3.3 the integral wavelet energy in the Chandler band (400-460 days) is shown, too.

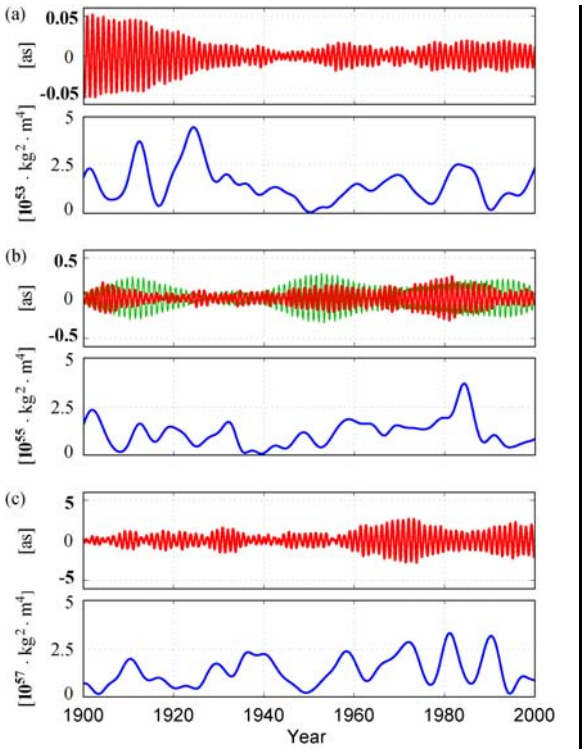

Fig. 5.3.5: Model results for polar motion (x-component) applying three different time series of equally distributed random numbers from the interval (a) [-1×10^{28}, +1×10^{28}], (b) [-1×10^{29}, +1×10^{29}], (c) [-1×10^{30}, +1OL215\f"Symbol"\s1210^{30}] kg m^2 instead of $\Delta I_{13}(t)$ and $\Delta I_{23}(t)$ (respective top panels) in comparison with the integral wavelet energy of the excitations in the spectral band between 400 and 460 days (lower panels). For comparison, the Chandler oscillation deduced from the C04 series is added in green in the upper panel of (b).

For $l = 1\times10^{28}$ the model result is characterised by strong damping. The amplitude of polar motion diminishes quickly and remains on a small level. Obviously the excitation energy is too low in order to perpetuate the Chandler oscillation as it is observed. The forcing with $l = 1\times10^{30}$ leads to a clearly increased Chandler amplitude (up to several arc seconds) since the excitation energy is too high. For $l = 1\times10^{29}$ the characteristics of the resulting free polar motion of DyMEG corresponds with the observations. It is shown that the Chandler oscillation can be excited over a century and longer alone by white noise. To support these results, the experiment is repeated with another white noise excitation series of the same noise level ($l = 1\times10^{29}$) over a time span of 1000 years (1900-2900). Again it can be seen that the characteristics of modelled and observed Chandler oscillation are similar.

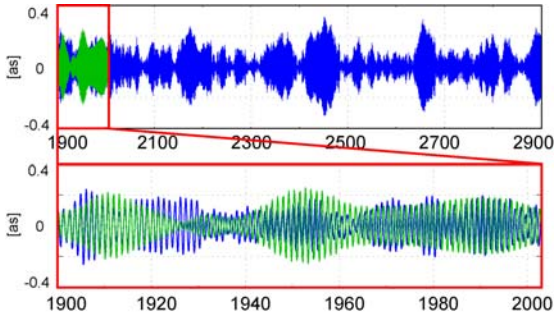

Fig. 5.3.6. Model results for polar motion over 1000 years (x-component) applying equally distributed random numbers from the interval [-1×10^{29}, +1×10^{29}] kg m^2 (top). The lower panel is a zoom on the period 1900-2006 and compares the model result with the observed Chandler oscillation (green).

The noise level, which is necessary for the perpetuation of the Chandler amplitude corresponds to the noise level which is described by the atmospheric and oceanic excitations (cf. Fig. 5.3.3). As above, the maxima of the energy and the maxima of the Chandler amplitude are not always syncing. Hence, this result supports the assumption, that not the energy level alone, but also the instantaneous phases of the random excitations are very important for the excitation of the Chandler wobble. The characteristics of the free polar motion resulting from the white noise experiment corresponds to the considerations of JEFFREYS (1962) who gives a descriptive comparison of the Earth's free polar motion with a pendulum:

> *Imagine a massive pendulum, at which several boys discharge peashooters. The hits occur at irregular intervals, but gradually build up a vibration in the natural period of the pendulum. The amplitude attained is limited by the damping. But the motion is due simply to the occurrence of an excess of impulses producing motion near one phase rather the opposite, and if the hits are at random intervals there will come a time when the excess is the other way and the motion may die down or be reversed.*

The performed experiments identify the stochastic atmospheric and oceanic pressure fluctuations to be the prominent hurriers of the Chandler oscillation. Which atmospheric

and oceanic processes are responsible for the noise, cannot be resolved in detail. It is assumed that purely stochastic atmospheric variations (weather) contribute essentially to the noise. As atmosphere and oceans interact, the stochastic signal is carried forward from the atmosphere into the oceans.

6. Conclusions and outlook

The project performs considerable progress in connecting integral parameters of the Earth as vector of rotation, surface shape or gravity field and their temporal variability with small-scale processes within the Earth system proper. A kind of analogy is given by the Gaussian theorem which relates fluxes at the surface A of a body to changes in its Volume V:

$$\iint_A \vec{v} \cdot \vec{dA} = \iiint_V \vec{\nabla} \cdot \vec{v}\, dV$$

where $\vec{v}$ is the velocity vector. Terrestrial and satellite observations provide the first mentioned planetary quantities, geological data from the atmosphere, ocean and solid Earth the variable state of the globe. It was and is the general objective of the research programme to understand and quantify this fundamental interconnection by means of model conceptions learning thereby from the total system about its components and vice versa (cf. Fig. 3.2.1). To remain with the analogy of the Gaussian theorem, we calculate separately both sides of the above equation and we are satisfied if they are equal for any data set. From the view point of physics, we consider fluxes of momentum and energy between the Earth and extraterrestrial bodies as well as between the geophysical system parts of the Earth itself (for the latter ones also mass fluxes exist). This exchange happens on different time scales ranging from geological periods (eons) down to tidal and weather dynamics (hours). The above formulated balance must be always fulfilled.

Naturally at the beginning of the research work about forty years ago we firstly considered the long time scales. Existing geological data (growth rhythms of fossil organisms; time range 500 mio years) and astronomical observations (eclipses, orbits of planets; time range 3000 years) have been used and interpreted in terms of geophysical processes on the Earth. Within the last decades more and more new astronomical and geodetical data (LLR, VLBI, altimetry, gravity) became available. They have achieved meanwhile a high degree of accuracy and density allowing analysis from the decadal and annual scale down to seasonal, daily and tidal signals. The planetary data have firstly been focussed on Earth rotation parameters (mainly LOD) and supplemented in recent years by measurements of the shape and the gravity of the Earth and their variations. At the same time modelling has been advanced from separate and rough studies of the system parts to high-resolving and coupled simulations of the total Earth system.

In the current project some major progresses have been achieved on the sketched way:

- For first time a free, coupled model of the partial systems atmosphere, ocean and terrestrial hydrosphere has been realized and applied.
- The global ocean model comprises the wind- and thermohaline driven circulation as well as ephemeridic tides and their nonlinear interaction.
- Basing on this data a physically consistent dynamic Earth model is run and provides simultaneously rotation parameters, surface deformation and gravity field of the Earth. The numerical results are directly compared with satellite data.

'Free' model means that on the rotating Earth with real topography – like in nature – only solar radiation and gravitational potential of Moon and Sun are acting. Atmosphere and ocean circulations as well as the hydrological cycle are freely developing under this forcing. No observational data are assimilated resulting in an independent numerical data set. This set is physically consistent in the sense that momentum, energy and mass are conserved in the total system and that fluxes between the system parts are steady.

The developed model type is necessary for the synthetical interpretation of existing and newly gained geophysical, geodetical and astronomical data, although it still may have some deficiencies for operational use. Restricted spatial resolution, insufficient parameterisation of processes or numerical artefacts must cause inaccuracies which may be greater than in a 'bounded' (by data assimilation) model. Nevertheless, for the theoretical interpretation of remote sensing data, its correction and for deducing information on the geophysical system parts, specifically for future scenarios, our model type is the only appropriate approach.

Further research activities could now focus on

- refinement of the model resolution;
- improvement of process parameterisations;
- scenario runs under global change.

The last item includes the monitoring of climate change. There are strong indications that climate change is reflected in time series' of planetary parameters (e.g. LOD). This opens the innovative possibility of an integral climate monitoring – independent of local geophysical observations.

7. References

ACCAD, Y., and C. L. PEKERIS (1978) *Solution for the M2 ans S2 tides in the world oceans from a knowledge of the tidal potential alone.* Phil. Trans. R. Soc. London Ser. A, 290, 235-266.

AOYAMA, Y., I. NAITO, T. IWABUCHI, and N. YAMAZAKI (2003) *Atmospheric quasi-14 month fluctuation and excitation of the Chandler wobble.* Earth Planets Space, 55, 25-28.

ARBIC, B.K., D. R. MACAYEAL, J. X. MITROVICA, and G. A. MILNE (2004) *Palaeoclimate: Ocean tides and Heinrich events.* Nature, 432, 460.

BASSIN, C, G. LASKEN and G. MASTERS (2000) *The current limits of resolution for surface wave tomography in North America.* EOS Trans AGU 81: F897 81pp.

BERGSTRÖM, S., (1992) *The HBV model – its structure and applications.* Swedish Meteorological and Hydrological Inst. Rep. 4, 35pp.

BOURDA, G. (2008)*: Length-of-day and space-geodetic determination of the Earth's variable gravity field.* J. Geodesy, 82, 295-305.

BRZEZINSKI, A., and J. NASTULA (2002)*: Oceanic excitation of the Chandler wobble.* Adv. Space. Res., 30, 195– 200.

BROSCHE, P., and J. SÜNDERMANN (EDS.) *(1978) Tidal friction and the Earth's rotation.* Springer-Verlag, 241pp.

BROSCHE, P., and J. SÜNDERMANN (EDS.) *(1982) Tidal friction and the Earth's rotation II.* Springer-Verlag, 345pp.

BROSCHE, P., and J. SÜNDERMANN (EDS.) *(1990) Earth's rotation from eons to days.* Springer-Verlag, 255pp.

BROSCHE, P., and J. SÜNDERMANN (1985) *The Antarctic Circumpolar Current and its influence on the Earth's rotation.* Dt. Hydrogr. Z., 38, 1–6

CHAO, B.F. (1994) *The Geoid and Earth Rotation.* In: Vanicek, P., N. Christou (Eds): Geoid and its geophysical interpretations, CRC Press, Boca Raton, 285-298.

CHEBOTAREV, A.I. (1977) *364 – Comp. of meteorology Vol. II: Part 1 – General Hydrology.* World Meteorological Organisation, Geneva, 23pp.

COX, C. and B. CHAO (2002)*: Detection of large-scale mass redistributions in the terrestrial system since 1998.* Science, 297, 247-250.

DE VIRON, O., V. DEHANT, H. GOOSSE, and M. CRUCIFIX (2002) *Effect of global warming on the length-of-day.* Geoph. Res. Lett., 29(7), 10.1029/2001GL013672.

DICK, W.R., and B. RICHTER (EDS.) *(2008) IERS Annual Report 2006.* Verlag des Bundesamts für Kartographie und Geodäsie, Frankfurt am Main, 187pp.

DOBSLAW, H., and M. THOMAS (2007) *The impact of river run-off on global ocean mass redistribution.* Geophys. J. Int., 168, 527-532.

DRIJFHOUT, S., C. HEINZE, M. LATIF and E. MAIER-REIMER (1994) *Mean circulation and internal variability in an ocean primitive equation model.* J. Geophys. Res., 99, 24821-24852.

DÜMENIL, L. and E. TODINI, (1992) *A rainfall-runoff scheme for use in the Hamburg climate model.* In: Kane, J.P. (ed) Advances in theoretical hydrology – a tribute to James Dooge. Elsevier Science, Amsterdam, 129-157.

DZIEWONSKI, A., and D. ANDERSON (1981) *Preliminary Reference Earth model (PREM).* Phys. Earth Planet. Int., 25, 297-356.

FARRELL, W. (1972) *Deformation of the Earth by surface loads.* Rev Geophys Space Phys 10, 761-797.

FRÖHLICH, C., and J. LEAN (1998) *The Sun's total irradiance: Cycles, trends in the past two decades and associated climate change uncertainties.* Geoph. Res. Lett., 25, 4377–4380.

FURUYA, M., Y. HAMANO, and I. NAITO (1996) *Quasi-periodic wind signal as a possible excitation of Chandler wobble.* J. Geophys. Res., 101, 25537-25546.

GARRETT, C. (2003) *Internal tides and ocean mixing.* Science, 301, 1858–1859.

GENT P. R., J. WILLEBRAND, T. MCDOUGALL, and J. C. MC WILLIAMS (1995) *Parameterizing eddy-induced tracer transports in ocean circulation models.* J. Phys. Oceanogr., 25, 463-474.

GREATBATCH, T. J. (1994) *A note on the representation of steric sea level in models that conserve volume rather than mass.* J. Geophys. Res., 99, 12767-12771.

GRIESBACH, I. (2004) *Validierung modellierter kontinentaler Wassertransporte.* TU-Dresden, Institut für Planetare Geodäsie – Astronomie, 157pp.

GROSS, R.S. (1986) *The influence of earthquakes on the Chandler wobble during 1977-1983.* Geophys. J. R. Astr. Soc., 85, 161-177.

GROSS, R.S. (1992) *Correspondence between theory and observations of polar motion.* Geophys. J. Int., 109, 162-170.

GROSS, R.S. (2000) *The excitation of the Chandler wobble.* Geophys. Res. Lett., 27(15), 2329-2332.

HAGEMANN, S., and L. DÜMENIL–GATES (2003) *Improving a subgrid runoff parameterization scheme for climate models by the use of high resolution data derived from satellite observations.* Clim. Dyn. 21, 349-359.

HAGEMANN, S., and L. DÜMENIL (1998a) *A parametrization of the lateral waterflow for the global scale.* Climate Dynamics,14, 17-31.

HAGEMANN, S., and L. DÜMENIL (1998b) *Documentation for the Hydrological Discharge Model.* Technical Report No. 17. Max Planck Institute for Meteorology, Hamburg, Germany, 42pp.

HINDERER, J., H. LEGROS, C. GIRE, and J.-L. LE MOUEL (1987) *Geomagnetic secular variation, core motions and implications for the Earth's wobbles.* Phys. Earth Planet. Int., 49, 121-132.

IPCC (INTERGOVERNMENTAL PANEL ON CLIMATE CHANGE) *(2007) Climate Change 2007.* The science of climate change. Working Group I: The Physical Basis of Climate Change, Cambridge University Press, 996pp.

JEFFREYS, H. (1962) *The Earth.* Cambridge University Press, Cambridge, 438pp.

JONES, P. D., M. NEW, D.E. PARKER, S. MARTIN, and I.G. RIGOR (1999) *Surface air temperature and its variations over the last 150 years.* Rev. Geoph., 37, 173–199.

JUNGCLAUS, J. H., N. KEENLYSIDE, M. BOTZET, H. HAAK, J.-J. LUO, M. LATIF, J. MAROTZKE, U. MIKOLAJEWICZ, and E. ROECKNER (2006) *Ocean circulation and tropical variability in the coupled model ECHAM5/MPI-OM.* J. Climate, 19, 3952–3972

KALNAY, E., M. KANAMITSU, R. KISTLER (1996) *The NCEP/ NCAR 40-year reanalysis project.* Bull. Amer. Meteor. Soc., 77, 437-471.

KRISTJÁNSSON, J. E., T. IVERSEN, Ø. KIRKEVÅG, A. SELAND, and J. DEBERNARD (2005) *Response of the climate system to aerosol direct and indirect forcing: Role of cloud feedbacks.* J. Geoph. Res., 110, 10.1029/2005JD006299.

LAMBECK, K. (1980) *The Earth's Variable Rotation: Geophysical Causes and Consequences.* Cambridge University Press, 449pp.

LE PROVOST, C. (1995) *A new sea truth data set for tides.* ftp:// meolipc.img.fr/pub/ST103

LEDWELL J.R., E. T. MONTGOMERY, K. L. POLZIN, L. C. ST. LAURENT, R. W. SCHMITT, and J. M. TOOLE (2000) *Evidence for enhanced mixing over rough topography in the abyssal ocean.* Nature, 403, 179–182.

LEE H.-C., A. ROSATI, and M. SPELMAN (2005) *Barotropic tidal mixing effects in a coupled climate model: Oceanic conditions in the Northern Atlantic.* Ocean Modelling, 11, 464-477.

LEGUTKE S. and R. VOSS (1999) *The Hamburg Atmosphere-Ocean Coupled Circulation Model ECHO-G.* Technical report, DKRZ, Hamburg. 62pp.

LIN, S. J. and R.B. ROOD (1996) *Multidimensional flux form semi-Lagrangian transport.* Monthly Weath. Rev., 124, 2046–2068.

LORENZ, D. J. and E.T. DEWEAVER (2007) *Tropopause height and zonal wind response to global warming in the IPCC scenario integrations.* J. Geoph. Res., 112, 2007. 10.1029/2006JD 008087.

MARCHENKO, A.N., and P. SCHWINTZER (2003) *Estimation of the Earth's tensor of inertia from recent global gravity field solutions.* J. Geodesy, 76, 495-509.

MARSHALL, J., A. ADCROFT, C. HILL (1997) *A finite-volume, incompressible Navier Stokes model for studies of the ocean on parallel computers.* J. Geophys. Res., 102(C3), 5753-5766.

MARSLAND, S. J., H. HAAK, J. JUNGCLAUS, M. LATIF, and F. RÖSKE (2003) *The Max-Planck-Institute global ocean-sea ice model with orthogonal curvilinear coordinates.* Ocean Modelling, 5, 91–127.

MCCARTHY, D.D., and G. PETIT (EDS.) *(2004) IERS Conventions 2003.* IERS Technical Note, vol. 32, Verlag des Bundesamts für Kartographie und Geodäsie, Frankfurt am Main, 127 pp.

MEEHL, G. A., G.J. BOER, C. COVEY, M. LATIF, and R.J. STOUFFER (2000) *The Coupled Model Intercomparison Project (CMIP).* Bull. Amer. Meteorol. Soc., 81, 313-318.

MEISEL, B., D. ANGERMANN, M. KRÜGEL (2005) *Refined approaches for terrestrial reference frame computations.* Adv. in Space Res., 36, 350-357.

MESINGER, F. and A. ARAKAWA (1976) *Numerical methods used in atmospheric models.* Global Atmospheric Research Programme (GARP) Publication Series, 17, 3771–3791.

MILLY, P. C. D., and A. B. SHMAKIN, 2002*: Global modeling of land water and energy balances. Part I: The land dynamics (LaD) model.* Journal of Hydrometeorology, 3(3), 283-299.

MIN, S.-K., S. LEGUTKE, A. HENSE, and W.-T. KWON (2005) *Internal variability in a 1000-year control simulation with the coupled climate model ECHO-G – I. Near-surface temperature, precipitation and mean sea level pressure*. Tellus, 57A, 605–621.

MIN S.-K., S. LEGUTKE, A. HENSE, U. CUBASCH, W.-T. KWON, and U. SCHLESE (2006) *East Asian climate change in the 21st century as simulated by the coupled climate model ECHO-G under IPCC SRES scenarios.* Journal of the Meteorological Society Japan, 84,1–26.

MONTENEGRO A., M. EBY, A. J. WEAVEE, S. R. JAYNE (2007) *Response of a climate model to tidal mixing parameterization under present day and last glacial maximum conditions.* Ocean Modelling 19, 125-137

MORITZ, H. (1980) *Geodetic Reference System 1980.* Bull. Geod., 54, 395-405.

MORITZ, H., and I.I. MUELLER (1987) *Earth rotation.* Ungar Publishing Company, New York, 617pp.

MÜLLER, M. (2008) *Synthesis of forced oscillations, Part I: Tidal dynamics and the influence of the loading and self-attraction effect.* Ocean Modelling, 20, 207-222.

MÜLLER, M., H. HAAK, J. H. JUNGCLAUS, J. SÜNDERMANN and M. THOMAS (2009) *The effect of ocean tides on a Climate model simulation.* Geophys. Res. Lett., submitted.

MUNK W. and C. WUNSCH (1998)*; Abyssal recipes II: energetics of tidal and wind mixing.* Deep-Sea Res., 45, 1977–2010.

MUNK, W.H., and G. J. F. MACDONALD (1960) *The rotation of the Earth: A geophysical discussion.* Cambridge University Press, New York, 323pp.

PACANOWSKI, R. C., and S. G. H. PHILANDER (1981)*: Parameterization of vertical mixing in numerical models of tropical oceans.* J. Phys. Oceanogr., 11(11), 1443-1451.

PRESS, W.H., B. P. FLANNERY, S. A. TEUKOLSKY, and W. T. VETTERLING (1987) *Numerical Recipes.* Cambridge University Press, New York, 818pp.

RAYNER, N. A., D.E. PARKER, E.B. HORTON, C.K. FOLLAND, L.V ALEXANDER, D.P. ROWELL, E.C. KENT, and A. KAPLAN (2003) *Globally complete analyses of sea surface temperature, sea ice and night marine air temperature, 1871-2000.* J. Geoph. Res., 108, 10.1029/2002JD002670.

RAYNER, N. A., P. BROHAN, D.E. PARKER, C.F. FOLLAND, J.J. KENNEDY, M. VANICEK, T. ANSELL, and S.F.B. TETT (2006) *Improved analyses of changes and uncertainties in sea surface temperature measured in situ since the mid-nineteenth century: the HadSST2 data set.* Journal of Climate, 19(3), 446–469.

ROECKNER, E., K. ARPE, L. BENGTSSON, S. BRINKTOP, L. DÜMENIL, M. ESCH, E. KIRK, F. LUNKEIT, M. PONATER, B. ROCKEL, R. SAUSEN, U. SCHLESE, S. SCHUBERT, M. WINDELBAND, (1992) *Simulation of the present-day climate with the ECHAM model: impact of model physics and resolution.* Max-Planck-Institute for Meteorology, Rep. 93, Hamburg. 171pp.

ROECKNER, E., G. BÜML, L. BONAVENTURA, R. BROKOPF, M. ESCH, M. GIORGETTA, S. HAGEMANN, I. KIRCHNER, L. KORNBLUEH, E. MANZINI, A. RHODIN, U. SCHLESE, U. SCHULZWEIDA, and A. TOMPKINS (2003) *The atmospheric general circulation model ECHAM5, part I: Model description.* Technical Report 349, Max-Planck-Institute for Meteorology, 127pp.

RUDOLF, B., H. HAUSCHILD, W. RUETH, U. SCHNEIDER (1996)*: Comparison of raingauge analyses, satellite-based precipitation estimates and forecast model results.* Adv. in Space Research, 18(7), 53 – 62.

SASAO, T., S. OKUBO, and M. SAITO (1980) *A simple theory on the dynamical effects of a stratified fluid core upon nutational motion of the earth.* In: Nutation and the Earth's Rotation, IAU Symposia, vol. 78, edited by E.P. Fedorov, D. Reidel, Kiev, 165-183.

SCHERNECK H.-G. (1990) *Loading Green's functions for a continental shield with a Q-structure for the mantle and density constraints from the geoid.* Bulletin d'Information Marees Terrestres, 108, 7757-7792.

SCHILLER A. (2004) *Effects of explicit tidal forcing in an OGCM on the water-mass structure and circulation in the Indonesian throughflow region.* Ocean Modelling, 6, 31-49

SCHMIDT, M. (2000) *Wavelet analysis of stochastic signals.* In Kolaczek, B., H. Schuh and D. Gambis (eds.): High frequency to subseasonal variations in Earth rotation, IERS Technical Note 28, Observatiore de Paris, 65-72.

SCHMIDT, M. (2001) *Grundprinzipien der Wavelet-Analyse und Anwendungen in der Geodäsie.* Shaker, Aachen.

SEGSCHNEIDER, J., and J. SÜNDERMANN (1997) *Response of a global ocean circulation model to real-time forcing and implications to Earth's rotation.* J. Phys. Oceanogr., 27, 2370-2380

SEITZ, F. (2002) *Atmosphärische und ozeanische Massenverlagerungen als Antrieb für ein Kreiselmodell der Erde.* In: Vorträge beim 4. DFG-Rundgespräch im Rahmen des Forschungsvorhabens Rotation der Erde zum Thema 'Wechselwirkungen im System Erde', H. Schuh, M. Soffel, H. Hornik (eds.), Deutsche Geodätische Kommission, A 118, 96-101, München.

SEITZ, F. (2004) *Atmosphärische und ozeanische Einflüsse auf die Rotation der Erde – Numerische Untersuchungen mit einem dynamischen Erdsystemmodell.* Deutsche Geodätische Kommission, C 578, München, 94 p..

SEITZ, F. (2005a)*: Atmospheric and oceanic influences on polar motion – numerical results from two independent model combinations.* Artificial Satellites, 40(3), 199-215.

SEITZ, F. (2005b) *Zur Anregung der Chandler-Schwingung.* Zeitschrift für Vermessungswesen, 130(3), 166-173.

SEITZ F., and H. DREWES (2009)*: Simulation of polar motion with a dynamic Earth system model over a period of 200 years (1860 – 2060).* Proceedings of Les Journées "Systèmes de référence spatio-temporels" and X. Lohrmann-Kolloquium, Dresden, 22. – 24. September 2008

SEITZ, F., and M. KRÜGEL (2009): *Modeling vertical load deformations in consideration of crustal inhomogeneities*. In: Drewes, H. (ed.): Geodetic Reference Frames, IAG Symposia 134, Springer, Berlin, in press.

SEITZ, F., and H. KUTTERER (2002) *Numerical solutions for the non-linear Liouville equation.* In: Adam, J., K.-P. Schwarz (eds): Vistas for Geodesy in the New Millennium, IAG Symposia, 125, Springer, Berlin, 463-468.

SEITZ, F., and H. KUTTERER (2005) *Sensitivity analysis of the non-linear Liouville equation.* In: Sansò F. (eds): A Window on the Future of Geodesy, IAG Symposia, 128, 601-606, Springer, Berlin, 601-606

SEITZ, F., and M. SCHMIDT (2005) *Atmospheric and oceanic contributions to Chandler wobble excitation determined by wavelet filtering.* J. Geophys. Res., 110, B11406, doi: 10.1029/2005JB003826.

SEITZ, F., J. STUCK, and M. THOMAS (2004) *Consistent atmospheric and oceanic excitation of the Earth's free polar motion.* Geophys. J. Int., 157, 25-35.

SEITZ, F., J. STUCK, and M. THOMAS (2005) *White noise Chandler wobble excitation.* In Plag, H., B.F. Chao, R. Gross and T. van Dam (eds): Forcing of polar motion in the Chandler frequency band: A contribution to understanding interannual climate variations, Cah. Cent. Eur. Geodyn. Seismol., 24, ECGS, Luxembourg, 15-21.

SIDORENKOV, N.S. (1992) *Excitation mechanisms of Chandler polar motion.* Astron. Zeitschr., 69, 905-909.

SIMMONS, H.L., S.R. JAYNE, L.C. ST. LAURENT, and A.J. WEAVER (2004)*; Tidally driven mixing in a numerical model of the ocean general circulation.* Ocean Modelling, 6, 245-263.

SIMONS, A. J., D.M. BURRIDGE, M. JARRAUD, C. GIRARD, and W. WERGEN (1989) *The ECMWF medium-range prediction models.* Development of the numerical formulations and the impact of increased resolution. Meteor.Atmos.Phys., 40, 28–60.

SMITH, M.L. and F.A. DAHLEN (1981) *The period and Q of the Chandler wobble.* Geophys. J. R. astr. Soc., 64, 223-281.

STAMMER, D., C. WUNSCH, R. GIERING, C. ECKERT, P. HEIMBACH, J. MAROTZKE, A. ADCROFT, C. N. HILL, and J. MARSHALL (2002)*, Global ocean circulation during 1992–1997, estimated from ocean observations and a general circulation model.* J. Geophys. Res., 107(C9), 3118, doi:10.1029/2001JC000888.

STANDISH, E.M. (1998) *JPL planetary and lunar ephemerides DE405/LE405.* JPL Tech. Rep. IOM 312.F-98-048, Jet Propulsion Laboratory, Pasadena, 18 pp.

STUCK, J., and A. HENSE (2002)*: Die simulierte dreidimensionale atmosphärische Drehimpulsvariabilität.* In Schuh H., Soffel M., Hornik H. (Eds.): Vorträge beim 4. DFG-Rundgespräch im Rahmen des Forschungsvorhabens Rotation der Erde zum Thema „Wechselwirkungen im System Erde“., Dt. Geod. Komm., Reihe A, Nr. 118, München, 117-124.

STUCK, J., F. SEITZ, and M. THOMAS (2005) *Atmospheric forcing mechanisms of polar motion.* In: Plag, H (eds) Forcing of polar motion in the Chandler frequency band: A contribution to understanding interannual climate variations, Cah. Cent. Eur. Geodyn. Seismol., 24, ECGS, Luxembourg, 127-133.

SUN, H., B. DUCARME, and V. DEHANT (1995) *Effect of the atmospheric pressure on surface displacements.* J Geodesy 70, 131-139.

SÜNDERMANN J., and A. HENSE (2008)*: A physical consistent system model for the study of Earth rotation, surface defomation and gravity field parameter.* Proceedings of Les

Journées "Systèmes de référence spatio-temporels" and X. Lohrmann-Kolloquium, Dresden, 22. – 24. September 2008

TALLEY, L.D., J.L. REID, and P.E. ROBBINS (2003) *Data-based meridional overturning streamfunctions for the global ocean.* J. Climate, 16, 3213-3226.

TANRE, D., J.-F. GELEYN, and J.M. SLINGO (1984). *First results of the introduction of an advanced aerosol-radiation interaction in the ECMWF low resolution global model*. In H. Gerber and A. Deepak (Eds.): Aerosols and their Climatic Effects, Hampton,Virgina.

TAYLOR, K. E., D. WILLIAMSON, and F. ZWIERS (2000). *The sea surface temperature and sea-ice concentration boundary conditions of AMIP II simulations*. PCMDI report No. 60, 19(3),20pp.

TERRAY L., S. VALCKE, and A. PIACENTINE (1998) *The OASIS coupler user guide, Version 2.*2. Techn. Rep. TR/CMGC/98-05, CERFACS, 85pp.

THOMAS, M. (2000) *Ergebnisse eines Simultanmodells für Zirkulation und ephemeridische Gezeiten im Weltozean.* PhD thesis, Univ. Hamburg, 128pp.

THOMAS, M., J. SÜNDERMANN, and E. MAIER-REIMER (2001) *Consideration of ocean tides in an OGCM and impacts on subseasonal to decadal polar motion excitation.* Geophys. Res. Lett, 28, 2457-2460.

TOOLE J.M., LEDWELL J.R., POLZIN K.L., SCHMITT R.W., and MONTGOMERY E.T. (1997)*; The Brazil Basin tracer release experiment.* Int. WOCE Newsl. 28, 25–28.

TRENBERTH, K. E. (1997) *The definition of El Niño.* Bull. Amer. Meteor. Soc., 78, 2771-2777

UPPALA, S., J.K. GIBSON, M. FIORINO, A. HERNANDEZ, P. KALLBERG, X. LI, K. ONOGI, and S. SAARINEN (1999) *ECMWF's Second Generation Reanalysis – ERA-40.*

VAN FLANDERN, T. C., and K. F. PULKKINEN (1998) *Low-precision formulae for planetary positions.* The Astrophysical Journal-Supplement Series 41, 3, Willmann-Bell, 10pp.

VAN OLDENBORGH, G.J., S.Y. PHILIPPS, and M. COLLINS (2005) *El Niño in a changing climate.* A multi model study. Ocean Sci., 1, 81-95

VONDRAK, J., C. RON, I. PESEK, and A. CEPEK (1995) *New global solution of Earth orientation parameters from optical astrometry in 1900-1990.* Astron. Astrophys., 297, 899-906.

WAHR, J.M. (1985) *Deformation induced by polar motion.* J. Geophys. Res., 90, B11, 9363-9368.

WALTER, C. (2008) *Simulation hydrologischer Massenvariationen und deren Einfluss auf die Erdrotation.* Phd-thesis, TU Dresden, Germany, 199pp.

WIGMOSTA, M.S., L. VAIL, and D.P. LETTENMAIER (1994) *A distributed hydrology-vegetation model for complex terrain.* Water Resource Res, 30, 1665-1679.

WILSON, C.R, and R.A. HAUBRICH (1976) *Meteorological excitation of the Earth's wobble.* Geophys. J. R. Astr. Soc., 46, 707-743.

WINKELNKEMPER, T., F. SEITZ, S.K. MIN, A. HENSE (2008): *Simulation of historic and future atmospheric angular momentum effects on length-of-day variations with GCMs*. In: Observing our Changing Earth, M. Sideris (Ed.), IAG Symposia 133, 447-454, Springer, Berlin.

WOLFF, J. O., E. MAIER-REIMER, and S. LEGUTKE (1996) *The Hamburg Ocean Primitive Equation Model HOPE.* Technical Report No.13, DKRZ, Hamburg. 100pp.